Nonlinear Optical Properties of $BaTiO_3$ in Symmetric and Asymmetric Microcavities

Thesis submitted for the degree of
Doctor of Philosophy in Physics

By

SHIHAB N K
(13PHPH13)

Under the guidance of

PROF. D. NARAYANA RAO

PROF. P. ANANTHA LAKSHMI

School of Physics
University of Hyderabad
Hyderabad-500 046, India
June 2020

DECLARATION

I hereby declare that this thesis titled **Nonlinear Optical Properties of $BaTiO_3$ in Symmetric and Asymmetric Microcavities** submitted by me, under the guidance and supervision of Prof. D. Narayana Rao and Prof. P. Anantha Lakshmi is a bonafide research work and is free from plagiarism. I also declare that it has not been submitted previously, in part or in full to this university or any other university or institution, for the award of any degree or diploma. I hereby agree that my thesis can be deposited in INFLIBNET.

A report on plagiarism statistics from the university librarian is enclosed.

Name: Shihab N K

Reg. No: 13PHPH13

Place: Hyderabad

Date:

CERTIFICATE

This is to certify that the thesis titled **Nonlinear Optical properties of $BaTiO_3$ in Symmetric and Asymmetric Microcavities** submitted by Shihab N. K. (Reg. No. 13PHPH13), in partial fulfillment of the requirements for the award of Doctor of Philosophy in Physics, is a bonafide work carried out by him under our supervision and guidance.

This thesis is free from plagiarism and has not been submitted previously, in part or in full to this or any other university or institution, for an award of any degree or diploma.

Further, the student has passed the following courses towards fulfillment of coursework requirement for PhD:

Course Code	Name of the Course	Credits	Pass/Fail
PY801	Advanced Quantum Mechanics	4	Pass
PY803	Advanced Statistical Mechanics	4	Pass
PY804	Advanced Electromagnetic Theory	4	Pass
PY821	Research Methodology	4	Pass

Prof. D. Narayana Rao

Prof. P. Anantha Lakshmi

Prof. Ashok Chatterjee
Dean,
School of Physics
University of Hyderabad

Place: Hyderabad

Date:

ACKNOWLEDGEMENT

Alhamdulillah (*Praise be to God*)

I would like to express my deep sense of gratitude to my research supervisor Prof. D. Narayana Rao for giving me an opportunity to work with him for my PhD and his constant encouragement, care, patience and guidance in all the time of research and making of this thesis. I would like to thank my thesis co-supervisor Prof. P. Anantha Lakshmi for her help during my research years.

I am extremely thankful to my collaborators Dr. G. Ramesh Babu, Dr. U. P. Mohammed Rasi (Dept. of Physics, Pondicherry University) and Prof. G. Vijaya Prakash, Jitendra Nath Acharyya (Nanophotonics Lab, Dept. of Physics, Indian Institute of Technology Delhi, New Delhi) for their valuable suggestions and fruitful discussions.

I would like to thank my doctoral committee members Prof. Suneel Singh, Dr. V. S. Ashoka and Prof. V. Nirmal Kumar for their valuable suggestions in DRC meetings. My sincere gratitude to Prof. Ashok Chatterjee, Dean, School of physics and former Deans Prof. V. Seshu Bai and Prof. Bindu A. Bambah for providing different facilities in the school. I also thank all the non-teaching staff especially Mr. Abraham, Mrs. Deepika and Mr. Sudarshan.

I thank to all my group members Dr. N. S. Ram Gopal and my seniors Dr. Sriramulu, Dr. Saikiran, Dr. Jyoti for their constant support and helpful discussions. My lab mates Nabil, Mudasir, Remya, Balaji, Sahoo, Abu Tahir, Vinod and Sajin were awesome and they made research life more beautiful. I am deeply thankful to my friends Dr. C. T. Samlan and Joshy Joseph for their support and helping hands.

Financial assistance from the University of Hyderabad is greatly acknowledged.

I am very grateful to Al-Islah Orphanage, Wadirahmah for moulding my educational life and bringing at this stage. Without the care, support and patience of my family this journey will be incomplete. I extend love and thanks for all.

Dedicated to my brother late **N. K. Riyas** for the inspiration and

living memories.

ABSTRACT

Ultrafast high dense information processing and transmission demand photonic devices and technologies in which microcavities are integral part due to its ability to confine the light field suitable for wave guide and lasing applications at micron scale. Design of a Microcavity using Bragg mirrors is commonly known as One Dimensional Photonic Crystal (1D PhC) which consists of alternate layers of high contrast dielectric materials with a defect layer at the centre. The thickness of each layer in the Bragg mirror and defect layer are equal to the quarter wave and half wave dimension for a given wavelength and offer a field confinement in the defect layer. In this thesis, we discuss the fabrication of Photonic crystal using two different methods: Sol-Gel and RF sputtering.

The first part of the thesis is focused on the fabrication of 1D PhC by Sol-Gel method, one of the simplest and cheapest available methods and later we switch over to fabrication by RF sputtering. We classify the crystals into symmetric and asymmetric microcavities based on Bragg's condition being satisfied or otherwise. We fabricated both types of microcavities and studied the symmetry effect by characterizing the linear and non-linear optical properties of $BaTiO_3$, which is a highly dielectric material suitable for multi-layer capacitors and energy storage applications, in additions to its ferroelectric and piezoelectric properties. The photoluminescence emissions from the two microcavities are compared.

In addition to the above, we have also fabricated two identical microcavities with different thicknesses of defect layer and its role in the nonlinear absorption is studied. Here it is experimentally observed that with an increase in the thickness of the defect layer, a good reversal from reverse saturable absorption (RSA) to saturable absorption (SA) in response to the angle tuning of the sample takes place. The spatial field distribution along the depth of the microcavities, using transfer matrix simulation shows that it is in good agreement with the experiment.

CONTENT

Chapter 1

Introduction

A brief introduction to photonic crystal and one dimensional photonic microcavity is presented. The origin of photonic band gap and ensuing phenomena such as slow light and the photon localization in the microcavity are discussed.

1.1 Motivation

The technological development of the modern human from stone-age to information-age is quite astonishing, especially the information technology and the information network. The transformation of information through metallic waveguides and cavities is not possible for certain frequencies of the electromagnetic spectrum, with reference to a threshold frequency [1-3]. The transformation of the electromagnetic waves through above systems is extremely difficult if the frequency lies outside the microwave regime, in particular, in the optical spectrum or visible light [1]. Therefore, an alternate system is required for the transformation of electromagnetic waves to include broader ranges of the electromagnetic spectrum. Photonic crystal is such an artificial system that can control the propagation modes of photons [4,5].

1.2 Introduction

A crystal is formed by the periodic arrangement of atoms or molecules which provides the periodic potential for electron to propagate through the crystal [1]. Photonic crystals (PhCs) are artificially fabricated; periodically arranged spatial distribution of particles with different refractive indices with the lattice parameter being equivalent to the wavelength of interest. These spatially modulated materials with different refractive indices produce forbidden regions known as band gaps or stop bands which completely block the propagation of electromagnetic waves of certain frequencies [6,7]. The wave vector associated with the wavelength lying in this stop band has imaginary value and it is exponentially attenuated as it propagates along the PhC [1]. The width of the photonic band gap (PBG) is decided by various factors such as refractive index contrast between the adjacent materials, lattice parameters and structural symmetry etc. [8,9]. The PBG structure associated with the PhC is an optical analogue of semiconductor crystal. In semiconductor crystal the electronic band structure is obtained by solving the time independent Schrödinger equation whereas the band structure in PhC is described by the Maxwell's equations [10,11].

PhCs can be classified as 1D, 2D and 3D based on the periodic arrangement of materials having different refractive indices, a schematic diagram of which is shown in Figure 1.1. A 1D PhC is simply a stack of multilayer structures known as Bragg reflectors in which adjacent layers differ in their refractive indices, while a 2D PhC is an arrangement of material columns in a plane [12-15]. A spherical arrangement of nanoparticles into ordered arrays constitutes 3D PhCs; opals and inverted opals are categorised in 3D PhCs [16-18]. Apart from the dimension, the fabrication complexity of PhC is depends on the desired wavelength of PBG. The larger dimension PhC with lower frequency band gap is easy to fabricate, for example, a 3D microwave crystal (the order of wavelength is cm). However, the major scientific defiance of 1D PhCs are its fabrication as its PBG lies in the optical region [19]. The first direction towards a PhC with a full PBG was proposed by Ho *et al*, which is a periodic arrangement of dielectric spheres in a diamond like structure [20]. It is very difficult to fabricate since it lies in micron and submicron length scales for IR or optical devices. Later in 1991, Eli Yablonovitch formulated an inventive way of constructing inverse diamond lattice by drilling cylindrical holes through a dielectric block (3D PhC) that possesses a full PBG, which lies in the microwave regime and is known as Yablonovite structure [21]. The complete PBG is observed in different structures such as Woodpile structures proposed by Susumu Noda [22], FCC structures put forth by Joannopoulos [1], square spiral structures suggested by John and Toader [23], scaffold structures suggested by Joseph Haus and his colleagues [24], tunable electrooptic inverse opal structure developed by Busch and John [25] etc. In 1996 Thomas Krauss exhibited 2D PhC such that its PBG lies in the optical wavelengths [26].

The propagation of electromagnetic waves through 1D stratified media was first illustrated by Lord Rayleigh in 1887 and he suggested the concept of quarter wave stack [27]. It took 100 years of journey to realize the structure in the form of complete PBG by E. Yablonovitch and S. John in 1987 [4,5].

In the early years of the 21st century, research in photonic crystals has been well established in the fabrication, understanding the physical phenomenon and the recognition of photonic crystal devices such as PhC laser, PhC filters, PhC switches etc. Now researchers pay great attention to the fabrication of unconventional PhC devices by incorporating novel physical effects [28].

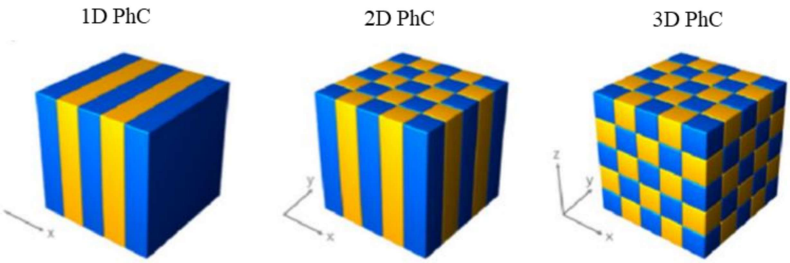

Figure 1.1: *schematic representations of 1D, 2D and 3D photonic crystals (Image courtesy Ref. [29])*

1.3 One dimensional Photonic Crystals

A 1D PhC is an artificially structured electromagnetic media in which the layers of periodic structures with different dielectric constants vary only in one direction (say Z axis direction) [1]. It can diffract light in any region of electromagnetic spectrum by suitably selecting the adjacent materials and its thicknesses. A 1D PhC can be fabricated by alternately placing two (or more) layers with high and low refractive indices [30,31]. The most common example of a 1D PhC is a Bragg mirror (BM), which consists of two dielectric materials having different refractive indices [32, 33]. The thickness of the layers of BM should follow the criteria, $nd=\lambda/4$, where n is the refractive index, d is the thickness of each layer and λ is the wavelength of the incident electromagnetic wave. Since 1D PhC can reflect light for a suitable frequency range it can be used for many applications unlike metals. Oxide based dielectric materials are a preferred choice, because of its transparency from UV to near IR

and it has good protection from temperature and radiation they possess [34]. Here we have selected SiO_2, TiO_2 and $BaTiO_3$ materials for the construction of 1D PhC. Figure 1.2 represents the schematic diagram and FESEM image of 1D PhC composed of SiO_2 and TiO_2 consisting of 14 layers.

The PBG of a 1D PhC is decided by the refractive index contrast between the nearby materials and the width of the band gap is determined by the following expression [1].

$$\frac{\Delta\omega}{\omega_m} = \frac{4}{\pi}\sin^{-1}\left(\frac{|n_1-n_2|}{n_1+n_2}\right) \qquad (1.1)$$

Where $\Delta\omega$ and ω_m are the width and the central frequency of the band gap respectively, with $n_1$and n_2 being the refractive indices of adjacent layers. It has been found that the band gap width is higher for larger refractive index contrast between the alternating materials [1,2]. Photonic bands at lower frequency side of PBG are known as air band and the higher frequency bands are dielectric band [35]. This PBG is an optical analogue of the forbidden gap in semiconductors.

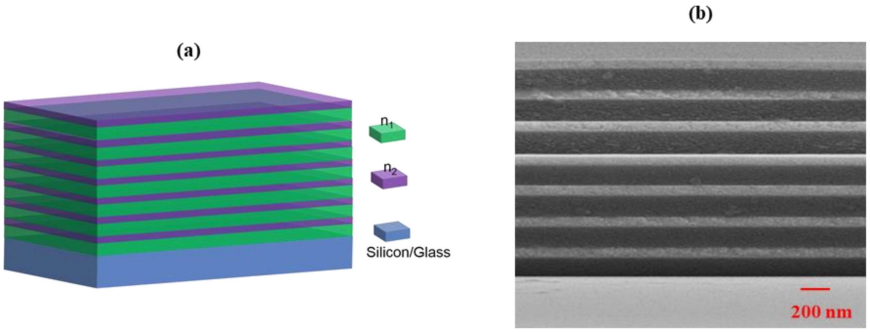

Figure 1.2: *(a) Schematic diagram of 1D photonic crystal (b) Cross sectional FESEM image of 1D photonic crystal. The dark and bright region corresponds to SiO_2 and TiO_2 respectively.*

1.4 One dimensional Photonic Microcavity

A 1D PhC microcavity is fabricated by inserting a defect layer in the periodic arrangement of the Bragg mirror and it can be seen as two parallel Bragg mirrors separated by a defect layer (spacer layer) [36,37]. These parallel mirrors are called distributed Bragg reflector (DBR), with the thickness of each layer of Bragg mirrors being $\lambda/4$ and that of the defect layer $\lambda/2$ [1]. An electromagnetic wave, incident on a one dimensional photonic microcavity, with its frequency in resonance with the defect mode can transmit through the PhC. The reflection spectrum of the 1D PhC microcavity comprised of a wide PBG with a narrow pass band (defect mode) at its centre [1,2]. The schematic diagram and FESEM image of the 1D photonic crystal microcavity is shown in Figure 1.3. Here microcavity is formed by placing a half wave (λ/2) layer of $BaTiO_3$ in between two Bragg mirrors formed by SiO_2, and TiO_2 layers. The central thick layer is the $BaTiO_3$ defect layer, and on either side, the dark and bright alternate layers are the two identical Bragg mirrors composed of SiO_2 and TiO_2 layers, respectively.

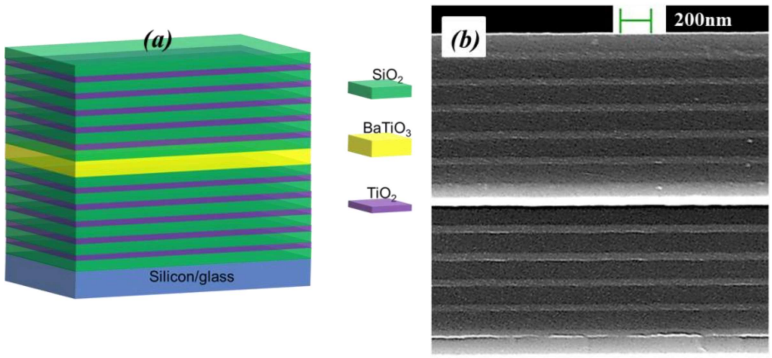

Figure 1.3: *(a) Schematic diagram of 1D PhC (b) Cross sectional FESEM image of 1D PhC. The dark and bright region corresponds to SiO_2 and TiO_2 respectively.*

1.5 Physics of photonic band gap

Propagation of electromagnetic wave and localisation of photons can be discussed on the basis of Bloch theory and Maxwell's equations [1,2]. A variety of numerical calculation methods are employed for understanding the PBG structure of PhC and nonlinear optical effects of PhCs. Some of the popularly used methods include the finite different time domain (FDTD) method [38,39], the plane wave expansion method [40,41], the transfer matrix method [42,43], etc. Here we are adopting the transfer matrix method to design our photonic crystal structure and to understand the electromagnetic field confinement in defect layers. The electromagnetic wave entering into the photonic crystal undergoes a coherent scattering at the interface of each dielectric layer and it undergoes a strong modulation by the periodic distribution of the potential. As a result, the photonic band gap appears and the frequency which lies in this PBG cannot propagate through the photonic crystal structure. But the electromagnetic wave whose frequency is in resonance with the defect mode can propagate through PBG based on the tunnelling effect [1,2]. The propagation of electromagnetic wave and the origin of PBG in PhC can be discussed using Maxwell's equations.

$$\nabla \times \vec{E} = -\frac{\partial \vec{B}}{\partial t} \tag{1.2}$$

$$\nabla . \vec{D} = \rho \tag{1.3}$$

$$\nabla \times \vec{H} = \vec{J} + \frac{\partial \vec{D}}{\partial t} \tag{1.4}$$

$$\nabla . \vec{B} = 0 \tag{1.5}$$

Where $\vec{E}$ is the electric field, $\vec{B}$ is the magnetic induction, $\vec{D}$ is the electric displacement vector ($\vec{D} = \varepsilon \vec{E}$), $\vec{H}$ is the magnetic field ($\vec{B} = \mu H$), $\vec{J}$ is current density. Since there are no free charge carriers in the dielectric material ($\rho = 0 \; and \; J = 0$), the above Maxwell's equations can be modified as

$$\nabla \times \vec{E} = -\frac{\partial \vec{B}}{\partial t} \quad (1.6)$$

$$\nabla.\vec{D} = 0 \quad (1.7)$$

$$\nabla \times \vec{H} = \frac{\partial \vec{D}}{\partial t} \quad (1.8)$$

$$\nabla.\vec{B} = 0 \quad (1.9)$$

The electric field and magnetic field are obtained by solving the above differential equations and can be written as,

$$\vec{E}(r,t) = \vec{E}(r)e^{i\omega t} \quad (1.10)$$

$$\vec{H}(r,t) = \vec{H}(r)e^{i\omega t} \quad (1.11)$$

Now, the electric displacement vector can be written as,

$$\vec{D}(r,t) = \varepsilon(r)\vec{E}(r)e^{i\omega t} \quad (1.12)$$

Using equations (1.11) and (1.12) in equation (1.8) , the electric field $\vec{E}(r)$ can be expressed as,

$$\vec{E}(r) = -\frac{i}{\omega\varepsilon(r)}\nabla \times \vec{H}(r) \quad (1.13)$$

The electromagnetic induction can be written as,

$$\vec{B}(r,t) = \mu(r)\vec{H}(r)e^{i\omega t} \quad (1.14)$$

Using equations (1.13) and (1.14) in (1.6), we can obtain

$$\nabla \times \left(\frac{1}{\varepsilon(r)}\nabla \times \vec{H}(r)\right) = (\mu\omega^2)\vec{H}(r) \quad (1.15)$$

Equation (1.15) is known as the master equation for the description of the propagation of electromagnetic wave through the photonic crystal. In order to understand the origin of the PBG, let us compare the master equation of photons and Schrödinger equation of electrons. Equation (1.11) gives the propagation state of photons similar to the electronic state in semiconductor crystal given below.

$$\Psi(r,t) = \Psi(r)e^{\left(\frac{iE}{\hbar}\right)t} \tag{1.16}$$

Where $\Psi(r)$ is the wave function of electron and E is the energy of the electron. The PBG structure of the PhC is obtained by solving the master equation (1.15), which is a complex differential equation.

1.6 Fabrication Processes

Various techniques have been developed for the fabrication of 1D PhCs such as holographic lithography [44,45], pulsed laser deposition method [46], ion exchange method [47], chemical vapour deposition method [48], etching method [49], Sol-Gel method [50], RF sputtering method [51], electron beam evaporation method [52] etc. In this thesis we are adopting two methods of fabrication, Sol-Gel and RF sputtering methods. Sol-Gel is a wet chemical fabrication method of producing solid materials from smaller molecules that is based on a chemical transformation of liquid alkoxide precursors into solid-state products by hydrolysis and polymerization reactions at room temperature. RF sputtering is a physical vapour deposition process on a substrate such as glass plate or silicon wafers, where the depositing material molecules are ejected from their respective targets via the strong collision of inert gas ions. More details of both methods are discussed in chapter 2.

1.7 Slow light effect in Photonic Crystals

The slow-light phenomenon has attracted many researchers in the world since it provides a control over the photon in light-matter interactions. The propagation of light with extremely low group velocity due to PBG effect in PhC is known as slow-light [53]. Usually, the phase

velocity v_p and group velocity v_g have no big difference as it propagates through normal media but, in PhC v_g is much smaller than v_p. The two important mechanisms for achieving slow light in PhC are coherent back scattering and omnidirectional reflection [54]. When light is incident on the PhC, it gets backscattered coherently at each unit cell of the crystal, so the crystal behaves as a one dimensional grating. If the phase and amplitude of forward propagating and backscattered light are equal, then it results in the formation of a standing wave, which is a slow mode with zero group velocity. At Γ- point in band structure, where $k = 0$, the modes travels very slow and forms a standing wave [53]. The slope of the band edges of PBG decrease considerably, that is $\frac{d\omega}{dk}$ tends to zero at the interface between the air band and dielectric band. The phenomenon of slow light in PhC is used in practical applications such as phase shifters [55], optical switches [56], optical micro amplifiers [57], optical storage [58], micro lasers [59] and optical delay lines [60] etc.

1.8 Nonlinear Effects in Photonic Crystals

The main issues in the modern computers are power dissipation and consequent hardware heating since it forced to operate at higher frequencies [3]. The telecommunication process is difficult when the electronics is operated at higher frequencies and electronics won't work at these frequencies. In this scenario, optical domain is perfectly suited to operate at higher frequencies. Combining nonlinear optics and PhCs has opened up a new dimension in physics which began as early as in 1970s, and since then the research in this field has grown rapidly. Broderick *et al.* had demonstrated second harmonic generation in 2D nonlinear PhC in lithium niobate [61]. Fleischer *et al.* had demonstrated the existence of two dimensional discrete solitons in optically induced nonlinear photonic lattices [62]. Nonlinear photonic crystals can show its high impact in signal processing by enhancing low energy signals which was impossible for the optics community in the past because of the weak ultra-fast nonlinear

effects. Geon Joon Lee *et al.* were the first to study the nonlinear optical enhancement in 1D PhC using ZnO as the defects [63]. Later, Tsurumachi *et. al.* demonstrated that the nonlinear optical properties of a 1D PhC can be greatly enhanced by localizing the electromagnetic field within a defect introduced in the PhC [64] and thereafter, enormous numbers of works have been reported [65-67].

In this thesis, nonlinear material $BaTiO_3$ (BTO) is placed in between two identical Bragg mirrors of one dimensional photonic crystal formed by low and high refractive indices of SiO_2 and TiO_2 respectively. We can observe the enhancement of nonlinear absorption coefficient due to the localization of photons and which is verified by the open aperture Z-scan technique. This enhancement of nonlinear optical properties is crucial for optical switches [68], optical limiting devices [69] and quantum cryptography [70], etc. BTO is an excellent choice for many applications such as capacitors [71], energy storage devices [72], piezoelectric [73] and photorefractive effect [74] due to its high dielectric constant. Moreover, BTO exhibits photorefractive effect which is suitable for storing erasable holograms [75,76]. Therefore, enhancing its nonlinear optical properties in the microcavity improves the holographic data storage at micron scales.

1.9 Applications of Photonic Crystals

PhCs play vital roles in optoelectronics and photonics and its application in this field is based on the suppression of spontaneous emission and localization of light. Both 2D and 3D PhCs are of great interest in the optics industry and extensive research is going on from its inception. PhC fiber (PCF) is a type of 2D PhC developed in the University of Bath, UK in 1996. Apart from the conventional optical fiber, PCF has the ability to confine light in its defect hollow cores and has to its credit a large variety of applications in numerous fields such as fiber lasers [77], nonlinear devices [78,79], fibre optic communications [80], high power transmissions [81] etc. 3D PhC has promising applications in micro-millimetre wavelength regime and it includes amplified photon absorption or emission, light bending,

inhibition of spontaneous emission etc. It plays a major role of enhancing light in dye-sensitized solar cells [82]. The ability to localize light in three dimensions has significance in quantum optical devices, realization of light emitting diodes (LEDs) and microelectronics fabrication technology [83,84]. The defect modes of photonic band gap structures can be used as filters [85], wave guides [86], optical limiting devices [87], optical delay lines [59], optical modulators [88], detectors [89] and nonlinear optical devices [90] etc.

Here we focus on unconventional 1D PhCs where the thickness of each layer differs from the Bragg's condition. First we fabricate two microcavities to understand the role of the defect layer by varying its thicknesses, the first microcavity is identical to the conventional microcavity and the defect layer of the second microcavity is higher than that of conventional microcavity, while the Bragg mirrors are identical in both the microcavities and it satisfies Bragg's condition of thickness. We then fabricate a third microcavity that completely differs from the Bragg's condition of its thickness both in Bragg mirror and the defect layer, which we have termed it as asymmetric microcavity. The aim of this thesis is to compare the results obtained in both conventional and unconventional microcavities.

1.10 Organization of the thesis

The thesis includes seven chapters. A short description of the remaining chapters is provided in the following.

Chapter 2: This chapter discusses various experimental techniques used in this study, such as fabrication and characterisation of photonic crystals using ellipsometer, UV-Visible-Near-IR spectrophotometer, field emission scanning electron microscopy (FESEM), Z-scan technique and photoluminescence spectrophotometer. It also explains the numerical analysis of the crystals using transfer matrix method, which is also been included in this chapter.

Chapter 3: In this chapter, we present the fabrication of 1D PhC by Sol-Gel method. Here 1D photonic crystal made up of multilayers (14 layers) of SiO_2-TiO_2 and SiO_2-SnO_2 are

explained with the preparation of respective sols. The optical characterisation using FESEM for morphology and UV-Visible-Near-IR spectrophotometer for reflection spectra are discussed. The consequence on the number of layers on photonic band gap and the dependence of photonic band gap on polarization is presented. Chapter concludes with the challenges in the fabrication of photonic crystals.

Chapter 4: The fabrication of one dimensional photonic microcavity (symmetric microcavity) by radio frequency sputtering technique is discussed here. The cavity enhancements in nonlinear absorption and photoluminescence of BTO in 1D photonic crystal comprising of 11 alternate layers of TiO_2 and SiO_2 are demonstrated. The reflection spectrum reveals a cavity resonance at 532 nm at an incident angle 32° and a Q-factor of the microcavity of 48. Photoluminescence of BTO is measured using spectrophotometer, while the enhancement in nonlinear absorption coefficient is verified from the open aperture Z-scan measurements using nanosecond (ns) laser. The angle tuned Z-scan measurements show saturable absorption which gets maximized at 32°. The enhancement of nonlinear absorption in the microcavity is expressed in terms of enhancement factor G, which is obtained to be about 16, by applying the spatial distribution of optical field. Our experimental results show good agreement with the simulated optical properties of the 1D PhC using optical transfer matrix formalism. The photoluminescence spectra of the reference layer and 1D PhC are compared.

Chapter 5: This chapter highlights the role of the thickness of microcavity for a given wavelength by fabricating two identical microcavities with different thickness of the defect layer followed by their optical characterization. Here BTO is placed in between the two Bragg mirrors of the 1D PhC comprising 11 alternate layers of TiO_2 and SiO_2 respectively. Photoluminescence of BTO in both cavities are measured using spectrophotometer, whereas the enhancement in nonlinear absorption coefficients of both cavities are measured using open aperture Z- scan technique with nanosecond (ns) laser and we compare the results in

both cases. Here we experimentally realize, as we increase the thickness of the defect layer, that there is a shift from reverse saturable absorption (RSA) to saturable absorption (SA) for the same intensity of the laser beam in response to the angle tuning of the sample. The spatial field distribution along the depth of the microcavities using transfer matrix simulation shows that it is in good agreement with the experimental results. The photoluminescence spectra of both reference layers and respective microcavities are compared.

Chapter 6: This chapter demonstrates the nonlinear optical absorption switching behaviour of BTO in asymmetric microcavity. It shows switching behaviour in nonlinear absorption from reverse saturable absorption to saturable absorption as we angle tune the sample. It also gives the enhancement in nonlinear absorption and photoluminescence of BTO in a 1D asymmetric photonic microcavity. The defect material BTO is sandwiched between the two Bragg mirrors of the microcavity composed of 9 layers of high and low refractive indices of titanium dioxide (TiO_2) and silicon dioxide (SiO_2) respectively. The enhancement in nonlinear absorption coefficient of BTO is verified from the open aperture Z-scan measurements using a nanosecond (ns) laser and photoluminescence is measured using spectrophotometer. For the design of the photonic 1D structures, the transfer matrix simulations and also the experimental results show that the same photonic band gap effect exists for asymmetric structures also. Here we are experimentally realizing abnormal behaviour in nonlinear absorption compared to conventional photonic crystal microcavity and when the thickness of the defect layer (BTO) goes higher, the SA behaviour dominates and obscures RSA behaviour. Our experimental results show good agreement with the simulated optical properties of the 1D asymmetric microcavity using optical transfer matrix method formalism.

Chapter 7: This chapter summarizes the results obtained in this dissertation work and a brief outline of some future directions and aspects.

1.11 References

[1] J. D. Joannopoulos, S. G. Johnson, J. N. Winn and R. D. Meade, “Molding the flow of light.” Princeton Univ. Press, Princeton, NJ (2008).

[2] Q. Gong and X. Hu, “Photonic crystals: principles and applications.” Jenny Stanford Publishing (2014).

[3] M. Soljačić and J. D. Joannopoulos, “Enhancement of nonlinear effects using photonic crystals.”, Nat. Mater. 3(4), pp211-219 (2004).

[4] E. Yablonovitch, “Inhibited spontaneous emission in solid-state physics and electronics.”, Phys. Rev. Lett. 58(20), p2059 (1987).

[5] S. John, “Strong localization of photons in certain disordered dielectric superlattices.”, Phys. Rev. Lett. 58(23), p2486 (1987).

[6] J. D. Joannopoulos, P. R. Villeneuve and S. Fan, “Photonic crystals: putting a new twist on light.”, Nature 386 (6621), pp143-149 (1997).

[7] J. N. Winn, Y. Fink, S. Fan and J. D. Joannopoulos, “Omnidirectional reflection from a one-dimensional photonic crystal.”, Opt. Lett. 23(20), pp1573-1575 (1998).

[8] H. Y. Lee and T. Yao, “Design and evaluation of omnidirectional one-dimensional photonic crystals.”, J. Appl. Phys. 93(2), pp819-830 (2003).

[9] L. D. Bonifacio, B. V. Lotsch, D. P. Puzzo, F. Scotognella and G. A. Ozin, “Stacking the nanochemistry deck: structural and compositional diversity in one-dimensional photonic crystals.”, Adv. Mater. 21(16), pp1641-1646 (2009).

[10] A. Yariv and P. Yeh, “Photonics: optical electronics in modern communications” New York: Oxford university press, 6 (2007).

[11] J. D. Joannopoulos, P. R. Villeneuve and S. Fan, “Photonic crystals.”, Solid State Commun. 102(2-3), pp165-173 (1997).

[12] S. Colodrero, M. Ocana and H. Míguez, “Nanoparticle-based one-dimensional photonic crystals.”, Langmuir, 24(9), pp4430-4434 (2008).

[13] Z. Yu, Z. Wang and S. Fan, “One-way total reflection with one-dimensional magneto-optical photonic crystals.”, Appl. Phys. Lett. 90(12), p121133 (2007).

[14] Y. Akahane, T. Asano, B. S. Song and S. Noda, “High-Q photonic nanocavity in a two-dimensional photonic crystal.”, Nature, 425(6961), pp944-947 (2003).

[15] D. N. Chigrin, S. Enoch, C. M. S. Torres and G. Tayeb, “Self-guiding in two-dimensional photonic crystals.”, Opt. Express, 11(10), pp1203-1211 (2003).

[16] Y. Xia, B. Gates and Z. Y. Li, “Self-assembly approaches to three-dimensional photonic crystals.”, Adv. Mater. 13(6), pp409-413 (2001).

[17] Y. A. Vlasov, K. Luterova, I. Pelant, B. Hönerlage and V. N. Astratov, “Enhancement of optical gain of semiconductors embedded in three-dimensional photonic crystals.”, Appl. Phys. Lett. 71(12), pp1616-1618 (1997).

[18] M. Scharrer, A. Yamilov, X. Wu, H. Cao and R. P. Chang, “Ultraviolet lasing in high-order bands of three-dimensional ZnO photonic crystals.”, Appl. Phys. Lett. 88(20), p201103 (2006).

[19] C. M. Soukoulis, “The history and a review of the modelling and fabrication of photonic crystals.”, Nanotechnology 13(3), p420 (2002).

[20] K. M. Ho, C. T. Chan and C. M. Soukoulis, “Existence of a photonic gap in periodic dielectric structures.”, Phys. Rev. Lett. 65(25), p3152 (1990).

[21] E. Yablonovitch, T. J. Gmitter, R. D. Meade, A. M. Rappe, K. Brommer and J. D. Joannopoulos, “Donor and acceptor modes in photonic band structure.”, Phys. Rev. Lett. 67(24), p3380 (1991).

[22] S. Noda, K. Tomoda, N. Yamamoto and A. Chutinan, “Full three-dimensional photonic bandgap crystals at near-infrared wavelengths.”, Science 289(5479), pp604-606 (2000).

[23] O. Toader and S. John, “Proposed square spiral microfabrication architecture for large three-dimensional photonic band gap crystals.”, Science 292(5519), pp1133-1135 (2001).

[24] J. W. Haus, H. S. Sözüer and R. Inguva, “Photonic bands: ellipsoidal dielectric atoms in an FCC lattice.”, J. Mod. Opt. 39(10), pp1991-2005 (1992).

[25] S. John and K. Busch, “Photonic bandgap formation and tunability in certain self-organizing systems.”, J. Light. Technol. 17(11), p1931 (1999).

[26] T. F. Krauss, “Planar photonic crystal waveguide devices for integrated optics.”, Phys. Status Solidi A 197(3), pp688-702 (2003).

[27] W. Zhang, G. Xu, J. Zhang, H. Wang and H. Hou, “Infrared spectrally selective low emissivity from Ge/ZnS one-dimensional heterostructure photonic crystal.”, Opt. Mater. 37, pp343-346 (2014).

[28] Y. F. Xiao, C. L. Zou, Y. Li, C. H. Dong, Z. F. Han and Q. Gong, “Asymmetric resonant cavities and their applications in optics and photonics: a review.”, Front. Optoelectron. 3(2), pp109-124 (2010).

[29] L. Nucara, F. Greco and V. Mattoli, “Electrically responsive photonic crystals: a review.”, J. Mater. Chem. C 3(33), pp8449-8467 (2015).

[30] S. Colodrero, M. Ocana and H. Míguez, “Nanoparticle-based one-dimensional photonic crystals.”, Langmuir 24(9), pp4430-4434 (2008).

[31] D. Zhou and R. Biswas, “Photonic crystal enhanced light-trapping in thin film solar cells.”, J. Appl. Phys. 103(9), p093102 (2008).

[32] M. E. Calvo, O. S. Sobrado, G. Lozano and H. Míguez, “Molding with nanoparticle-based one-dimensional photonic crystals: a route to flexible and transferable Bragg mirrors of high dielectric contrast.”, J. Mater. Chem. 19(20), pp3144-3148 (2009).

[33] Y. Fan, Z. Wei, H. Li, H. Chen and C. M. Soukoulis, “Photonic band gap of a graphene-embedded quarter-wave stack.”, Phys. Rev. B 88(24), p241403 (2013).

[34] L. D. Bonifacio, B. V. Lotsch, D. P. Puzzo, F. Scotognella and G. A. Ozin, “Stacking the nanochemistry deck: structural and compositional diversity in one-dimensional photonic crystals.”, Adv. Mater. 21(16), pp1641-1646 (2009).

[35] D. Urbonas, A. Balčytis, K. Vaškevičius, M. Gabalis and R. Petruškevičius, “Air and dielectric bands photonic crystal microringresonator for refractive index sensing.”, Opt. Lett. 41(15), pp3655-3658 (2016).

[36] C. M. Soukoulis, “Photonic crystals and light localization in the 21st century.”, Springer Science & Business Media 563 (2012).

[37] S. Lan, S. Nishikawa, Y. Sugimoto, N. Ikeda, K. Asakawa and H. Ishikawa, “Analysis of defect coupling in one-and two-dimensional photonic crystals.”, Phys. Rev. B 65(16), p165208 (2002).

[38] A. Lavrinenko, P. I. Borel, L. H. Frandsen, M. Thorhauge, A. Harpøth, M. Kristensen and H. M. H. Chong, “Comprehensive FDTD modelling of photonic crystal waveguide components.”, Opt. Express 12(2), pp234-248 (2004).

[39] A. Mekis, S. Fan and J. D. Joannopoulos, “Absorbing boundary conditions for FDTD simulations of photonic crystal waveguides.”, IEEE Microw. Wirel. Compon. Lett. 9(12), pp502-504 (1999).

[40] S. Shi, C. Chen and D. W. Prather, “Plane-wave expansion method for calculating band structure of photonic crystal slabs with perfectly matched layers.”, J. Opt. Soc. Am. A 21(9), pp1769-1775 (2004).

[41] J. Arriaga, J. C. Knight and P. S. J. Russell, “Modelling photonic crystal fibres.”, Physica E 17, pp440-442 (2003).

[42] J. Tang, H. J. Yang, Q. Xu, J. W. Liao, S. Yuan and Y. Hu, “Analysis of the transfer characteristics of one-dimensional photonic crystal and its application with transfer matrix method.”, Infrared Laser Eng. 39(1), pp76-80 (2010).

[43] R. Srivastava, K. B. Thapa, S. Pati and S. P. Ojha, “Omni-direction reflection in one dimensional photonic crystal.”, Prog. Electromagn. Res. 7, pp133-143 (2008).

[44] M. Campbell, D. N. Sharp, M. T. Harrison, R. G. Denning and A. J. Turberfield, “Fabrication of photonic crystals for the visible spectrum by holographic lithography.”, Nature 404(6773), pp53-56 (2000).

[45] D. Chanda, L. Abolghasemi and P. R. Herman, “One-dimensional diffractive optical element based fabrication and spectral characterization of three-dimensional photonic crystal templates.”, Opt. Express 14(19), pp8568-8577 (2006).

[46] X. Xiao, W. Wenjun, L. Shuhong, Z. Wanquan, Z. Dong, D. Qianqian and Z. Bingyuan, “Investigation of defect modes with Al_2O_3 and TiO_2 in one-dimensional photonic crystals.”, Optik 127(1), pp135-138 (2016).

[47] M. E. Calvo, S. Colodrero, N. Hidalgo, G. Lozano, C. López-López, O. Sánchez-Sobrado and H. Míguez, "Porous one dimensional photonic crystals: novel multifunctional materials for environmental and energy applications.", Energy Environ. Sci. 4(12), pp4800-4812 (2011).

[48] J. Riedrich-Möller, L. Kipfstuhl, C. Hepp, E. Neu, C. Pauly, F. Mücklich and S. Gsell, "One-and two-dimensional photonic crystal microcavities in single crystal diamond.", Nat. Nanotechnol. 7(1), p69 (2012).

[49] A. R. M. Zain, N. P. Johnson, M. Sorel and M. Richard, "Ultra high quality factor one dimensional photonic crystal/photonic wire micro-cavities in silicon-on-insulator (SOI).", Opt. Express 16(16), pp12084-12089 (2008).

[50] K. M. Chen, A. W. Sparks, H. C. Luan, D. R. Lim, K. Wada and L. C. Kimerling, "SiO_2 /TiO_2 omnidirectional reflector and microcavity resonator via the sol-gel method.", Appl. Phys. Lett. 75(24), pp3805-3807 (1999).

[51] H. Y. Lee and T. Yao, "Design and evaluation of omnidirectional one-dimensional photonic crystals.", J. Appl. Phys. 93(2), pp819-830 (2003).

[52] S. Chen, Z. Song, Y. Wang and D. Yao, "Preparation of one-dimensional photonic crystal with variable period by using ultra-high vacuum electron beam evaporation.", Microelectron J 38(2), pp282-284 (2007).

[53] T. Baba, "Slow light in photonic crystals.", Nat. Photonics 2(8), p465 (2008).

[54] T. F. Krauss, "Slow light in photonic crystal waveguides.", J. Phys. D 40(9), p2666 (2007).

[55] J. Sancho, J. Lloret, I. Gasulla, S. Sales and J. Capmany, "Fully tunable 360° microwave photonic phase shifter based on a single semiconductor optical amplifier.", Opt. Express 19(18), pp17421-17426 (2011).

[56] D. M. Beggs, T. P. White, L. O'Faolain and T. F. Krauss, “Ultracompact and low-power optical switch based on silicon photonic crystals.”, Opt. Lett. 33(2), pp147-149 (2008).

[57] M. G. Wickham, G. W. Holleman and S. J. Brosnan, U.S. Patent No. 6,301,421. Washington, DC: U.S. Patent and Trademark Office (2001).

[58] H. Li, J. Wang, H. Lin, L. Xu, W. Xu, R. Wang and D. Zhu, “Amplification of fluorescent contrast by photonic crystals in optical storage.”, Adv. Mater. 22(11), pp1237-1241 (2010).

[59] B. Ben Bakir, C. Seassal, X. Letartre, P. Viktorovitch, M. Zussy, L. Di Cioccio and J. M. Fedeli, “Surface-emitting microlaser combining two-dimensional photonic crystal membrane and vertical Bragg mirror.”, Appl. Phys. Lett.88(8), p081113 (2006).

[60] Z. Wang and S. Fan, “Compact all-pass filters in photonic crystals as the building block for high-capacity optical delay lines.”, Phys. Rev. E 68(6), p066616 (2003).

[61] N. G. R. Broderick, G. W. Ross, H. L. Offerhaus, D. J. Richardson and D. C. Hanna, “Hexagonally poled lithium niobate: a two-dimensional nonlinear photonic crystal.”, Phys. Rev. Lett. 84(19), p4345 (2000).

[62] J. W. Fleischer, M. Segev, N. K. Efremidis and D. N. Christodoulides, “Observation of two-dimensional discrete solitons in optically induced nonlinear photonic lattices.”, Nature, 422(6928), pp147-150 (2003).

[63] G. J. Lee, Y. P. Lee, S. G. Jung, C. K. Hwangbo, S. Kim and I. Park, “Linear and nonlinear optical properties of one-dimensional photonic crystals containing ZnO defects.”, J. Appl. Phys. 102(7), p073528 (2007).

[64] N. Tsurumachi, S. Yamashita, N. Muroi, T. Fuji, T. Hattori and H. Nakatsuka, “Enhancement of nonlinear optical effect in one-dimensional photonic crystal structures.”, Jpn. J. Appl. Phys. 38, pp6302–6308 (1999).

[65] G. J. Schneider and G. H. Watson, “Nonlinear optical spectroscopy in one-dimensional photonic crystals.”, Appl. Phys. Lett. 83, pp5350-5352 (2003).

[66] J. Shen, Z. Zhang, Z. Hua, G. Ma and S. H. Tang, “Observation of two-photon absorption enhancement at double defect modes in one-dimensional photonic crystals.”, Appl. Phys. Lett. 88, p011113 (2006).

[67] H. Inouye and Y. Kanemitsu, “Direct observation of nonlinear effects in a onedimensional photonic crystal.”, Appl. Phys. Lett. 82, pp1155-1157 (2003).

[68] C. Liao, H. Zhang, L. Tang, Z. Zhou, C. Lv, Y. Cui and J. Zhang, “Nonlinear optical response of semiconductor-nanocrystals-embedded photonic band gap structure.”, Appl. Phys. Lett. 104, p171901 (2014).

[69] A. Mecozzi, S. Trillo and S. Wabnitz, “Spatial instabilities, all-optical limiting, and thresholding in nonlinear distributed-feedback devices.”, Opt. Lett. 12, pp1008-1010 (1987).

[70] H. G. Schuster, “Nonlinear laser dynamics: from quantum dots to cryptography.”, John Wiley & Sons (2012).

[71] M. E. Lines and A. M. Glass, “Principles and applications of ferroelectrics and related materials.”, Oxford university press (1977).

[72] J. Li, J. Claude, L. E. Norena-Franco, S. I. Seok and Q. Wang, “Electrical energy storage in ferroelectric polymer nanocomposites containing surface-functionalized $BaTiO_3$ nanoparticles.”, Chem. Mater. 20, pp6304–6306 (2008).

[73] K. I. Park, S. Xu, Y. Liu, G. T. Hwang, S. J. L. Kang, Z. L. Wang and K. J. Lee, “Piezoelectric $BaTiO_3$ thin film nanogenerator on plastic substrates.”, Nano Lett. 10, pp4939–4943 (2010).

[74] D. D. Nolte, “Photorefractive effects and materials.”, Springer Science & Business Media (2013).

[75] J. Feinberg, D. Heiman, A. R. Tanguay and R. W. Hellwarth, “Photorefractive effects and light- induced charge migration in barium titanate.”, J. Appl. Phys. 51, p12971305 (1980).

[76] R. L. Townsend and J. T. LaMacchia, “Optically induced refractive index changes in $BaTiO_3$.”, J. Appl. Phys. 41, pp5188-5192 (1970).

[77] J. Limpert, O. Schmidt, J. Rothhardt, F. Röser, T. Schreiber, A. Tünnermann and F. Salin, “Extended single-mode photonic crystal fiber lasers.”, Opt. Express 14(7), pp2715-2720 (2006).

[78] L. Fu, A. Jain, H. Xie, C. Cranfield and M. Gu, “Nonlinear optical endoscopy based on a double-clad photonic crystal fiber and a MEMS mirror.”, Opt. Express 14(3), pp1027-1032 (2006).

[79] M. Vieweg, T. Gissibl, S. Pricking, B. T. Kuhlmey, D. C. Wu, B. J. Eggleton and H. Giessen, “Ultrafast nonlinear optofluidics in selectively liquid-filled photonic crystal fibers.”, Opt. Express 18(24), pp25232-25240 (2010).

[80] F. Gerome, J. L. Auguste and J. M. Blondy, “Design of dispersion-compensating fibers based on a dual-concentric-core photonic crystal fiber.”, Opt. Lett. 29(23), pp2725-2727 (2004).

[81] D. Nodop, C. Jauregui, D. Schimpf, J. Limpert and A. Tünnermann, “Efficient high-power generation of visible and mid-infrared light by degenerate four-wave-mixing in a large-mode-area photonic-crystal fiber.”, Opt. Lett. 34(22), pp3499-3501 (2009).

[82] A. Mihi and H. Míguez, “Origin of light-harvesting enhancement in colloidal-photonic-crystal-based dye-sensitized solar cells.”, J. Phys. Chem. B 109(33), pp15968-15976 (2005).

[83] K. N. Hui, W. Y. Fu, W. N. Ng, C. H. Leung, P. T. Lai, K. K. Y. Wong and H. W. Choi, "Polychromatic light-emitting diodes with a fluorescent nanosphere opal coating.", Nanotechnology 19(35), p355203 (2008).

[84] S. Y. Lin, J. G. Fleming, D. L. Hetherington, B. K. Smith, R. Biswas, K. M. Ho and J. Bur, "A three-dimensional photonic crystal operating at infrared wavelengths.", Nature 394(6690), pp251-253 (1998).

[85] S. R. Entezar, "Photonic crystal wedge as a tunable multichannel filter.", Superlattices and Microstruct. 82, pp33-39 (2015).

[86] K. A. Atlasov, M. Felici, K. F. Karlsson, P. Gallo, A. Rudra, B. Dwir and E. Kapon, "1D photonic band formation and photon localization in finite-size photonic-crystal waveguides.", Opt. Express 18(1), pp117-122 (2010).

[87] X. Hu, P. Jiang, C. Ding, H. Yang and Q. Gong, "Picosecond and low-power all-optical switching based on an organic photonic-bandgap microcavity.", Nat. Photonics 2(3), p185 (2008).

[88] S. Schönenberger, T. Stöferle, N. Moll, R. F. Mahrt, M. S. Dahlem, T. Wahlbrink and B. J. Offrein, "Ultrafast all-optical modulator with femtojoule absorbed switching energy in silicon-on-insulator.", Opt. Express 18(21), pp22485-22496 (2010).

[89] H. Shirai, K. Ishii, H. Miyagawa, S. Koshiba, S. Nakanishi and N. Tsurumachi, "Efficient terahertz emission, detection, and ultrafast switching using one-dimensional photonic crystal microcavity.", J. Opt. Soc. Am. B 31(6), pp1393-1401 (2014).

[90] T. Stomeo, G. Epifani, V. Tasco, A. Massaro, I. Tarantini, A. Campa and C. Sibilia, "Fabrication of GaN/AlGaN 1D photonic crystals designed for nonlinear optical applications.", Photonic Crystal Materials and Devices IX 7713, p771316(2010).

Chapter 2

Experimental Methods and Numerical Modelling

This chapter explains two different methods of fabrication of one dimensional photonic crystals namely the Sol-Gel technique and the RF Sputtering method and its characterization using field emission scanning electron microscopy, UV/Visible spectrophotometer, Photoluminescence spectrometer, Z-scan etc. It also discusses the numerical analysis of the microcavity properties using transfer matrix simulation.

2.1 Introduction

Photonic crystals are periodically patterned electromagnetic media that often possess photonic band gap, where a range of frequency for which light is not permitted to propagate through the structure. Photonic crystals offer unique ways to tailor light and the propagation of electromagnetic waves [1-3]. Our design for a microcavity is based on 1-Dimensional Photonic Crystal (1D PhC) structures that comprise a defect layer (also known as spacer layer) of $BaTiO_3$ (BTO) sandwiched between two Bragg mirrors made up of alternate layers of high contrast dielectric materials such as SiO_2 and TiO_2. This Bragg mirror is also called as distributed Bragg reflectors (DBR) for obvious reasons. Here the thicknesses of the alternative and defect layers are made equal to the quarter-wave and half-wave lengths of a given electromagnetic field respectively. This chapter discusses the numerical analysis of the desired microcavity and the experimental techniques used to fabricate them and to characterize their physical properties. Sol-Gel and Radio Frequency Magnetron Sputtering (RFMS) thin film deposition techniques are adopted to fabricate the structures. Importantly, Sol-Gel is a chemical deposition method while the RFMS is a physical vapour deposition process. The physical properties of the fabricated 1D PhC are characterised using Field Emission Scanning Electron Microscopy (FESEM) for the cross-sectional morphology, while UV/Visible Spectrophotometer and Z-scan are used for studying linear and non-linear optical properties of the materials respectively.

2.2 Refractive index and thickness measurements of thin films using Ellipsometer

Ellipsometry is a well-known technique to measure the refractive index of thin films [4,5] that works on the principle of the polarization changes due to Fresnel reflection. Such polarization change is a function of complex refractive index or dielectric function, and hence one can obtain the refractive index of the thin film using proper data fitting. The experimental set up of the commercially available ellipsometer (J. A. Woollam, M2000V) is shown in Figure 2.1. Electromagnetic radiation from the light source is linearly polarised by a

polarizer, and it falls on to the sample. After reflection from the sample it passes through a compensator and a second polarizer called analyzer before it falls on the detector. The experimental data are expressed in terms of two parameters ψ and Δ, where ψ is the amplitude and Δ is the phase difference. When light is incident upon the sample at an angle of incidence ϕ_0, the polarization state of the sample may be decomposed in to 's-' and 'p-' components. If I_s and I_p are intensity of 's-' and 'p-' components after reflection, the ellipsometry equation is defined as

$$\rho = \frac{I_p}{I_s} = \tan\psi e^{i\Delta} \qquad (2.1)$$

Where ρ is the complex reflectance ratio. The experimentally measured ψ and Δ is converted into optical constants by using a model analysis.

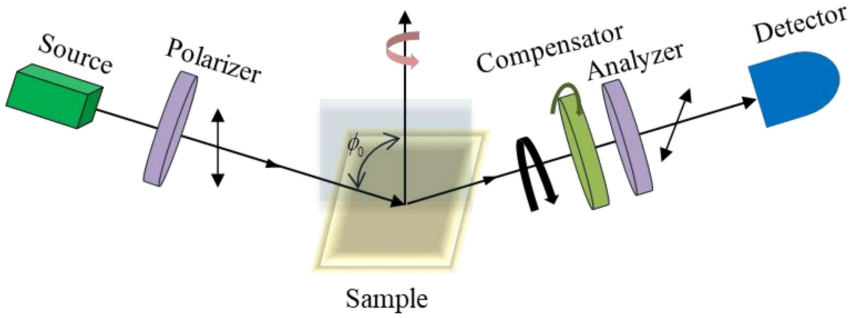

Figure 2.1: *Schematic diagram of the Ellipsometer*

2.3 Fabrication techniques of 1-Dimensional photonic crystal

First successful creation of the photonic crystal was done by E. Yablonovitch in 1987 by simply piercing holes in a block of a material with similar dielectric characteristics of silicon [1]. It was a 3-D photonic band crystal. Colloidal self-assembling is another technique

of fabricating 3-D photonic crystal, which is the process of assembling monodispersed sub-micron spheres arranged by sedimentation into face centered cubic lattices (fcc). Due to the presence of spherical Brillouin zones, fcc lattices have largest photonic band gap when compared to other crystalline structures. E-beam lithography is one of the techniques of fabricating 2-D photonic crystal [6-8]. It is the process of drilling holes in the substrate and filling the space with another material having relatively high dielectric constant and then depositing another layer of substrate. This process is repeated until the desired pattern of photonic crystal is obtained.

The simplest type of 1D PhC is a quarter wavelength multilayers of two dielectric materials with high refractive index contrast, commonly referred to as a Bragg mirror. Each layer of the Bragg mirror is having an optical thickness $nd = \lambda/4$, where n is the refractive index, d is thickness of each layer and λ is the working wavelength of the optical field. It is possible to construct a microcavity using two parallel Bragg mirror separated by a defect layer of relatively high refractive index and half wavelength thickness [9]. The reflection or transmission spectrum of microcavities exhibits a wide band gap with a narrow passband at the working wavelength. Various techniques were developed for the fabrication of 1D PhC such as holographic lithography [10,11], etching methods [12,13], chemical vapour deposition method [14,15], Sol-Gel method [16-18], RF Sputtering [19-21] etc.

Sol-Gel and RF Sputtering are the two techniques discussed in the following sections. Sol-Gel is a low-cost fabrication method which helps to incorporate variety of materials including semiconductor quantum dots and nanomaterials. By adjusting the speed of rotation of spin coater and viscosity of the solution, the desirable microcavity with low thickness (of the order of nm) can be constructed. RF sputtering provides thin films of better quality and uniformity in each layer. It helps in deposition of thin films of metals, insulators, alloys etc., and this technique is used to sputter all types of films.

2.3.1 Sol-Gel method

Sol-Gel is a wet chemical fabrication method of producing solid materials from smaller molecules that is based on a chemical transformation of liquid alkoxide precursors into solid-state products by hydrolysis and polymerization reactions at room temperature [22]. Oxide-based dielectric materials are suitable for fabricating photonic band gap (PBG) structures, as they exhibit wide range of transparency from ultraviolet to near infra-red regions [23]. More importantly, Sol-Gel is a convenient method to dope each layer with variety of materials like organic molecules, semiconductor nano-crystals, quantum dots etc [24]. For example, it was used to fabricate the defect photonic crystal microcavity with nonlinear optical materials such as ZnO, CdSe and semiconductor quantum dots of CdS, ZnS etc [25-27], and also developed the 1D PhC microcavity with rare-earth doped materials such as Eu^{3+}, Er^{3+}, Yb^{3+} [28-30].

Sol-Gel is a low cost and simple method to fabricate the nano/micro layers with a large variety of materials in room temperature, and it gives uniform distribution of components and porosity. It can be used to deposit very thin films of metal oxides. However, great advantages always bring unavoidable disadvantages, and the major disadvantage of Sol-Gel method is the cracking of the layers possibly due to the internal stresses and thermal expansion. It is also very sensitive to moisture and requires longer processing time.

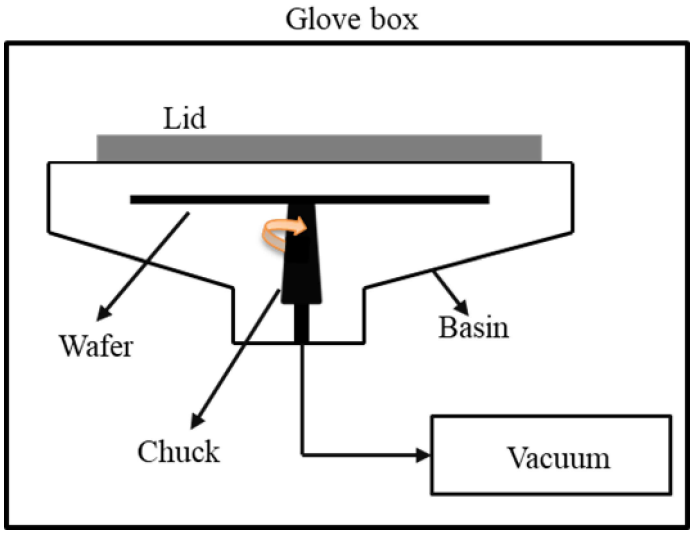

Figure 2.2: *The schematic diagram of Sol-Gel using spin coater placed inside the glove box*

SiO_2, TiO_2 and SnO_2 dielectric materials are chosen here for the fabrication of 1D PhC as they are transparent and provide high refractive index contrast between the adjacent layers for a given wavelength (532 nm). It also provides higher reflectivity of the stop band. These materials are included in liquid phase during the sol fabrication. Sol is a stable distribution of colloidal particles of polymers in a solvent. First, the precursor sol is converted into multi-layered films by depositing on the substrate containing stop band in the visible region using a spin coater (SPIN 150). Every layer of coating is followed by an annealing process using a furnace (YUDIAN Al-508) at a low temperature in the range $50℃ - 70℃$. This process typically results in shrinkage and densification of the layers. The whole set up is isolated from the outer atmosphere using a locally developed glove box. The schematic diagram of Sol-Gel technique is shown in Figure 2.2. Here a spin coater and a furnace are kept inside the glove box. The vacuum pump attached to the glove box creates vacuum inside the chamber before the deposition process starts. The rotary pump attached to the spin coater can also

make vacuum inside the spin coater. The thickness of the film can be varied by adjusting the spinning speed of the wafer. The formation of each layer is by the centrifugal force on the spinning substrate.

2.3.2 Radio Frequency (RF) Magnetron Sputtering Technique (RFMS)

RF Sputtering is a physical vapour deposition process on a substrate such as glass plate or silicon wafers, where the depositing material molecules are ejected from their respective target via the strong collision of inert gas ions [31]. RF sputtering prevents this building up of positive charges on the materials. There is powerful magnet just below the target to confine the plasma towards the target. This rapidly increases the collision rate and maintains higher deposition of atoms on the substrates.

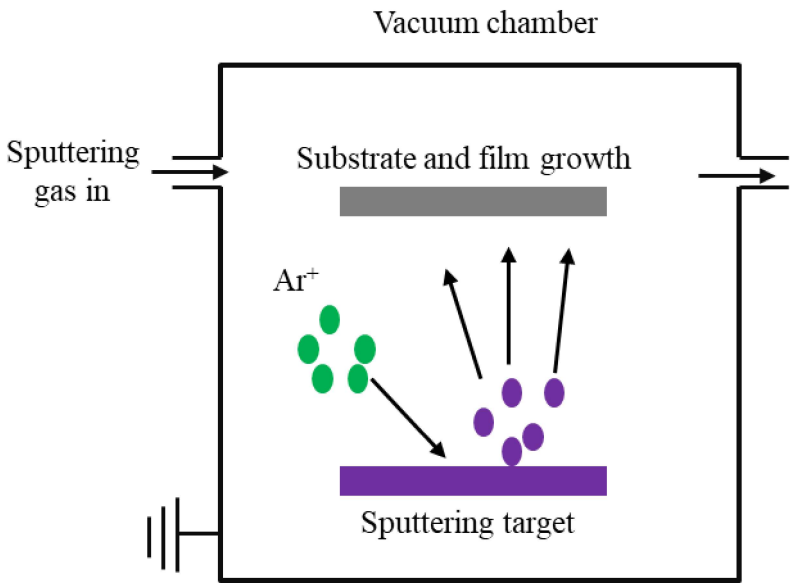

Figure 2.3: *Schematic diagram of RF sputtering process*

The schematic diagram of RF sputtering system is shown in Figure 2.3 which consists of a target (acts as cathode) and a substrate (acts as anode) inside the vacuum chamber. Here the

material is sputtered from the target by Argon ions which are accelerated by RF electric field. Targets and substrates are placed inside a vacuum chamber, which is pumped down to a residual pressure of 4.9×10^{-6} mbar.

Argon gas is filled in the chamber up to a pressure of 5.5×10^{-3} mbar before the sputtering process. When a negative voltage is applied to the target, it results in the formation of plasma discharge or a glow. These positively charged gas ions are directed towards the target at very high speed. As a result of this collision by high energetic ions with the target, atoms are ejected from the target, which are transported to the substrate and condense to form thin films on the substrates.

The alternating dielectric layers of SiO_2 and TiO_2 with an optical thickness of $\lambda/4$ are fabricated by multi-target RF sputtering system (Advanced Process Technology, India). The dimensions of the SiO_2 and TiO_2 targets are 50mm diameter and 3 mm thickness with RF powers of 150W and 130W respectively. BTO is used as the spacer layer with the same dimension with RF power 50W.

Sputter coating is extensively used for industrial applications such as deposition of thin films of various materials in integrated circuit processing [32], semiconductor industry [33]. Thin antireflection coating in glass for optical application is done by sputtering [34]. The deposition of thin layer of conducting materials on different specimen can be done with the RF sputtering systems. The major advantage of sputtering is even materials with high melting points also possess high sputtering yield. RF sputtering is more efficient than DC sputtering for the non-conducting materials. For non-conducting materials there is a chance of piling up of positive charges on the materials if DC sputtering is employed and it will stop sputtering.

2.4. Characterization of 1-Dimensional Photonic Crystals

Different techniques were used to ascertain the morphological, linear and nonlinear optical properties of the materials. Commonly used techniques include UV/Visible-Near-IR spectrophotometer, field emission scanning electron microscope (FESEM), photoluminescence spectrophotometer, white light ellipsometer etc. Here, a UV/Visible-Near-IR spectrophotometer is used for the linear absorption, transmission and reflection studies of 1DPhC, while Z-scan technique is used to characterize the nonlinear absorption coefficients. The multi-layer structure and cross-sectional morphology is probed by a FESEM.

2.4.1 UV-Visible-Near-IR Spectrophotometer

The transmission and reflection measurements are carried out using a UV-Visible-Near-IR double beam spectrophotometer (JASCO V-670). It has two light sources, a deuterium (D_2) lamp and halogen lamp (W Lamp). Deuterium lamp covers the ultraviolet region while halogen lamp covers visible and near-infrared regions. It employs a single monochromatic design and covers a wavelength range 190 to 2700 nm. The monochromator comprises a dual grating. For UV/Visible region it consists of 1200 grooves/mm and 300 grooves/mm for Near-IR region. Correspondingly there are two detectors: A PMT detector for the UV/Visible region and a Peltier-cooled lead sulphide (PbS) detector for Near-IR region.

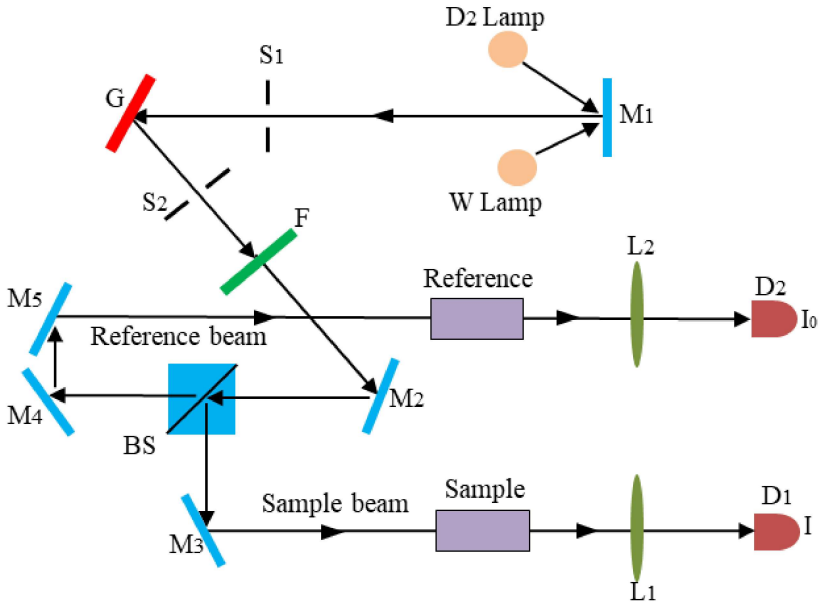

Figure 2.4: *Schematic diagram of the optical system of the JASCO V-670 UV-Visible-Near-IR spectrophotometer: M- Mirror, S- Slit, G- Grating, F-Filter, L- Lens, BS- Beam Splitter, D- Detector.*

The schematic diagram of the optical system of the JASCO model V-670 UV-Visible-Near-IR spectrophotometer is shown in Figure 2.4. The light coming from the source is directed to the grating G through the slit S_1 after the reflection from the mirror M_1. A specific wavelength can be selected by the rotation of grating. A monochromatic beam is passed through the slit S_2 by a proper orientation of the grating. The higher-order diffraction beam can be eliminated by using filter F. Before the beam gets split by the beam splitter (BS), the light beam is incident on a second mirror M_2. There is partial reflection and transmission at BS. The transmitted ray passes through the reference (air) while the reflected ray passes through the sample. The intensities of the light beams are measured at the end as shown in the figure. The ratio of the sample signal to the reference signal (I / I_0) is computed by the photometer to obtain the transmittance. There are three measurement accessories that are

attached with the spectrophotometer: variable angle transmittance, fixed angle and variable angle reflectance. An aluminium mirror is used for the standard reference sample.

It is important to notice the possibility of carrying out the polarization-dependent studies in the reflection mode, and polarization-dependent spectral characteristics with s-, p- and un-polarized light. It is also possible to mount the sample, reflecting mirror and detector on a single rotational stage. The detector is furnished with an integrating sphere, thus enabling the measurement of the relative reflectance of a diffusely reflecting sample. Using Glan-Taylor prism polarizer the polarization of the beam can be selected. However, it only permits measuring the reflectance from 5^0 to 70^0 only, due to aperture limitation

2.4.2 Field Emission Scanning Electron Microscopy (FESEM)

FESEM is an analytical technique that uses to probe nano level information about the surface morphology and the material's composition**.** Electrons coming from a field emission source are used rather than light as they exhibit much shorter wavelength and hence enables us to extract the nano-structure. In optical microscopes the resolution is limited by the wavelength of the light used. The resolution is also limited due to the lens aberrations. The FESEM offers higher resolution, in comparison with other optical microscopes due to the short de-Broglie wavelength of electrons. The de-Broglie wavelength of an electron accelerated by a potential V is given by the well-known formula $\lambda = \frac{h}{\sqrt{2m_0 eV}}$ in the non-relativistic case, where h is Planck's constant, m_0 is the rest mass of electrons and e is the charge of electron. The equation is in good agreement for potentials below 100keV, and more specifically, for a potential that varies from $1keV$ to $30keV$, the de-Broglie wavelength is in the range $38pm$ to $7pm$.

The use of magnetic correction lenses in modern FESEM compensates for these errors, which results in resolutions better than 0.1nm. At low and high electron energy it provides narrow

probing beams. This results in decreased charging, improved spatial resolution and minimised damage of the sample. The sample is scanned by the electrons according to a zig-zag pattern. There are two different types of emission sources of electron: thermionic emission source and field emission source. In FESEM it uses field emission type source. In thermionic emitters, the filament is heat up by the electrical current which is made up of either Tungsten (W) or Lanthanum Hexaboride (LaB_6). The electrons can be emitted from the materials when the heat is enough to overcome the work function of the materials. Most of the thermionic emitters have low brightness and thermal drift during its process. In field emission it can generate electrons by itself and there is no heating of the filament, thus avoiding the above mentioned problems.

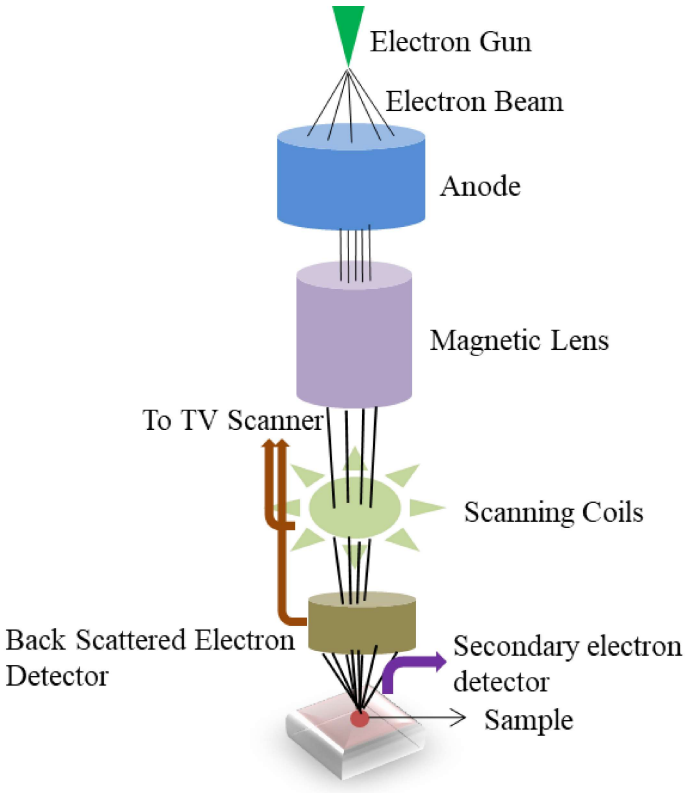

Figure 2.5: *Schematic diagram of field emission scanning electron microscope.*

Figure 2.5 shows the schematic diagram of FESEM. It has a field emission gun (FEG) for the emission of electrons. Since it does not heat the filament it is also called as 'cold' cathode field emitter. It starts emission when the filament is placed inside the large electrical potential gradient. The FEG made up of a tungsten (W) wire modified into a sharp point. The tip radius is nearly 100nm and it helps to concentrate the electric field to an extreme level. The image formed by the FESEM is from the auger electrons, characteristic X-rays, backscattered electrons and secondary electrons which are emitted by the sample.

The sharp pointed end of the FEG (cathode) is held at large negative potential relative to nearby anode. The field electron emission is caused by the potential gradient at the emitter surface. FEG is a Schottky type emitter which contains coating of zirconium oxide on the tip of the tungsten wire. The condenser magnetic lens in the setup is used to focus the beam of electron emitted from the tungsten to very small spot size of about 1 nm to 5 nm. The beam passes through the secondary coils which focus the electron beam over the object according to a zig-zag pattern. The incident beam generates low energy secondary electrons from the sample. These secondary electrons are sensed by scintillator-photomultiplier tube which converts it in to digital image, which can be processed further.

2.4.3 Photoluminescence Spectrometer

Photoluminescence (PL) spectroscopic technique is a well-known method based on photo-excitation for the optical and electronic characterization of semiconductors and other materials. It causes the electrons to excite to an upper energy state, and as a result of relaxation to a ground state, energy gets released. The physical mechanism behind PL emission is exposed in Figure 2.6. The electron in the valence band absorbs photon and the electron gets promoted to certain vibrational levels of the electronic excited states shown in dotted lines. The excited electron quickly relaxes to conduction band via non-radiative transition. The emission of photon takes place when it makes a transition from conduction band to valence band.

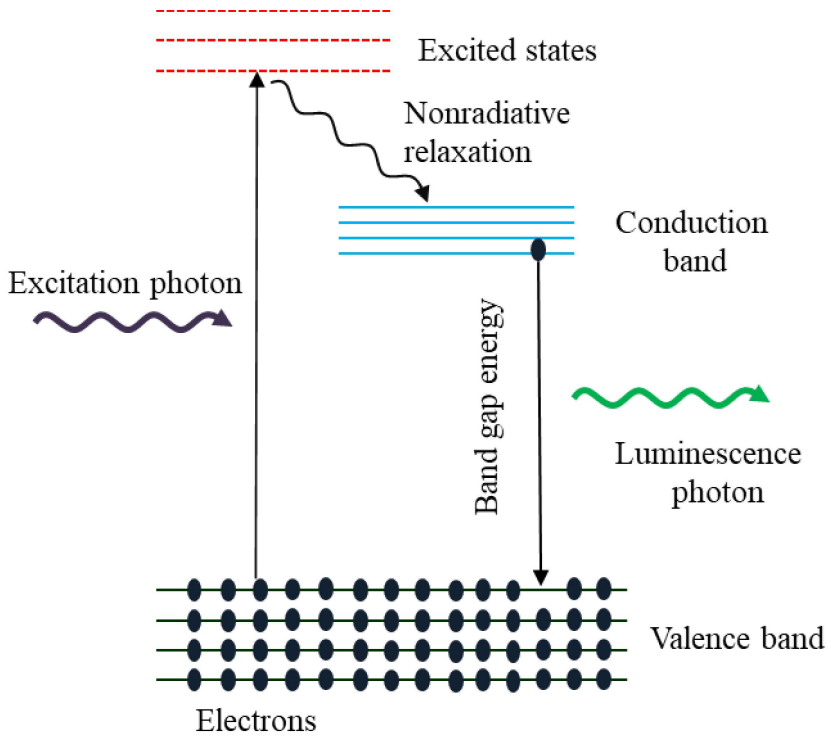

Figure 2.6: *The Schematic diagram of photoluminescence emission.*

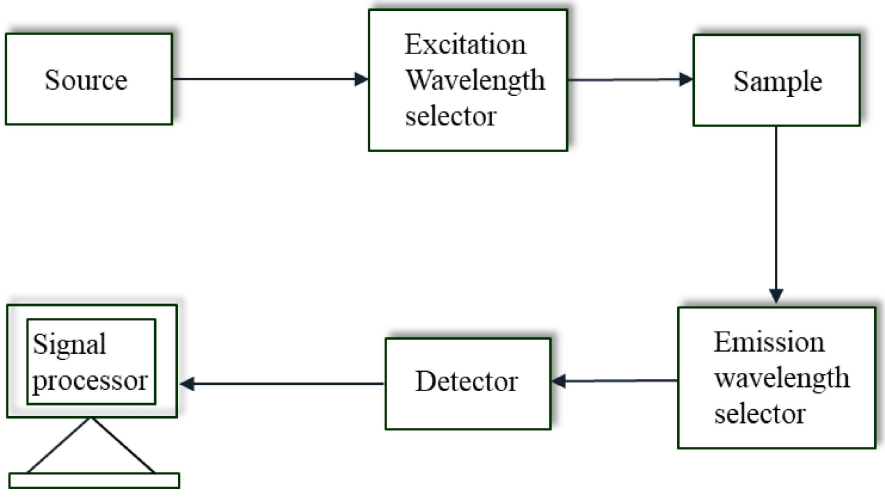

Figure 2.7: *Block diagram of PL spectrometer*

We use commercially available spectrometer (Fluorolog, Horiba Jobin Yvon), which consists of a powerful lamp (450 W Xe lamp) as a source which provides a broad spectrum of wavelengths for excitation (240-600 nm), and a double monochromator to reject stray light and provide high spectral resolution. The emission by the sample from 290 nm to 850 nm is detected by an ultra-sensitive PMT detector. The block diagram of PL spectrometer is displayed in Figure 2.7.

2.5 Measurement of Nonlinear optical properties

Nonlinear optics has enhanced our knowledge of understanding the fundamentals of light-matter interactions. Unlike linear optics, if intensity of light is high enough then the material produces vibrations of all the frequencies corresponding to different energy levels. Z-scan is one of the widely accepted methods to explore the nonlinear optical properties which is discussed below. Since this technique is simple and easy to interpret, it has gained quick acceptance by the nonlinear optics community. The applications of nonlinear optics can be seen in all the emerging photonic devices.

2.5.1 Z-scan technique

It is a single beam technique used to determine the complex nonlinear refractive index of the material [35]. Here a laser beam of gaussian profile is tightly focused to nonlinear medium and transmittance is measured either through a finite aperture (closed aperture) or without an aperture (open aperture). The closed aperture Z-scan determines the real part of the nonlinear refractive index while the open aperture Z-scan is used to measure the imaginary part of the nonlinear refractive index and the nonlinear absorption coefficient of the material. The presence of far-field aperture in the closed aperture mode helps to detect the small beam distortions in the original beam. The nonlinear material will act like a weak lens and the focal power is decided by the nonlinear refractive index. Hence it is possible to compute the nonlinear optical index from the Z-dependent transmission spectrum. When the aperture is

removed in open-aperture case the detector measures the whole signal from the sample, and hence the nonlinear absorption.

The Open aperture (OA) and closed aperture (CA) Z-scan profiles can be analysed approximating the laser beam to be a Gaussian. The intensity distribution of a Gaussian laser beam (TEM_{00}) propagating along the positive Z direction can be expressed as

$$I(z,r;t) = (I_0/(1+\frac{Z^2}{{Z_r}^2}))\exp(-2r^2/w^2(z))\ \exp(-t^2/\tau^2) \qquad (2.2)$$

where I_0 denotes the intensity of laser at focus, $Z_r(=\frac{\pi {w_0}^2}{\lambda})$ is the Rayleigh length, with a beam waist at the focus w_0 , λ is the excitation wavelength, τ is the pulse width and *w(z)* represents the beam waist at *z* which can be expressed as $w^2(z) = {w_0}^2(1+\frac{Z^2}{{Z_r}^2})$.

The OA Z-scan normalized transmittance *T(Z)* is represented by

$$T(z) = \sum_{m=0}^{\infty} \frac{\left[\frac{-q}{1+(\frac{Z}{Zr})^2}\right]^m}{(m+1)^{3/2}} \qquad (2.3)$$

For two photon absorption process (*m=1*), q is equal to $\beta I L_{eff}$, where I denotes the laser intensity measured at the focus and effctive sample length, $L_{eff} = \frac{1-e^{-\alpha_0 L}}{\alpha_0}$ (where L is the sample length).

The normalized transmittance for closed aperture (CA) Z-scan measurement is given by

$$T(z) = 1 - \frac{4x\Delta\phi}{(1+x^2)(9+x^2)} \qquad (2.4)$$

where $x = Z/Z_r$ and $\Delta\phi$ is the nonlinear phase shift. The nonlinear refractive index (n_2) can be obtained from

$$n_2 = \frac{|\Delta\phi|\lambda}{2\pi I L_{eff}} \quad \text{(in cm}^2\text{/W)} \qquad (2.5)$$

Both OA and CA Z-scan measurements were standardised using reference samples CS_2.

2.5.2 Experimental set-up for Open aperture Z-scan: measurement of nonlinear optical absorption

The multi-photon (two or more) absorption is the main cause of nonlinear absorption. This multi-photon absorption leads to an enhancement in the the valley of the Z-scan curve while the opposite effect (peak) can be observed for the saturable absorption. The refractive nonlinearities of a material can be drawn from a division of the transmission through an aperture by the nonlinear absorption recorded without any aperture. This division leads to a normalization and cancels the effects due to any nonlinear absorption. The schematic diagram of the OA Z-scan is given in Figure 2.8. A spatially filtered input laser beam is focused with lens L1, and 1D PhC sample is moved through the focus such that the sample stage is connected to a stepper motor. Another lens L2 is used to collect the transmitted light, which is focused on a photodiode placed after the neutral density filters. The error originating from the power level fluctuations of laser beam is minimised by dividing the data obtained from detector D_1 to detector D_2.

Samples are placed at the translation stage that can move along the Z-axis of the laser beam with the help of an automated stepper motor. The interfacing between the stepper motor of the translation stage and the computer is established through stepper motor driver. The motion of the stepper motor for data collection is controlled by the Labview program and an oscilloscope is used to visualise the signal from detectors and boxcar integrators.

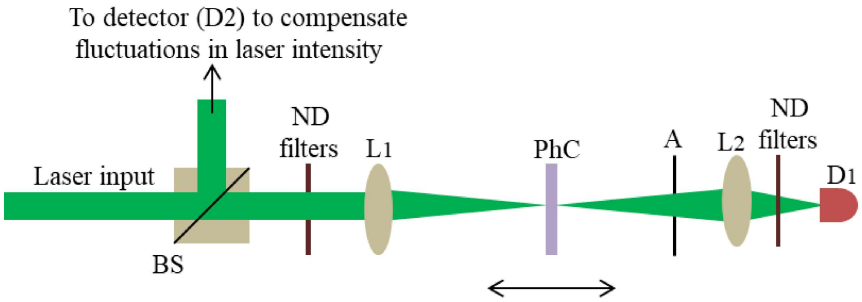

Figure 2.8: *Schematic diagram of open aperture Z-scan experimental setup: BS-Beam splitter, L-Lens, PhC- Photonic crystal, A-Aperture, ND filters- Neutral density filters, D-Detector*

2.6 Numerical analysis of 1-Dimensional photonic crystal

Numerical modelling of 1D PhC is very relevant for their design and accurate fabrication. We numerically simulate the optical field amplitude in each layer of the 1D PhC using optical transfer matrix method (TMM) [36]. TMM is applied to a periodic medium to examine the propagation of electromagnetic waves through each layer. Here each of the group of layers on either side of the defect layer forms a Bragg mirror (BM). Reflection of light at an interface separated by two media is described by Fresnel equations. However, to describe the reflection from the periodic stratified medium TMM is useful. This method is derived from the boundary conditions (continuity) of the electric field across an interface. TMM consists of simple matrix operations in which the field at the final layer of a multilayer can be found if the field at the starting layer is known. Each layer of the 1D PhC can be represented as individual matrices. The product of these individual matrices gives the matrix of the whole system.

We consider a periodic multi-layered structure with refractive indices n_L (SiO_2), n_H (TiO_2) and n_d (BTO) as schematically shown in Figure 2.9, where n_L, n_H and n_d are respectively

corresponding to the low refractive index layer, high refractive index layer and refractive index of the defect layer. The thicknesses of the corresponding layers are d_L, d_H and d_d respectively. A_m denotes the amplitude of the incident wave and B_m is that of the reflected wave. A_m and B_m are not continuous at the interface of the two layers. The outermost layers of the microcavity structure are connected to two homogeneous media designated by n_0 and n_s where n_0 is refractive index of the initial medium and n_s is the refractive index of final medium (substrate). Here A_0 and A_s are respectively represent the amplitudes of the electromagnetic waves at the initial medium and the substrate, in our case air and glass.

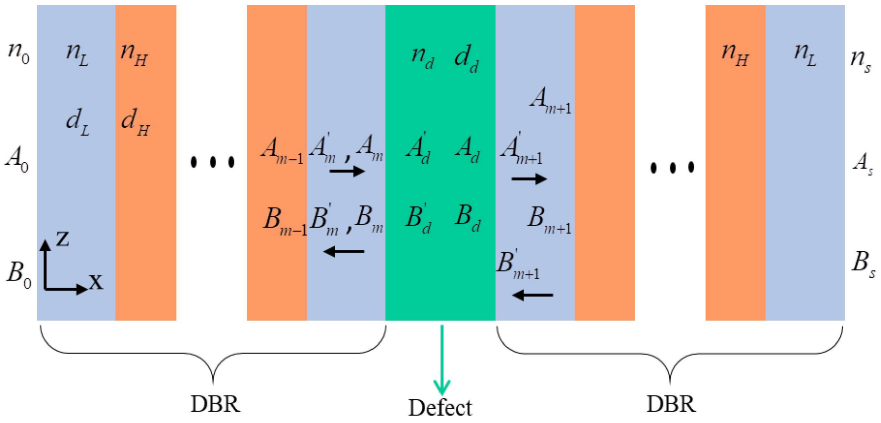

Figure 2.9: *Schematic of 1D PhC microcavity. A defect layer is introduced between two Distributed Bragg Reflector (DBR).*

The field amplitude in each layer is related by a product of 2×2 matrices in sequence. The electric field on both sides of an interface is linked by the corresponding dynamic matrix D, whereas the propagation matrix P connects the electric field inside a bulk layer. The product of the matrices is again a 2×2 matrix, and is expressed in terms of the complex Fresnel reflection and transmission coefficients of the interface. It takes the same form in both cases of s- or p- waves. Repeated application of the transformations for the N layers and N+1 interfaces leads to a product of N+1 matrices as given below.

$$T^{(N)} = \begin{pmatrix} T_{11} & T_{12} \\ T_{21} & T_{22} \end{pmatrix} = D_0^{-1}[\prod_{m=1}^{N} D_m P_m D_m^{-1}] D_{N+1} \quad (2.6)$$

Subsequently, the complex reflection and transmission coefficients of the multilayer can be obtained from the four elements of the transfer matrix, which are respectively given by,

$$r = \frac{T_{21}}{T_{11}} \quad (2.7)$$

$$t = \frac{1}{T_{11}} \quad (2.8)$$

The reflectance and the transmittance of the front surface can be obtained as the square of the above coefficients r and t respectively.

$$\text{Reflectance; } R = |r|^2 = \left|\frac{T_{21}}{T_{11}}\right|^2 \quad (2.9)$$

$$\text{Transmittance; } T = |t|^2 = \left|\frac{1}{T_{11}}\right|^2 \quad (2.10)$$

Figure 2.10 shows the numerically simulated spatial distribution of the transverse electric (TE) field intensity ($|E|^2$) in the 1D PhC microcavity of 23 layers versus wavelength. The dimensions chosen for the simulations of the microcavity are as follows: The input laser field wavelength is 532 nm and the corresponding thicknesses are d_L = 110 nm, d_H = 58 nm and d_d =130 nm. The refractive index values are n_L =1.55, n_H =2.67 and n_d =2.47. A dark region expands from 500 nm to 700 nm represents the photonic band gap of the 1D PhC microcavity and bright discrete line-shaped intensities (area encircled by the green coloured dashes) denotes the resonance mode at 532 nm at an incident angle of 32^0, which is also known as the passband.

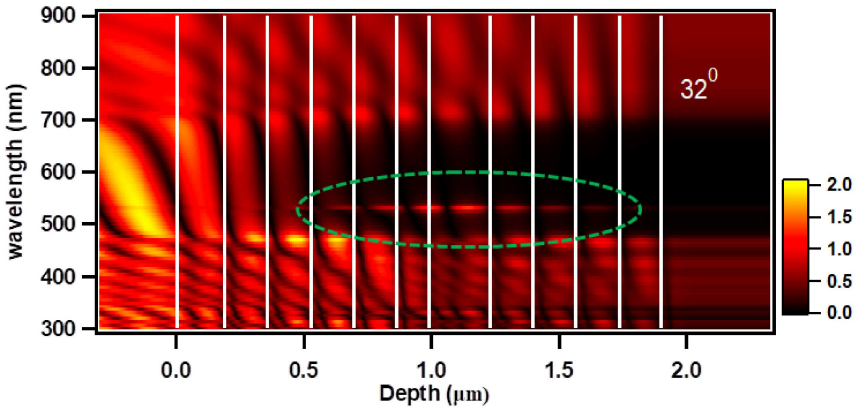

Figure 2.10: *Simulated spatial field distribution of the TE optical field intensity ($|E|^2$)-wavelength mapping in the 1D PhC microcavity.*

2.7 References

[1] E.Yablonovitch, "Inhibited spontaneous emission in solid state physics and Electronics." Phys. Rev.Lett. 58, p2059 (1987).

[2] S. John, "Strong localization of photons in certain disordered dielectric Superlattices." Phys. Rev. Lett. 58, p2486 (1987).

[3] J.D. Joannopoulos, S.G. Johnson, J. N. Winn and R. D. Meade, "Photonic Crystals: molding the flow of light." Princeton University Press, Second edition (2008).

[4] McCrackin, L. Frank, E. Passaglia, R. R. Stromberg and H. L. Steinberg, "Measurement of the thickness and refractive index of very thin films and the optical properties of surfaces by ellipsometry." J. Res. Nat. Bur. Sec. A 67 (1963).

[5] D. Pristinski, V. Kozlovskaya, and S. A. Sukhishvili, "Determination of film thickness and refractive index in one measurement of phase-modulated ellipsometry." J. Opt. Soc. Am. A 23 (10), pp2639-2644 (2006).

[6] J. Kouba et al. “Fabrication of nanoimprint stamps for photonic crystals.” J. Phys. Conf. Ser. 34, p897 (2006).

[7] Y. W. Su, C.S. Wu, C. C. Chen and C. D. Chen, “Fabrication of two- Dimensional arrays of CdSe pillars using e-beam lithography and electrochemical deposition.” J. Adv. Mater. 15 (1), pp49-51 (2003).

[8] G. Subramania and S. Y. Lin, “Fabrication of three-dimensional photonic crystal with alignment based on electron beam lithography.” Appl. Phys. Lett. 85 (21), pp5037-5039 (2004).

[9] M. Bayindir, C. Kural, and E. Ozbay. “Coupled optical microcavities in one-dimensional photonic bandgap structures.” J. Opt.A 3 (6), pS184 (2001).

[10] D. N. Sharp et al., “Photonic crystals for the visible spectrum by holographic lithography.” J. Opt. Quant. Electron. 34 (1-3), pp3-12 (2002).

[11] J. B. Yeo, and H. Y. Lee, “Fabrication of photonic crystals by holographic lithography method.” J. Adv. Mater. Res. 31, pp98-100 (2008).

[12] C.C. Cheng et al. “New fabrication techniques for high quality photonic crystals.” J. Vac. Sci. Technol. B 15 (6), pp2764-2767 (1997).

[13] V. A. Tolmachev et al., “1D photonic crystal fabricated by wet etching of silicon.” J. Opt. Mater. 27 (5), pp831-835 (2005).

[14] F. O’Sullivan et al., “Optical characteristics of one-dimensional Si/SiO_2 photonic crystals for thermophotovoltaic applications.” J. Appl. Phys. 97(3), p033529 (2005).

[15] A. R. Parker, and H. E. Townley. “Biomimetics of photonic nanostructures.” Nat. Nanotechnol. 2 (6), p347 (2007).

[16] J. Bellessa, et al., “Eu 3+-doped microcavities fabricated by sol–gel process.” Appl. Phys. Lett. 79 (14), pp2142-2144 (2001).

[17] K. M. Chen et al., "SiO_2/TiO_2 omnidirectional reflector and microcavity resonator via the sol-gel method." J. Appl. Phys. Lett. 75 (24), pp3805-3807 (1999).

[18] R. M. Almeida and S. Portal, "Photonic band gap structures by sol–gel processing." Current Opinion in Solid State and Materials Science 7 (2), pp151-157 (2003).

[19] F. Scotognella et al., "Metal oxide one dimensional photonic crystals made by RF sputtering and spin coating." J. Ceram. Int. 41 (7), pp8655-8659 (2015).

[20] S. Jena et al., "Omnidirectional photonic band gap in magnetron sputtered TiO_2/SiO_2 one dimensional photonic crystal." Thin Solid Films 599, pp138-144 (2016).

[21] Y. X. Ying et al., "Fabrication and characterization of three-dimensional core–shell structure ZnO photonic crystals by magnetron sputtering based on opal template." J. Cryst. Growth 312 (16-17), pp2484-2488 (2010).

[22] K. M. Chen et al., "SiO_2/TiO_2 omnidirectional reflector and microcavity resonator via the sol-gel method." J. Appl. Phys. Lett. 75 (24), pp3805-3807 (1999).

[23] P. J. Kim et al., "Fabrication of oxide materials for one-dimensional photonic crystals." J. Korean Phys. Soc. 49 (3), p869 (2006).

[24] N. Tsurumachi et al. "Time response of one-dimensional photonic crystals with a defect layer made of semiconductor quantum dots." Jpn. J. Appl. Phys. 38 (12A), pL1400 (1999).

[25] S. Valligatla et al., "Optical field enhanced nonlinear absorption and optical limiting properties of 1-D dielectric photonic crystal with ZnO defect." Opt. Mater. 50, pp229-233 (2015).

[26] M. A Guohong, S. H. Tang, J. Shen, Z. Zhang and Z. Hua, "Defect-mode dependence of two-photon-absorption enhancement in a one-dimensional photonic bandgap structure." Opt. Lett. 29 (15), pp1769-1771 (2004).

[27] K. Vasudevan, M. C. Divyasree and K. Chandrasekharan, “Enhanced nonlinear optical properties of ZnS nanoparticles in 1D polymer photonic crystal cavity.” J. Optlastec. 114, pp35-39 (2019).

[28] J. Bellessa, S. Rabaste, J. C. Plenet, J. Dumas and J. Mugnier, “Eu^{3+}-doped Microcavities fabricated by sol-gel process.” Appl. Phys. Lett. 79 (14), pp2142-2144 (2001).

[29] D. Biallo, A. D. Orazio and V. Petruzzelli, “Enhanced light extraction in Er^{3+} doped SiO_2-TiO_2 microcavity embedded in one dimensional photonic Crystal.” J. Noncrysol. 352 (36-37), pp3823-3828 (2006).

[30] R. M. Almeida and A. C. Marques, “Rare earth-doped photonic crystals via sol-gel.” J. Mater. Sci. 20 (1), pp307-311 (2009).

[31] S. F. Chichibu, T. Ohmori, N.Shibata and T. Koyama, “Dielectric SiO_2/ZrO_2 distributed Bragg reflectors for ZnO microcavities prepared by the reactive helicon-wave-excited-plasma sputtering method.” Appl. Phys. Lett. 88 (16), p161914 (2006).

[32] G. H. Haertling, “Ferroelectric thin films for electronic applications”, J. Vac. Sci. Tech A. 9 (3), pp414-420 (1991).

[33] B. Szyszka et al., “Recent developments in the field of transparent conductive oxide films for spectral selective coatings, electronics and photovoltaics.” Curr. Appl. Phys. 12, ppS2-S-11 (2012).

[34] S. H. Jeong, J. K. Kim, B. S. Kim, S. H. Shim and B. T. Lee, “Characterization of SiO_2 and TiO_2 films prepared using Rf magnetron sputtering and their application to anti-reflection coating.” J. Vacuum 76 (4), pp507-515 (2004).

[35] M. Sheik-Bahae, A. A. Said, T. H. Wei, D. J. Hagan and E. W. Van Stryland, “Sensitive measurement of optical nonlinearities Using a single beam.” IEEE J. Quantum electronics 26 (4), pp760-769 (1990).

[36] P. Yeh, “Optical waves in layered media.” New York: Wiley 95 (1988).

Chapter 3

Fabrication and Characterization of Sol-Gel prepared 1-D Photonic Crystals

1-D photonic crystals composed of SiO_2 - TiO_2 as adjacent layers and SiO_2-SnO_2 as adjacent layers is fabricated using Sol-Gel method. The band gap and morphology of the crystals are charecterized and compared. The dependence of band gap on the number of layers and polarization are studied.

3.1 Introduction

Sol-Gel is the chemical process in which the polycondensation reactions of precursors in a liquid turns in to the formation of an oxide network [1-4]. The typical precursors used in this method are metal alkoxides and metal chlorides [5]. It is a low cost method of fabricating the structure in which the chemically prepared solution is converted into solid film after annealing process. Low cost fabrication and high quality films with a broad variety of materials are the major attractions of this method. The schematic diagram of the typical multilayered structure (1D PhC) is shown in Figure 3.1. The low refractive index layer (n_1) and high refractive index layers (n_2) are represented by green and violet colours respectively and these multilayers are growing on silicon/glass substrate.

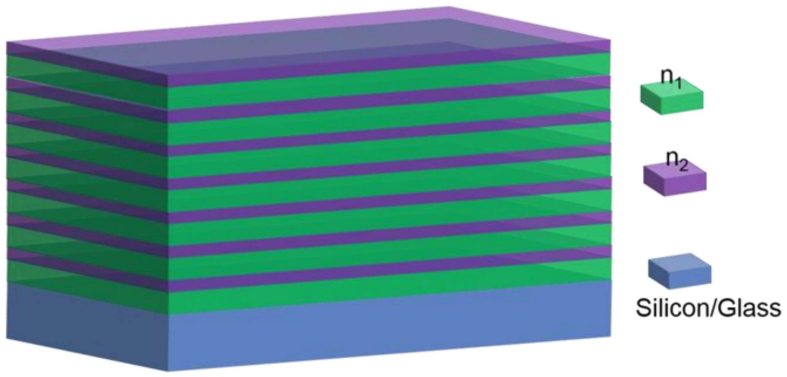

Figure 3.1: *Schematic diagram of 1D PhC:* n_1 *and* n_2 *are low and high refractive indices respectively (It is already discussed in chapter 1)*

3.2 1-D Photonic crystal fabrication by Sol-Gel

The fabrication procedure of photonic crystal by sol-gel method includes 3 different steps, namely the preparation of solution, film deposition and annealing. An overview of the fabrication of thin film using Sol-Gel is showed in Figure 3.2. Here we discuss 1D PhC structure made up of multilayers (14 layers) of SiO_2-TiO_2 and SiO_2-SnO_2. Oxide based dielectric materials are of typical choice since they are transparent over wide range of frequencies, i.e., from ultra violet (UV) to near infra red (IR). These materials also show high resistance to corrosion, radiation and temperature [6]. These structures are deposited on glass/silicon substrate. The different steps involved in the fabrication are discussed below.

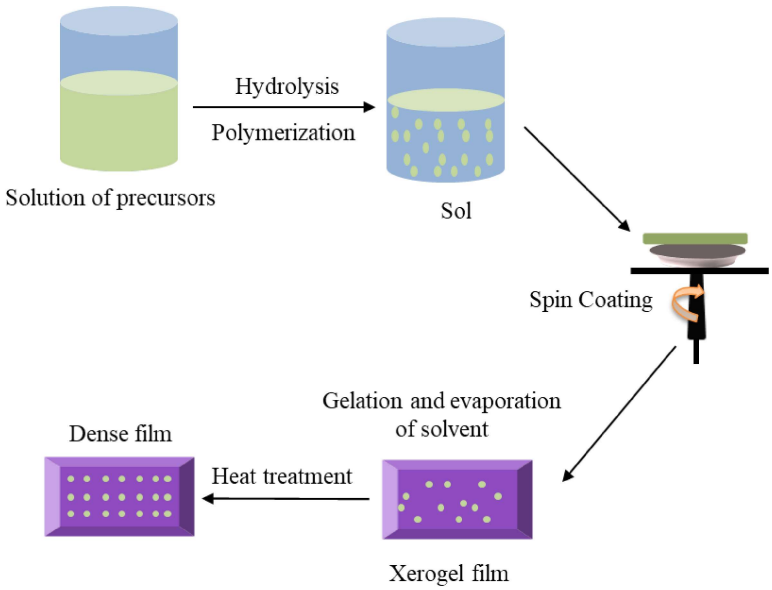

Figure 3.2: *An overview of the fabrication of thin film using Sol-Gel synthesizing.*

3.2.1 Preparation of Sols

Synthesis of Sols such as SiO_2 [7], TiO_2 [8] and SnO_2 [9] is the first step of making thin films and these sols are separately prepared. Tetra-ethyl-ortho silicate (TEOS), ethanol, distilled water and HCl are the precursors required for making SiO_2 mixture. The scheme for the preparation of SiO_2 precursor solution is shown in Figure 3.3(a). After mixing 3 ml TEOS

and 16 ml of ethanol, hydrolyze the solution by adding 4 ml of water and 0.5 ml of HCl. The solution is then magnetically stirred for 12 hours.

Figure 3.3(b) denotes the outline of the procedure for synthesizing titania (TiO_2) precursor solution. Titanium isopropoxide (1.5 ml) is dissolved in anhydrous isopropanol (4.5 ml) and to which 5 ml of acetic acid is added. After stirring the solution at 60 ^{0}C for 30 minutes, 12 ml of methanol is added. The solution is stirred further for 3-4 hours until a transparent solution is obtained.

The tin oxide (SnO_2) solution is prepared by dissolving 0.5 g of stannous chloride dihydrate ($SnCl_2$ $2H_2O$) in 20 ml of ethanol (C_2H_5-OH). Stir the mixture for 3 hours at room temperature.

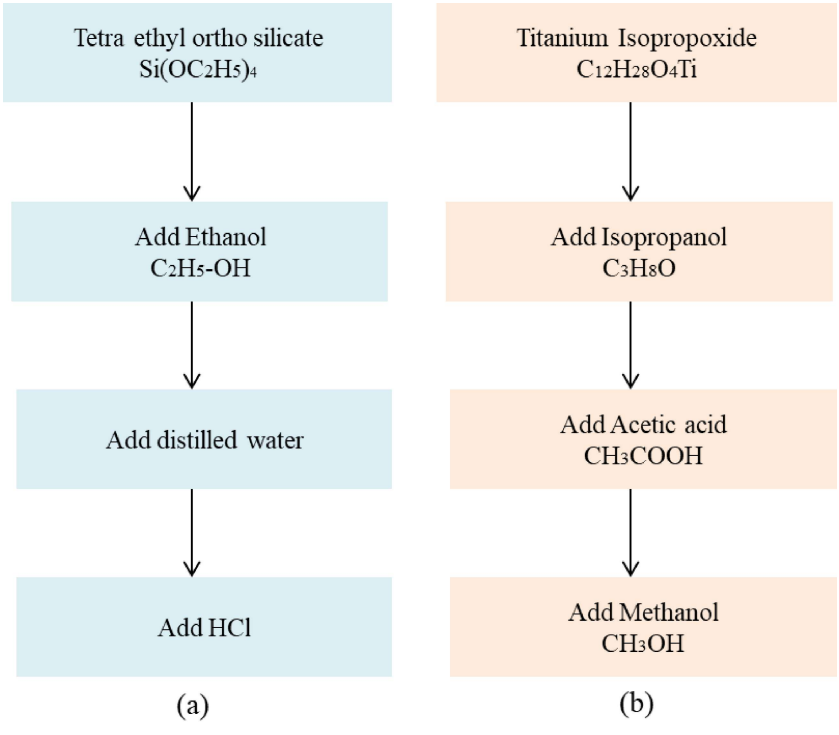

Figure 3.3: *Scheme of preparation of silica (SiO_2) solution (a) and titania (TiO_2) solution (b)*

3.2.2 Fabrication of Photonic Crystal by spin coating

Prior to the fabrication, the substrates should be cleaned thoroughly. It is cleaned with Piranha solutions (mixture of concentrated sulphuric acid (H_2SO_4) and hydrogen peroxide (H_2O_2) in 3:1 ratio) to remove organic impurities from the substrates and then it is cleaned by treating ultrasonically in distilled water. The SiO_2 sol is used to coat the film on already cleaned glass/silicon substrates using spin coater (SPIN 150, Germany). It is operated at 2500 rpm for 2 minutes. Then it is dried at room temperature and heated slowly between 100 ^{0}C and 200 ^{0}C for 3 minutes at the rate of 1 ^{0}C/s using a programmable furnace (YUDIAN Al-508, China) and after the heat treatment it keeps at outside for cooling about 7-10 minutes. The TiO_2 sol is used to coat the next layer in which the spin coater is operated at 3500 rpm for 2 minutes. Here the heat treatment is done between 200 ^{0}C and 300 ^{0}C for 3 minutes at the rate of 1 ^{0}C/s and kept outside for 7-10 minutes for cooling. This process is repeated until 14 layers (7 bilayers of SiO_2/TiO_2 (BM1)) is obtained. Similarly 7 bilayers of SiO_2/SnO_2 (BM2) is prepared in which SnO_2 film is coated by operating the spin coater at a speed of 3000 rpm and following the same heat treatment of SiO_2. The multilayer film growth is done inside the locally made glove box in argon (Ar) atmosphere and the whole experimental unit is shown in Figure 3.4. The fabricated structure is then characterized by reflection/transmission spectroscopy and FESEM.

Figure 3.4: *The experimental unit of fabrication of photonic crystal by Sol-Gel method. The spin coater and furnace is shown in the inset at right top corner.*

3.3 Optical Characterization of the Samples

3.3.1 Morphology

The cross-sectional morphology of the 1D PhC is recorded by FESEM and the experimental details are explained in Section 2.4.2. The cross-sectional image of the SiO_2-SnO_2 (7 bilayers) 1D PhC and SiO_2-TiO_2 (7 bilayers) 1D PhC is shown in Figure 3.5(a) and (b) respectively.

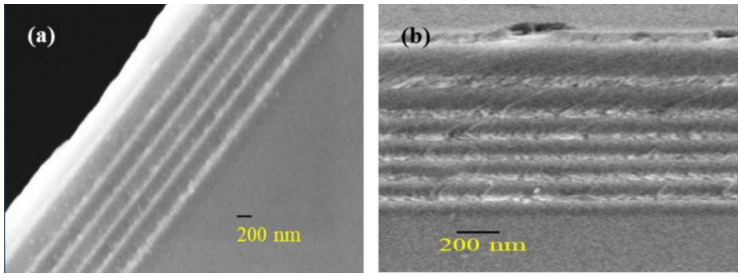

Figure 3.5: *(a) FESEM image of SiO_2-SnO_2 PhC (BM2). The alternate dark and bright lines are SiO_2 and SnO_2 respectively. (b) FESEM image of SiO_2-TiO_2 PhC (BM1), the alternate dark and bright lines are SiO_2 and TiO_2 respectively.*

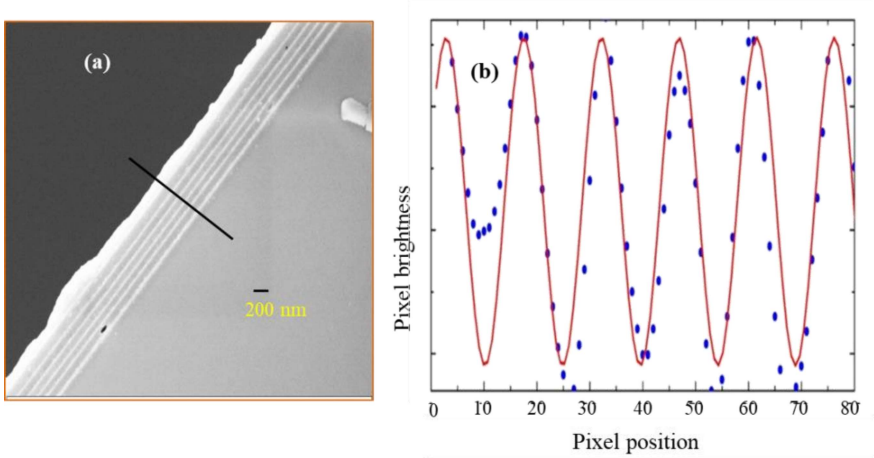

Figure 3.6: *(a) Perpendicular line drawn to measure the intensity contrast in FESEM image of SiO_2-SnO_2 PhC (BM2). (b) The experimental data (blue dots) are fitted by sine fit (red sinusoidal wave).*

The FESEM micrographs display the homogeneity in film thickness and periodicity. The periodicity in the thickness of the layers can be estimated using pixel intensity contrast fitting. From the pixel contrast of perpendicular line drawn in the FESEM image of SiO_2-SnO_2 PhC, the periodicity is found to be 94 nm (Figure 3.6).

3.3.2 Reflection Spectrum

The reflection spectrum (Section 2.4.1) of BM1 and BM2, recorded using UV-Visible-Near IR Spectrophotometer, is shown in Figure 3.7. The band gap of BM1 ranges from 579 nm to 729 nm and that of BM2 ranges from 469 nm to 566 nm. That is BM1 has a stop band of 150 nm and that of BM2 has 97 nm. The large band gap of BM1 is due to the high contrast in refractive index between the adjacent layers.

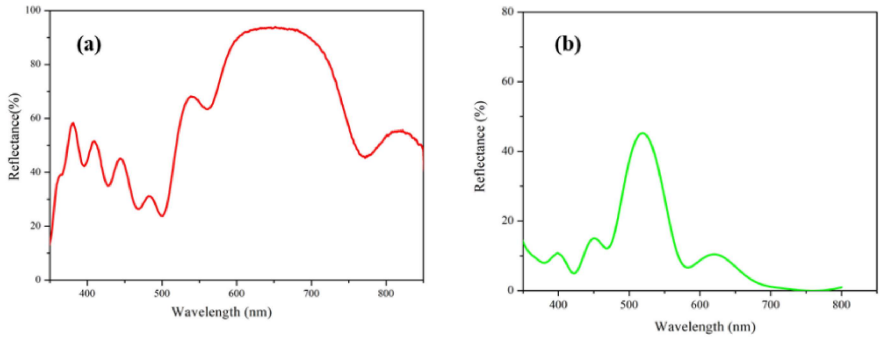

Figure 3.7: *(a) The reflection spectrum of BM1. (b) The reflection spectrum of BM2.*

The angle tuned reflection spectrum of BM1 and BM2 are shown in Figure 3.8. The oscillations on both sides of the stop band shows the *Fabry-Perot* fringes. Both Bragg mirrors show significant blue shift for the higher angle of incidence. The blue shift in the spectra with higher angle of incidence can be explained with the shortening of lattice constant experienced by the incident optical wave with the increase of the incident angle, given by the relation [10,11],

$$\lambda(\theta) = \lambda(0) \times (1 - Sin^2(\theta) / n_{eff}^2)^{1/2} \qquad (3.1)$$

Where $\lambda(0)$ and $\lambda(\theta)$ are wavelengths corresponding to the cavity peaks of 0^0 and θ^0 angle of incidence with respect to the normal to the surface, n_{eff} is the effective refractive index.

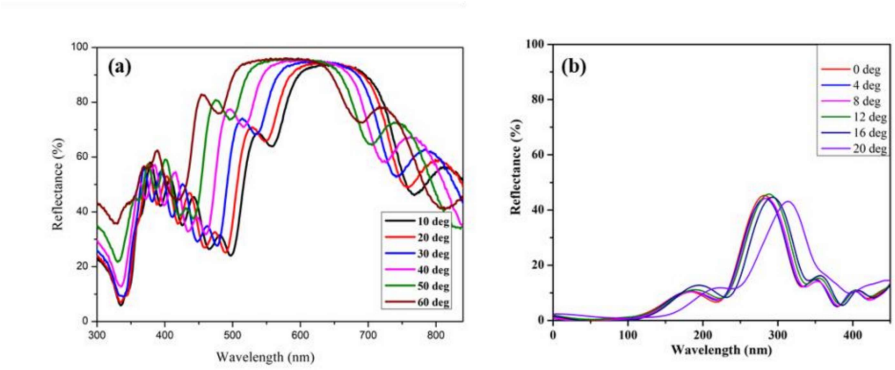

Figure 3.8: *(a) Angle variable reflection spectra of BM1. (b) Angle variable reflection spectra of BM2.*

The peak reflectivity at a specific wavelength can be expressed as [12].

$$R = \left[\frac{1-(n_H/n_L)^{2q}(n_H^2/n_S)}{1+(n_H/n_L)^{2q}(n_H^2/n_S)}\right]^2 \qquad (3.2)$$

Where, n_H and n_L are high and low refractive indices of alternate layers of materials respectively. The refractive index of the substrate is designated as n_S and q is the total number of layer periods. The reflectivity of BM1 and BM2 is calculated as 99.34 % and 95.43 % respectively.

3.4 Consequences of number of layers on photonic band gap of 1D PhC

Width of the band gap of photonic crystal depends on the number of layers. Figure 3.9 shows the reflection spectrum of SiO_2-TiO_2 photonic crystal at normal incidence which comprises 7

bilayers, 5 bilayers and 4 bilayers respectively. While 14 layered 1-D PhC shows the highest reflection, the perfect reflectance can be observed for the PhC having number of layers greater than 20 [13]. The stop band edge is much sharper for the higher number of layers and the group velocity v_g of photon will be nearly equal to zero at this band edge. The 1D PhC with 14 layers have much steeper band edge than 10 and 8 layered. The *Fabry-Perot* fringes on both sides of the stop band are higher for the 14 layer 1D PhC compared to other fabricated 1D PhC's. The increase in the number of fringes can be attributed to the reflections from the interfaces of the dielectric stack of layers. As the number of layers become higher, more and more reflections can be observed which give rise to the higher number of *Fabry-Perot* fringes. The width of the band (FWHM) is higher for lesser number of layers.

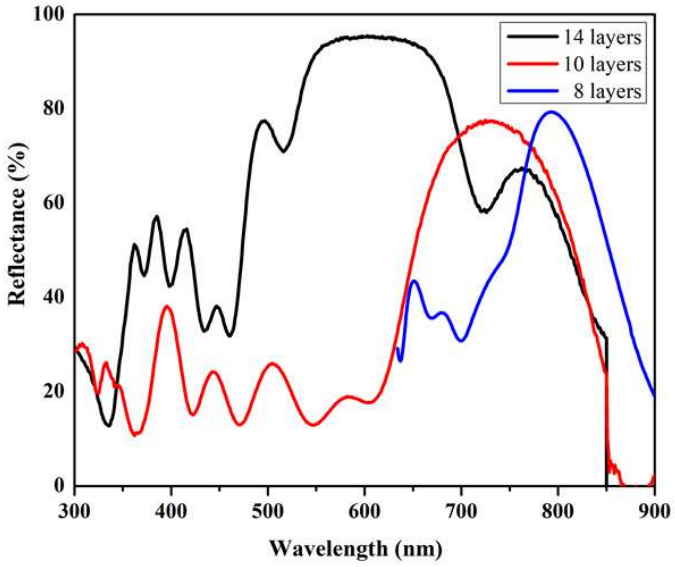

Figure 3.9: *The reflection spectra of three SiO_2-TiO_2 photonic crystals having 14, 10 and 8 layers*.

3.5 Dependence of photonic band gap on Polarization

The polarization dependent spectral characteristics of the 1D PhC of SiO_2-TiO_2 (BM1) for s- and p- polarized light are shown in Figure 3.10. The reflection is recorded at 45° to the crystal normal. The reflectance is higher for p-polarized light, but the FWHM is reduced with respect to s- polarized light.

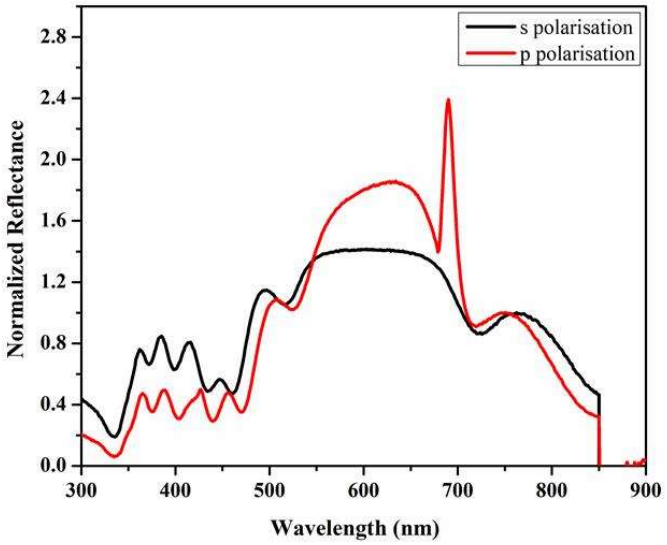

Figure 3.10: *The reflection spectra of 1-D PhC (BM1) for s- and p- polarized light at an angle 45°.*

3.6 Challenges in the fabrication of Photonic crystal by Sol-Gel method

The Sol-Gel fabrication method is a low cost wet chemical method that is used in micro and macro photonic applications. It has wide variety of applications in the thin film industry such as antireflection coatings [14], waveguides [15], Filters [16] etc. One of the major advantages of this method is the compositional flexibility in oxides, piezoelectrics and ferroelectrics etc. Apart from these the sol-gel fabrication of PhC faces a lot of challenges. The grave limitation of this technique is cracking which takes place as it undergoes multiple annealing steps. As a result of the chemical reactions between the ingredients within the solution, many atoms,

molecules and ions are generated, which decline the optical property of the materials. We were not able to succeed in fabricating perfect microcavity structures due to the cracking issues. The different thermal expansion coefficient for different materials leads to cracks in the photonic crystal structure. The humidity in the atmosphere too plays an important role in developing the cracks.

3.7 Conclusion

The preliminary investigations on 1-D photonic crystals with adjacent layers as SiO_2-TiO_2 and SiO_2-SnO_2 using Sol-Gel method are reported. The reflection spectrum of both samples show that the band gap is in the visible region. The FESEM image shows the homogeneity in the layer thickness and the periodicity in the thickness of the layers is calculated using fitting. The effect of stop band on the number of layers and refractive index contrast between the adjacent materials is studied. The dependence of the spectral characteristics of band gap on polarisation is also studied which shows that the FWHM of the stop band becomes shorter for TM polarisation, but the reflectivity will be higher compared to TE polarisation.

3.8 References

[1] J. W. Galusha, L. R. Richey, M. R. Jorgensen, J. S. Gardner and M. H. Bartl, "Study of natural photonic crystals in beetle scales and their conversion into inorganic structures via a sol–gel bio-templating route." J. Mater. Chem. 20(7), pp1277-1284 (2010).

[2] R. M. Almeida and S. Portal, (2003). Photonic band gap structures by sol–gel processing." Curr. Opin. Solid. St. M 7(2), pp151-157 (2003).

[3] K. M. Chen, A. W. Sparks, H. C. Luan, D. R. Lim, K. Wada and L. C. Kimerling, "SiO 2/TiO2 omnidirectional reflector and microcavity resonator via the sol-gel method." Appl. Phys. Lett. 75(24), pp3805-3807 (1999).

[4] R. M. Almeida, M. C. Gonçalves and S. Portal, "Sol–gel photonic bandgap materials and structures." J. Non-Cryst. Solids 345,pp 562-569 (2004).

[5] M. Kuwabara, "Photonic Crystals Fabricated by Sol-Gel Process: Handbook of Sol-Gel Science and Technology: Processing, Characterization and Applications." pp2127-2160 (2018).

[6] L. D. Bonifacio, B. V. Lotsch, D. P. Puzzo, F. Scotognella and G. A. Ozin, "Stacking the nanochemistry deck: structural and compositional diversity in one-dimensional photonic crystals." Adv. Mater. 21(16), pp1641-1646 (2009).

[7] B. D. Fabes, D. P. Birnie III and B. J. J. Zelinski, "Porosity and composition effects in sol-gel derived interference filters." Thin Solid Films 254(1-2), pp175-180 (1995).

[8] U. Selvaraj, A. V. Prasadarao, S. Komarneni and R. Roy, "Sol–gel fabrication of epitaxial and oriented TiO_2 thin films." J. Am. Ceram. Soc. 75(5), 1167-1170 (1992).

[9] S. F. Ahmed, S. Khan, P. K. Ghosh, M. K. Mitra and K. K. Chattopadhyay, "Effect of Al doping on the conductivity type inversion and electro-optical properties of SnO_2 thin films synthesized by sol-gel technique." J. Sol-Gel Sci. Technol. 39(3), pp241-247 (2006).

[10] Q. Gong and X. Hu, "Photonic crystals: principles and applications." Jenny Stanford Publishing, (2014).

[11] S. Guddala, V. K. Dwivedi, G. Vijaya Prakash and D. Narayana Rao, "Raman scattering enhancement in photon-plasmon resonance mediated metal-dielectric microcavity."J. Appl. Phys. 114(22), p224309 (2013).

[12] R. Katouf, T. Komikado, M. Itoh, T. Yatagai and S. Umegaki, "Ultra-fast optical switches using 1D polymeric photonic crystals." Photonics Nanostructures: Fundam. Appl. 3(2-3), pp116-119 (2005).

[13] S. Valligatla, A. Chiasera, S. Varas, N. Bazzanella, D. N. Rao, G. C. Righini and M. Ferrari, M, “High quality factor 1-D Er 3+-activated dielectric microcavity fabricated by RF-sputtering.” Opt. Express 20(19), pp21214-21222 (2012).

[14] D. Chen, “Anti-reflection (AR) coatings made by sol–gel processes: a review.” Sol. Energy Mater. Sol. Cells. 68(3-4), pp313-336 (2001).

[15] M. Yoshida and P. N. Prasad, “Fabrication of channel waveguides from sol-gel-processed polyvinylpyrrolidone/SiO_2 composite materials.”Appl. Opt. 35(9), pp1500-1506 (1996).

[16] D. S. Hinczewski, M. Hinczewski, F. Z. Tepehan and G. G. Tepehan, “Optical filters from SiO_2 and TiO_2 multi-layers using sol–gel spin coating method.” Sol. Energy Mater. Sol. Cells 87(1-4), pp181-196 (2005).

Chapter 4

Optical Properties of $BaTiO_3$ in Symmetric Microcavity

This chapter deals with the enhancement of nonlinear optical absorption and photoluminescence of one dimensional photonic crystal with $BaTiO_3$ as defect, fabricated via RF sputtering technique. The homogeneity of layers thickness is confirmed through field emission scanning electron microscopy (FESEM). The cavity resonance mode is obatined at 532 nm and the quality factor of the microcaviy is found to be 48. Open aperture Z-scan and spectrometer measurement of microcavity show enhancements in nonlinear absorption and photoluminscence of $BaTiO_3$ at 532 nm and 355 nm, respectively due to the strong field confinement around the defect layer. The experiments show good agreement with numerically simulated results using optical transfer matrix method.

4.1 Introduction

Microcavities become an integral part of photonic devices and technologies due to their ability to confine the photons and lasing applications at micron scale [1]. A photonic microcavity consists of a defect layer between two identical micro-Bragg mirrors, which are multilayers of high contrast refractive index dielectric materials, each layer having a quarter-wave thickness at a given wavelength [2,3]. Here the fabrication procedure strictly follows the perfect Bragg's condition. In this thesis work we call such a cavity as symmetric microcavity. The photon localization in the defect layer due to resonance leads to a large enhancement in linear and non-linear optical properties such as enhanced photoluminescence and non-linear absorption [4,5], which are being explored in this chapter. Geon Joon Lee *et al.* were the first to study the linear and nonlinear optical enhancement in 1D PhC using ZnO as the defects [4]. Later, Tsurumachi and *et al.* demonstrated that the nonlinear optical properties of one dimensional photonic crystal (1D PhC) can be greatly enhanced by localizing the electromagnetic field within a defect introduced in the 1D PhC [6] and thereafter, enormous number of works have been reported [7-9]. Enhancement in photoluminescence emission from Silica doped with Er^{3+} which emits at the telecommunication wavelength [5] and co-doped with Er^{3+}/Yb^{3+} [10], and non-linear refractive index of CdSe Nano-crystals [11], rare earth ions [12] and quantum dots [1] are few examples in this long list. Enhancement of nonlinear optical properties is crucial for applications as optical switches [13], optical limiting devices [14] and quantum cryptography [15], etc.

In this chapter we demonstrate the cavity enhancement in nonlinear absorption and photoluminescence of BTO in a 1D PhC. The BTO is placed between the two Bragg mirrors of the 1D PhC composed of 11 layers of high and low refractive indices of TiO_2 and SiO_2 respectively. Photoluminescence of BTO is measured using spectrophotometer, while the enhancement in nonlinear absorption coefficient is verified from the open aperture Z-scan

measurements using nanosecond (ns) laser. Our experimental results show good agreement with the simulated optical properties of the 1D PhC using optical transfer matrix formalism.

4.2 Experimental details

The refractive index of the single layer of SiO_2, TiO_2 and BTO are measured using white light ellipsometer (J.A. Woollam, M2000V) and are calculated as 1.48, 2.42 and 2.05 respectively. The experimental details of the Ellipsometer is discussed in section 2.2 and this information of refractive index is crucial towards the design and fabrication of the 1D PhC using the SiO_2 and TiO_2 nano layers with quarter-wave ($\lambda/4$) thickness of 90 nm and 55 nm respectively. The defect layer BTO's half-wave ($\lambda/2$) thickness is 130 nm at the operation wavelength of λ=532 nm. The 1D PhC is shown in Figure 4.1, which is fabricated on a silica/silicon substrate using a multi target sputtering system (Advanced Process Technology, India). The experimental details are discussed in section 2.3.2. First, a high vacuum is attained inside a chamber with a residual pressure of 4.9×10^{-6} mbar and later the chamber is filled with Ar gas up to the pressure of 5.5 $\times10^{-3}$ mbar. Then the first Bragg mirror (11 alternate layers) is deposited on the substrate by sputtering the SiO_2 and TiO_2 targets (50 mm diameter and 3 mm thickness) respectively with RF power of 150 W and 130 W, for a duration of 23 and 17 minutes respectively. Next, the pressure was increased to 7.5 $\times10^{-3}$ mbar and then we deposited the BTO at RF power of 50 W for 82 minutes. Then the second Bragg mirror is deposited on top of the BTO layer as mentioned previously, reducing the pressure back to the initial value.

The cross-sectional morphology and reflection spectrum of the 1D PhC are studied using FESEM (Zeiss, Ultra^{TM}55) and a UV-visible spectrophotometer (Jasco V-670 Spectrophotometer) respectively. The enhancement in nonlinear optical absorption is studied using Z-scan technique [16] with 532 nm nanosecond laser pulses (pulse width 6 ns, repetition

rate of 10 Hz) coming out of an Nd:YAG laser (Spectra-Physics), and the photoluminescence is recorded using photoluminescence spectrophotometer (Fluorolog, Horiba Jobin Yvon).

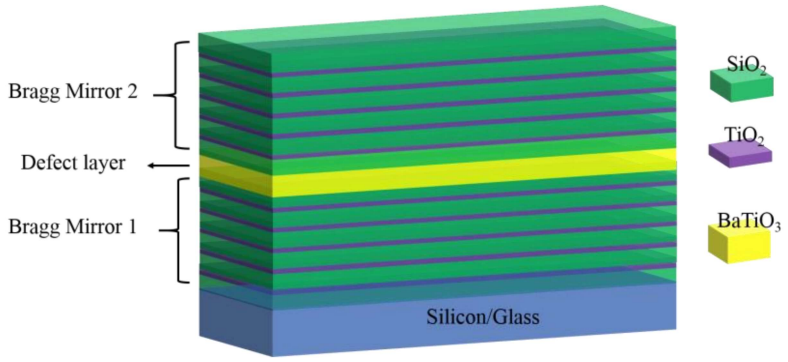

Figure 4.1: *Schematic representation of 1D PhC consists of two Bragg mirrors on either sides of the defect layer.*

4.3 Numerical simulations

Prior to the experiment, we have numerically simulated the electric field distribution and field confinement inside the microcavity using transfer matrix method formalism (TMM). The detailed theory of TMM formalism is discussed in section 2.6. The spectrally resolved optical field (TE) intensity ($|E|^2$) spatial distribution along the length of the cavity through the 1D PhC at an angle 32° is shown in Figure 4.2(a). A dark region expands from 500 nm to 700 nm represents the photonic band gap of the 1D PhC, and bright discrete line-shaped intensities (white-coloured dashed encircled area) correspond to the resonance mode at 532 nm. Figure 4.2(b) shows the angle resolved intensity distribution for the wavelength 532 nm. The maximum light confinement in the BTO layer is observed at an angle of 32° (white-coloured dashed encircled area). Simulated spatial TE and TM field intensity distribution is overlapped with refractive

index profile of the 1D PhC at 32° is shown in Figure 4.2(c). The intensity maxima at the central defect layer imply the strong localization of optical fields in the microcavity. These results reinforce the use of BTO defect containing 1D PhC to strengthen optical effects, which will be discussed in the following sections.

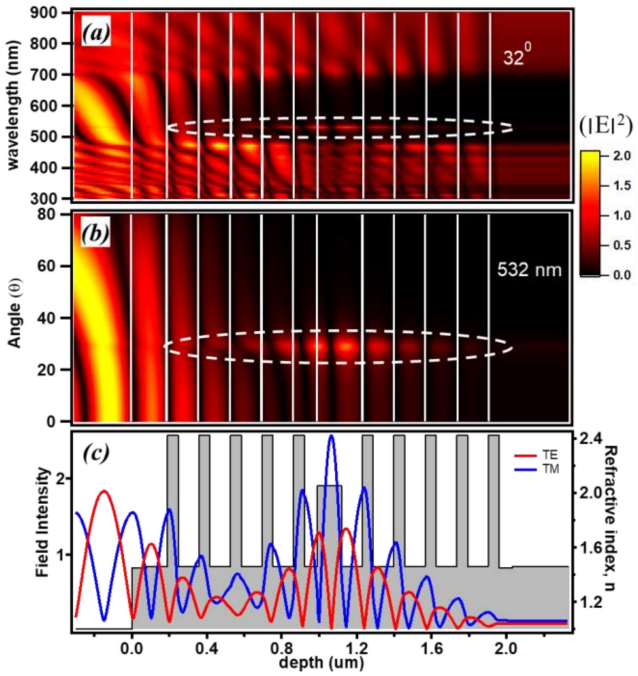

Figure 4.2: *Simulated spatial distribution mapping of the Transverse Electric (TE) Field intensity ($|E|^2$) in the 1D PhC versus (a) wavelength and (b) incident angle. (c) Simulated spatial distribution of the TE and TM Field intensity ($|E|^2$) inside the 1D PhC and the refractive indices profile of 1D PhC at 32° angle and 532 nm.*

4.4 Results and Discussions

The cross-sectional FESEM image of the 1D PhC is given in Figure 4.3(a), where the dark and bright regions represent SiO_2 and TiO_2 layers, while the central thick bright layer corresponds to the BTO defect layer. The layer thicknesses of SiO_2, TiO_2 and BTO are estimated respectively to be 93±5 nm, 53±5 nm and 133±5 nm respectively, which indicates the precision in fabrication. The thickness of the entire 1D PhC structure is 1.8 μm. Figure 4.3(b) shows the reflection spectra of the 1D PhC for an incident angle of 32°, where the solid red and black curves respectively denote the experimental and simulation data. A strong cavity mode is observed at 532 nm with full width at half maximum (FWHM) of 11 nm and its Q-factor is calculated as 48.

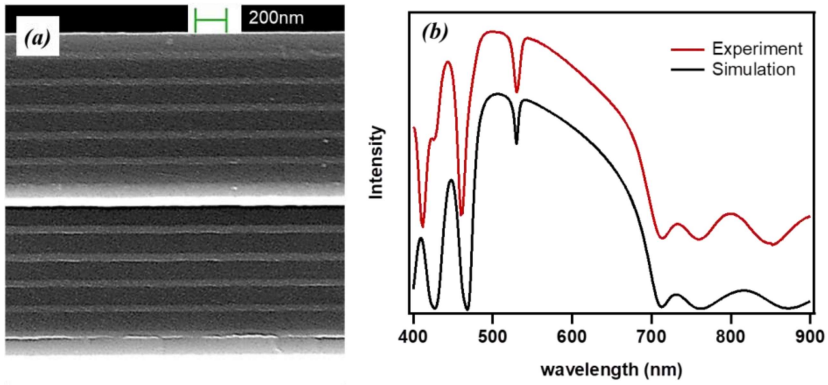

Figure 4.3: (a) *FESEM Image and (b) reflection spectra of the 1-D PhC at an incident angle of* 32^0 *where red and black curves represent the experimental and TMM simulated data respectively.*

The angle tuned experimental and simulated reflection spectra (from 10° to 60°) are given in Figure 4.4(a) and 4.4(b), respectively. The blue shift in the spectra with higher angle of incidence can be understood from the shortening of lattice constant experienced by the incident electromagnetic wave with the increase of the incident angle, given by the relation [17,18],

$$\lambda(\theta) = \lambda(0) \times (1 - \sin^2\theta / n_{eff}^2)^{1/2} \qquad (4.1)$$

where $\lambda(0)$ and $\lambda(\theta)$ are wavelengths corresponding to the cavity peaks of 0^0 and θ^0 angle of incidence with respect to the normal to the surface, n_{eff} is the effective refractive index.

The cavity resonance modes are at 557 nm and 480 nm correspond to 10° and 60° respectively, which indicates the wide tunability of the 1D PhC. These simulations are in well concordance with the experimentally observed results as can be seen from the figure 4.4.

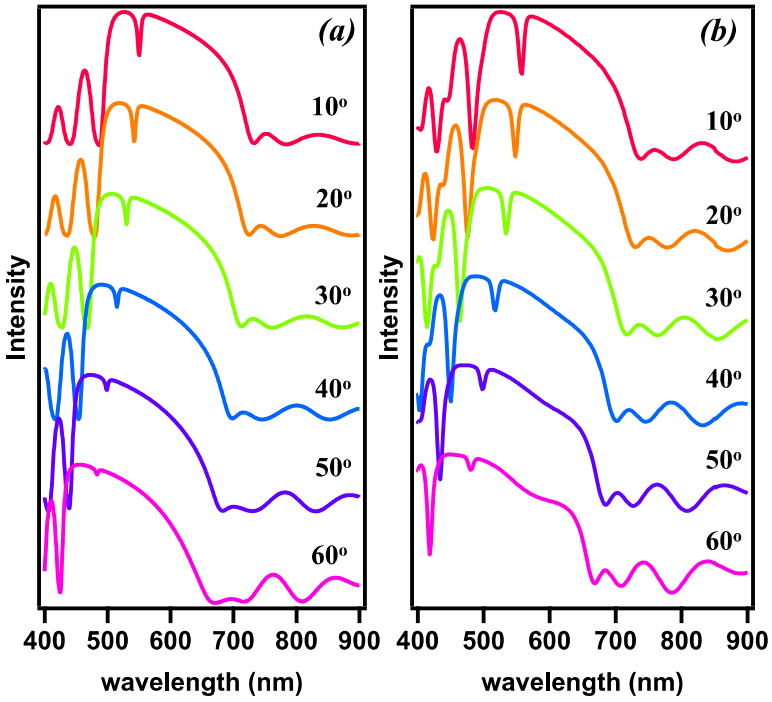

Figure 4.4: *Angle tuned (a) Experimental and (b) TMM simulated reflection spectra of the 1D PhC. (Spectra are shifted along y-axis for clarity)*

Parameters	Simulation (nm)	Experiment (nm)
	Thickness of the layers	
SiO_2	110	93±5
TiO_2	58	53±5
$BaTiO_3$	130	133±5
	Band gap at 32°	
Central Wavelength	532	532
FWHM (nm)	204	205
	Pass band at 32°	
Central Wavelength	532	532
FWHM (nm)	8	11
Q-factor	67	48

Table 4.1: *A table of fabricated and simulated 1D PhC parameters.*

4.4.1 Nonlinear Absorption Studies

The Nonlinear absorption studies are carried out using Z- scan set up, the experimental details of which are discussed in section 2.5.2. Z-scan technique in open aperture (OA) mode [16] is operated to measure the nonlinear absorption of BTO in the microcavity for different incident angles (from 0° to 60°). A frequency doubled Nd:YAG pulsed laser at the wavelength 532 nm (with a pulse width of 6 ns and repetition rate of 10 Hz) is focused on the sample using a plano-convex lens having focal length 120 mm and collecting the output intensity with a photodiode. The experiment is carried out at the input laser intensity of about 0.18 GW/cm^2. The coefficient

of saturable absorption (α) is obtained by fitting the data collected from the above experiment to the normalized transmittance equation [19],

$$T = 1 - \frac{\alpha I_0 L_{eff}}{2^{3/2}\left(1 + \left(z/z_0\right)^2\right)} \tag{4.2}$$

where $\alpha(I) = \alpha_0 / (1 + (I_z / I_s))$, with α_0 the linear absorption coefficient, I_z and I_s the laser radiation intensity at z and saturation intensity respectively. Laser radiation intensity is given by $I_z = I_0/(1+(z/z_0)^2)$, where I_0 is the peak intensity at the centre of the focus, z is the sample position, $z_0 = \pi\omega_0^2 / \lambda$ is the Rayleigh range, ω_0 is the beam waist at the focal point ($z = 0$) and λ is the laser wavelength. The effective path length in a sample of length L is given by the expression

$$L_{eff} = (1 - exp(-\alpha_0 L))/\alpha_0 \tag{4.3}$$

The normalized OA Z-scan curves and related experimental data points are shown in black solid line and dots, respectively in Figure 4.5 (a), where the red line and dots are corresponding to the bare layer of the BTO whose non-linear behaviour is very nearly zero. This clearly indicates the cavity enhancement of the BTO layer due to the localization of photons in the microcavity. The enhancement in nonlinear absorption due to the localization of optical field can be quantified by an enhancement factor G, which is defined as [4]

$$G = \frac{1}{d_{defect}} \int_0^d \frac{\left|E_{defect}(z)\right|^2}{\left|E_{incident}\right|^2}\, dz \tag{4.4}$$

where d_{defect} is the thickness of defect layer, $E_{defect}(z)$ is the amplitude of field in the defect layer as a function of position z, and $E_{incident}$ is the amplitude of the incident field.

The transmittance T at the transmission peak of the defect mode is given as [6]

$$T = \frac{4}{\left[2 + \frac{\pi k}{n_x}\left(\frac{n_B}{n_A}\right)^{2N}\right]^2} \tag{4.5}$$

Where n_A, n_B and n_x are the refractive indices of SiO_2, TiO_2 and defect layer (BTO) and k is the extinction coefficient of the defect layer (BTO) and N is the number of periods of the SiO_2 and TiO_2 on each side of the defect BTO.

The enhancement factor of the cavity is given as [2]

$$G = \frac{T}{2}\left(\frac{n_B}{n_A}\right)^{2N} \tag{4.6}$$

By applying the spatial distribution of the optical field, the enhancement factor G is obtained as 16. Z-scan curves of 1D PhC for the incident angles 0°, 20° and 32° are shown in Figure 4.5(b). The perfect fit of the curve given in Equation (4.2) with the experimentally obtained data gives a nonlinear absorption coefficient α of -1.3×10^{-4} cm/W, -1.22×10^{-4} cm/W and -1.45×10^{-4} cm/W for incident angles 0°, 20° and 32° respectively. The maximum absorption is obtained at an incident angle of 32° as expected and it is due to the presence of strong cavity mode at 532 nm at this particular angle as discussed above. The maximum light confinement in the BTO layer is observed at this angle.

The optically induced changes in these 1D PhC can be utilized in many nonlinear optical applications. For example, the potential usage of BTO thin films for holographic data usage is widely known [20]. Holographic grating is a photo-refractive effect which results from the third-order nonlinear intensity dependent process. These results show optical field enhancement in the

BTO defect-based cavity, leading to optical nonlinearity. The BTO defect layer can be tailored to larger thicknesses (> λ/2) to support higher TE modes, to enable holographic grating recording even at longer wavelengths of visible region, and still support the field enhancement due to the cavity effect [21,22].

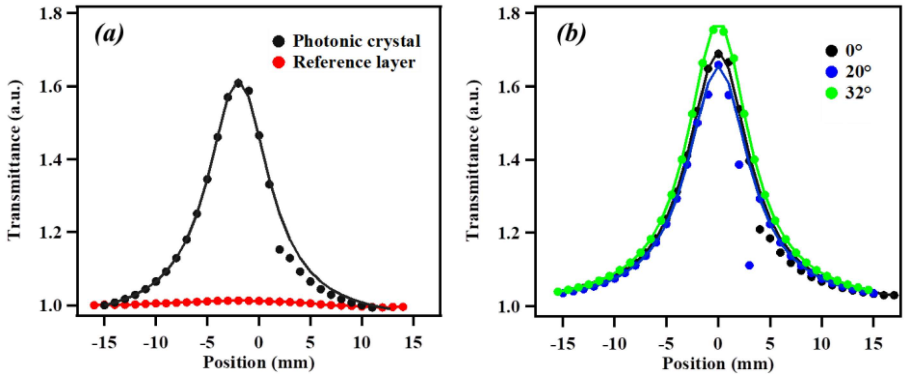

Figure 4.5: *(a) Z scan curves showing corresponding to the BTO reference (red) and 1D PhC with BTO defect (black), and (b) Z scan curves corresponding to 1-D PhC for the incident angles 0^0, 20^0 and 32^o.*

4.4.2 Photoluminescence Emission

The photoluminescence emission of the sample is recorded using photoluminescence spectrophotometer (Fluorolog, Horiba Jobin Yvon), which is explained in section 2.4.3. The absorption spectrum of the reference BTO film is shown in Figure 4.6 (black line), where the observed peaks at 296 nm and 355 nm are corresponding to the interband transitions.

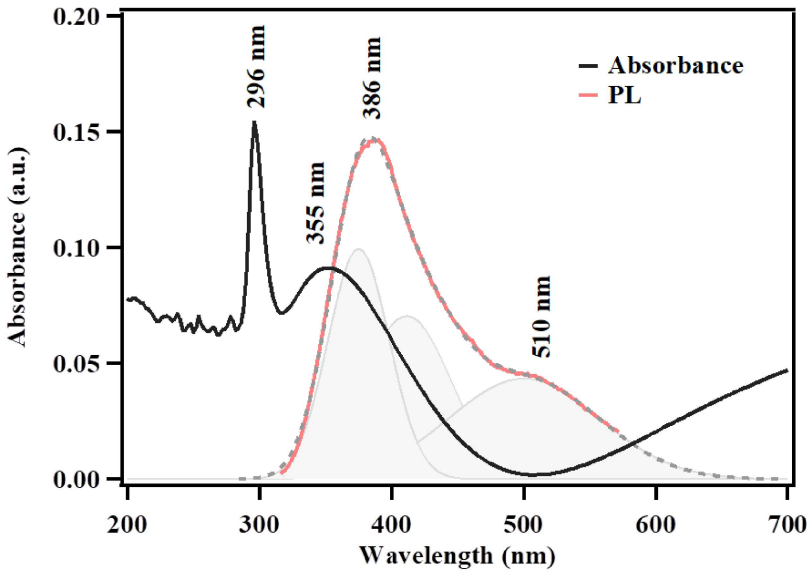

Figure 4.6: *Absorption spectrum (in black) and the photoluminescence emission spectrum (in red) (λ_{ex}=296 nm) of BTO reference layer. Dotted line and shaded curves show the PL multi-Gaussian fits.*

The Photoluminescence (PL) emission spectrum of the reference layer BTO is recorded at excitation wavelengths 296 nm as well as at 355 nm. The PL spectrum excited at 296 nm is shown in Figure 4.6 which shows two prominent peaks at 386 nm and 510 nm and a shoulder at around 425 nm. The multi-Gaussian fitting is depicted with dashed line in Figure 4.6. Figure 4.7(a) shows the PL emission spectra of the BTO single layer (133 nm) and 1D PhC with excitation at 355 nm and the emission peak of both is observed at 424 nm.

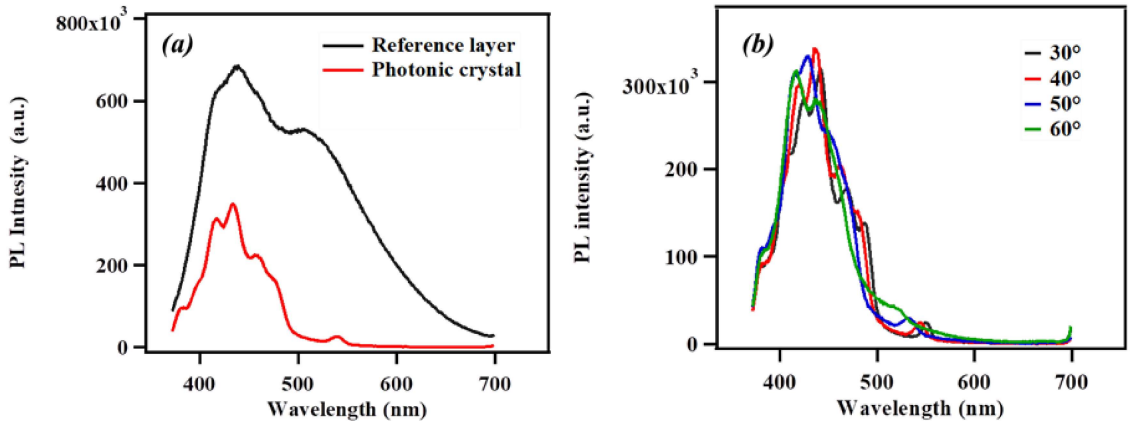

Figure 4.7: *(a) The photoluminescence spectra of single BTO layer (reference layer) and 1D PhC. (b) Angle variable PL spectra of 1D PhC. (λ_{ex}=355 nm)*

The full width at half maximum (FWHM) of the reference layer and 1D PhC are obtained as 167 nm and 69 nm respectively. The cavity effect reduces FWHM of the spectrum of 1D PhC when compared to that of its reference layer. The Q-factor of the microcavity is found to have a value 6, which is estimated from the PL emission spectrum at the resonance wavelength.

The angle tuned PL emission spectra of the 1D PhC from 30° to 60° with step size 10° are given in Figure 4.7(b). The un-shifted PL emission peak is obtained. The PL emission can occur in different ways, through numerous states inside the forbidden energy band gap. PL is directly associated with the localized states existing inside the band gap. The conduction band of BTO consists of s state of Barium and *s* and *d* states of Titanium and the valence band includes *2p* state of Oxygen. Delocalized electronic levels can be formed in the forbidden energy band gap as a result of the electron transfer between the states of Barium and Titanium. The *s* and *p* states within the band gap causes the formation of clusters (TiO_2 or TiO_5) which decrease the band gap emission [23,24].

4.5 Conclusion

Photonic crystal containing BTO defect is fabricated via RF sputtering technique and its reflection spectra reveal a cavity resonance at 532 nm and a 205 nm wide photonic band gap. The cavity resonance occurs at 532 nm at an incident angle 32°. The Q-factor of the microcavity is obtained as 48. The spatial field intensity distribution with respect to angle and wavelength is described using transfer matrix simulation to the fabricated multilayer structure. The results and their analysis clearly indicate the large light-matter interaction and high density of electromagnetic modes at 32°. The enhancement of nonlinear absorption in the microcavity is expressed in terms of enhancement factor G, which is obtained to be 16, by the application of spatial field distribution. The large enhancement is due to the localization of electromagnetic field within the microcavity. The photoluminescence spectra of the reference layer and 1-D PhC have been compared. It is inferred, from a comparative study of the photoluminescence spectra of the reference layer and the 1D PhC, that the large enhancement obtained in the microcavity is due to the strong confinement of the optical field.

4.6 References

[1] K. J. Vahala, “Optical microcavities.” Nature 424, pp839-846 (2003).

[2] Y. Li, L. M. Fortes, A. Chiappini, M. Ferrari, and R. M. Almeida, “High quality factor Er-doped Fabry–Perot microcavities by sol–gel processing.” J. Phys. D: Appl. Phys. 42 p205104 (2009).

[3] R. M. Almeida and A. S. Rodrigues, “Photonic bandgap materials and structures by sol–gel processing.” J. non-cryst. Solids. 326 pp405-409 (2003).

[4] G. J. Lee, Y. P. Lee, S. G. Jung, C. K. Hwangbo, S. Kim and I. Park, “Linear and nonlinear optical properties of one-dimensional photonic crystals containing ZnO defects.” J. Appl. Phys. 102 p073528 (2007).

[5] S. Valligatla, A. Chiasera, S. Varas, P. Das, B. N. S. Bhaktha, A. Lukowiak, F. Scotognella, D. N. Rao, R. Ramponi, G. C. Righini and M. Ferrari, “Optical field enhanced nonlinear absorption and optical limiting properties of 1-D dielectric photonic crystal with ZnO defect.” Opt. Mater. 50 pp229-233 (2015).

[6] N. Tsurumachi, S. Yamashita, N. Muroi, T. Fuji, T. Hattori and H. Nakatsuka, “Enhancement of nonlinear optical effect in one-dimensional photonic crystal structures.” Jpn. J. Appl. Phys. 38 pp6302–6308 (1999).

[7] G. J. Schneider and G. H. Watson, “Nonlinear optical spectroscopy in one-dimensional photonic crystals.” Appl. Phys. Lett. 83 pp5350-5352 (2003).

[8] J. Shen, Z. Zhang, Z. Hua, G. Ma and S. H. Tang, “Observation of two-photon absorption enhancement at double defect modes in one-dimensional photonic crystals.” Appl. Phys. Lett. 88 p011113 (2006).

[9] H. Inouye and Y. Kanemitsu, “Direct observation of nonlinear effects in a one-dimensional photonic crystal.” Appl. Phys. Lett. 82 pp1155-1157 (2003).

[10] R. M. Almeida, A. C. Marques, A. Chiasera, A. Chiappini and M. Ferrari, “Rare-earth doped photonic crystal microcavities prepared by sol–gel.” J. non-cryst. Solids. 353 pp490-493 (2007).

[11] S. Rabaste, J. Bellessa, C. Bonnand, J. C. Plenet and L. Spanhel, “Microcavity strongly doped with CdSe nanocrystals.” Eur. Phys. J. B 42 pp47-50 (2004).

[12] J. Bellessa, S. Rabaste, J. C. Plenet, J. Dumas, J. Mugnier and O. Marty, “Eu^{3+}-doped microcavities fabricated by sol–gel process.” Appl. Phys. Lett. 79 pp2142-2144 (2001).

[13] C. Liao, H. Zhang, L. Tang, Z. Zhou, C. Lv, Y. Cui and J. Zhang, “Nonlinear optical response of semiconductor-nanocrystals-embedded photonic band gap structure.” Appl. Phys. Lett. 104 p171901 (2014).

[14] A. Mecozzi, S. Trillo and S. Wabnitz, “Spatial instabilities, all-optical limiting, and thresholding in nonlinear distributed-feedback devices.” Opt. Lett. 12 pp1008-1010 (1987).

[15] H. G. Schuster, “Nonlinear laser dynamics: from quantum dots to cryptography.” John Wiley & Sons, (2012).

[16] M. Sheik-Bahae, A. A. Said, T. H. Wei, D. J. Hagan and E. W. VanStryland, “Sensitive measurement of optical nonlinearities using a single beam.” IEEE J. Quantum Electron. 26 pp760-769 (1990).

[17] Q. Gong and X. Hu, “Photonic crystals: principles and applications.” Pan Stanford, (2014).

[18] S. Guddala, V. K. Dwivedi, G. Vijaya Prakash and D. N. Rao, “Raman scattering enhancement in photon-plasmon resonance mediated metal-dielectric microcavity.” J. Appl. Phys. 114 p224309 (2013).

[19] Y. Gao, X. Zhang, Y. Li, H. Liu, Y. Wang, Q. Chang, W. Jiao and Y. Song, “Saturable absorption and reverse saturable absorption in platinum nanoparticles.” Opt. Commun. 251 pp429-433 (2005).

[20] R. L. Townsend and J. T. LaMacchia, “Optically induced refractive index changes in $BaTiO_3$.” J. Appl. Phys. 41 pp5188-5192 (1970).

[21] M. Falmbigl, I.S. Golovina, A.V. Plokhikh, D. Imbrenda, A. Podpirka, C.J. Hawley, G. Xiao, A. Gutierrez-Perez, I.A. Karateev, A.L. Vasiliev and T.C. Parker, “$BaTiO_3$ Thin Films from Atomic Layer Deposition: A Superlattice Approach.” J. Phys. Chem. C. 121 pp16911-16920 (2017).

[22] S. Ponelyte and A. Palevicius, “Novel piezoelectric effect and surface plasmon resonance-based elements for MEMS applications.” Sensors 14 (2014) 6910-6921.

[23] L. S. Cavalcante, M. F. C. Gurgel, A. Z. Simoes, E. Longo, J. A. Varela, M. R. Joya and P. S. Pizani, “Intense visible photoluminescence in Ba $(Zr_{0.25}Ti_{0.75})O_3$ thin films.” Appl. Phys. Lett. 90 p011901 (2007).

[24] G. F. G. Freitas, R. S. Nasar, M. Cerqueira, D. M. A. Melo, E. Longo and J. A. Varela, “Luminescence in semi-crystalline zirconium titanate doped with lanthanum.” Mater. Sci. Eng. A. 434 pp19-22 (2006).

Chapter 5

Optical Properties of $BaTiO_3$ in Partially-Symmetric Microcavity

This chapter presents the details of fabrication of two identical microcavities with different thicknesses of defect layer and a study of its role in the nonlinear absorption. Here, it is experimentally realized that with an increase in the thickness of the defect layer, a good reversal from reverse saturable absorption (RSA) to saturable absorption (SA) in response to the angle tuning of the sample is obtained. The spatial field distribution along the depth of the microcavities using transfer matrix simulation shows good consistency with the experimentally obtained results. The photoluminescence emission from the two microcavities of different defect layer thicknesses is compared.

5.1 Introduction

Ultrahigh Q-factor optical cavities find numerous applications in the field of optics such as optical switches [1-4], optical limiting devices [5-7], low threshold lasers [8,9] and quantum electrodynamics [10,11]. Since light is extensively challenging to localize, it is tough to conceive the optical cavities, with dimensions comparable to its wavelength. However, the extensive research that is being carried out in this field due to its huge potential applications, has realized strong confinement of light using photonic crystal microcavities (MC) [12-14].

In this chapter, we discuss the role of thickness of the microcavity for a given wavelength, by fabricating two identical microcavities with different thickness of the defect layer, followed by their optical characterization. Here $BaTiO_3$ (BTO) is placed in between two Bragg mirrors of the 1D PhC comprising of 11 layers of alternating high and low refractive indices of TiO_2 and SiO_2 respectively. Photoluminescence of BTO in both cavities are measured using spectrophotometer while the enhancement in nonlinear absorption coefficients of both cavities are measured using open aperture Z-scan technique with nanosecond (ns) laser and a comparison of the results in both the cases is carried out. In this study, it is experimentally demonstrated that as the thickness of the defect layer is increased, a good reversal from reverse saturable absorption (RSA) to saturable absorption (SA) in response to the angle tuning of the sample is obtained. The spatial field distribution computed along the depth of the microcavities using transfer matrix simulation is in good agreement with the experimental results.

5.2 Experimental details

The 1D PhC microcavities in this study comprise of 23 layers of SiO_2-TiO_2 with BTO as defect layer with the difference in the defect layer thickness. These are prepared using RF magnetron sputtering technique and the experimental details are explained in section 2.3.2. The refractive index of single layer of each material is measured with white light ellipsometer (J.A. Woollam, M2000V), and the experimental details are presented in section 2.2. The

Bragg mirrors of 1D PhC is fabricated using the SiO_2 and TiO_2 nano-layers with quarter-wave (λ/4) thickness of 90 nm and 55 nm, respectively, and the defect layer is fabricated using BTO with half-wave (λ/2) thickness of 130 nm for the first microcavity (MC1) and $2\lambda/3$ (173 nm) for the second microcavity (MC2) at the operation wavelength λ=532nm. The fabrication procedure is same as explained in section 4.2 and the experimental details are discussed in section 2.3.2.

The cross-sectional morphology and reflection spectrum of MC1 and MC2 are studied using FESEM (Zeiss, Ultra^{TM}55), and the UV-visible spectrophotometer (Jasco V-670 Spectrophotometer). The enhancement in nonlinear optical absorption is investigated through Z-scan technique with 532 nm nanosecond laser pulses (pulse width 6 ns, repetition rate of 10 Hz) generated from the Nd:YAG laser (Spectra-Physics), and the photoluminescence is recorded using photoluminescence spectrophotometer (Fluorolog, Horiba Jobin Yvon).

5.3 Numerical simulations

We numerically simulate the electric field distribution and field confinement inside the microcavity using transfer matrix formalism (TMM) [15]. The detailed theory of TMM formalism is discussed in section 2.6. The spatial distribution of the spectrally resolved TE mode intensity ($|E|^2$) along the length of the cavity through MC1 at an angle 32˚ is shown in Figure 5.1(a) and that of MC2 at an angle of 20° is shown in Figure 5.1(b). A dark region extending from 500 nm to 700 nm represents the photonic band gap (PBG) of the MC1 and the same for MC2 as shown in Figure 5.1(b) is ranging from 450 nm to 700 nm. The bright discrete line-shaped intensities (white-coloured dashed encircled area) correspond to the resonance mode at 532 nm. Figure 5.1(c) and 5.1(d) show the angle resolved intensity distribution for the wavelength 532 nm for MC1 and MC2 respectively. The maximum light confinement in the BTO layer is seen to occur at an angle of 32° for MC1 and at 20° for MC2 (white-coloured dashed encircled area). Simulated spatial TE field intensity distribution is overlapped with refractive index profile of the MC1 at 32° is shown in Figure 5.1(e) and that

of MC2 at 20° in Figure 5.1 (f). The intensity maxima at the central defect layer imply a strong localization of optical fields in the microcavity. These results support the use of BTO defect containing 1D PhC to enhance the nonlinear optical effects, which will be discussed in the following sections.

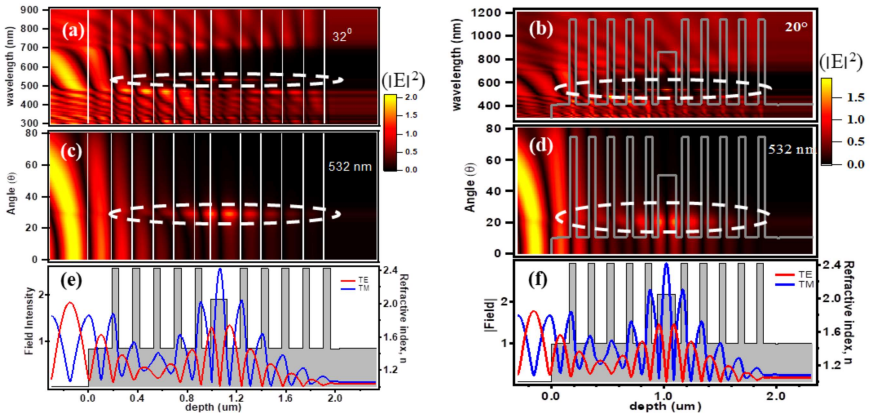

Figure 5.1: *Simulated spatial distribution mapping of the Transverse Electric (TE) field (|E|) in the MC1* and MC2 versus (a), (b) wavelength and (c), (d) incident angle. (e), (f) Simulated spatial distribution of the TE and TM Field intensity (|H|) and |E|) inside MC1 and MC2 and the refractive indices profile of both at 32° and 20° for 532 nm. *MC1 is already discussed in Chapter 4.*

5.4 Results and Discussions

The microcavities, MC1 and MC2 with the defect BTO layer thickness $\lambda/2$ and $2\lambda/3$ respectively constitute 1D PhC of total 23 layers. The quarter wave thickness of SiO_2 and TiO_2 forms the Bragg mirrors (BM) on either side of the defect layers of both microcavities. Figure 5.2 (a) and (b) represents the cross sectional FESEM image of MC1 and MC2 where the dark and bright regions correspond to SiO_2 and TiO_2 respectively with central thick bright layer of BTO. The thickness of the SiO_2 and TiO_2 of BM's of MC1 and MC2 estimated from FESEM image are $93\pm5\ nm$ and $53\pm5\ nm$ respectively while that of the BTO layer is $133\pm5\ nm$ and $170\pm5\ nm$ respectively.

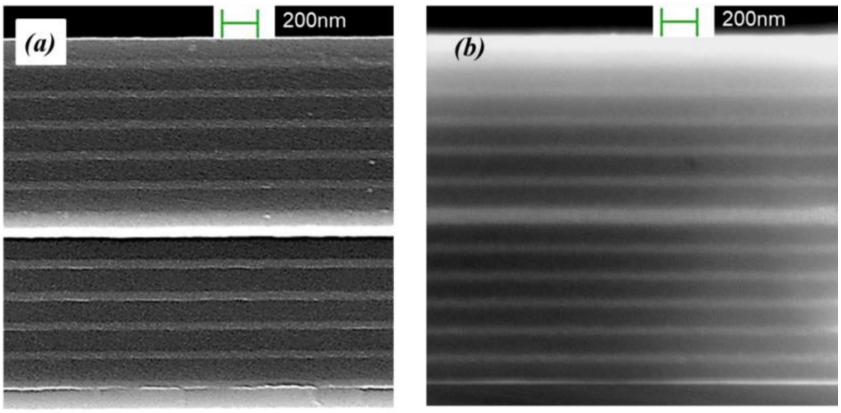

Figure 5.2: *(a) FESEM images of MC1* and (b) MC2. *MC1 is already discussed in Chapter 4.*

Figure 5.3 (a) and (b) show the experimental and simulation reflection spectra of MC2 at normal incidence with the pass band at 540 nm. It can be seen that the theoretical simulation and experimental results are in good agreement.

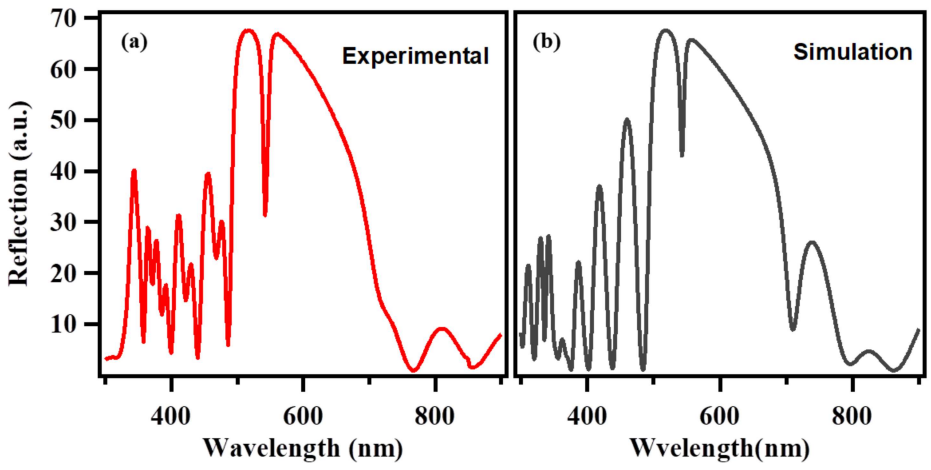

Figure 5.3: *Experimental and simulated reflection spectrum of MC2 at normal incidence.*

The angle tuned reflection spectra with a step size of 10° shown in Figure 5.4 (a) and (b) of MC1 and MC2 respectively demonstrate the wide tunability of PhC's. Here the band gap of MC1 ranges from 557 nm at 10° to 480 nm at 60° and that of MC2 ranges from 539 nm at 10° to 460 nm at 60°. The reason for this noticeable blue shift with the angle tuning of the sample can be understood using the equation 4.1 which is explained in section 4.4. Since our working wavelength is 532 nm, the sample MC1 is kept at 32° and MC2 at 20° for nonlinear optical studies.

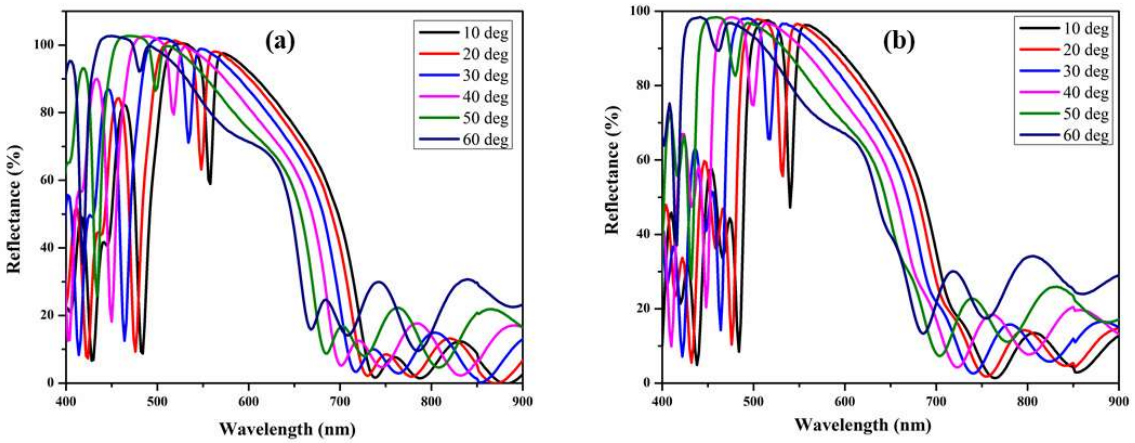

Figure 5.4: *Angle tuned reflection spectrum of (a) MC1* and (b) MC2 with a step size of 10°.*
**MC1 is already discussed in Chapter 4.*

	Parameters	Simulation (nm)	Experiment (nm)
MC 2	Thickness of the layers		
	SiO_2	110	93±5
	TiO_2	58	53±5
	$BaTiO_3$	164	170±5
	Band gap at 20°		
	Central Wavelength	532	532
	FWHM (nm)	200	202
	Pass band at 20°		
	Central Wavelength	532	532
	FWHM (nm)	7.2	8
	Q-factor	74	67

Table 5.1 *The summarized fabricated and simulated 1D PhC parameters of MC2.* **MC1 is already discussed in Chapter 4.*

5.4.1 Nonlinear Absorption Studies

The Z- scan technique is used to investigate the nonlinear absorption characteristics of MC1 and MC2, the experimental details of which are given in section 2.5.2. Open aperture Z-scan technique [16] is utilised to measure the nonlinear absorption of BTO in MC1 and MC2 for different incident angles. A frequency doubled Nd:YAG pulsed laser at the wavelength 532 nm (with 6 ns pulse width, and 10 Hz repetition rate) is focused on each of the samples using a plano-convex lens of focal length 120 mm and the output intensity is collected with a large area fast photodiode. The experiment is carried out at the input laser intensity of 0.18 GW/cm^2. The normalized transmittance from the theory of open aperture Z-scan is stated as

$$T = 1 + \frac{\beta I_0 L_{eff}}{2^{3/2}\left(1+\left(z/z_0\right)^2\right)} \qquad (5.1)$$

where, β is the effective two photon absorption coefficient, I_0 is the on-axis peak intensity at the focus, L_{eff} is the effective interaction length, z is the sample position and z_0 is the Rayleigh range. The normalized open aperture Z scan curves of the MC1 and MC2 at normal incidence with the single reference layer of BTO are exposed in Figure 5.5(a) and (b) respectively. The experimentally obtained data is fitted using equation 5.1. The experimental data points of both cavities are shown in green dots whereas the green solid curves represent the fitted curves and the black dots and black solid curves respectively represent the experimental and fitted curves of BTO reference layer. Here MC1 shows SA behavior and MC2 shows RSA behavior at normal incidence for the laser intensity of 0.18 GW/cm^2 and it is observed that the nonlinear behaviour of reference BTO layer is about six orders of magnitude lower ($\alpha(I)$ = -1.86×10^{-10} cm/W) as compared to the microcavity. This clearly illustrates the cavity enhancement of the BTO layer due to the localisation of photon in the microcavity.

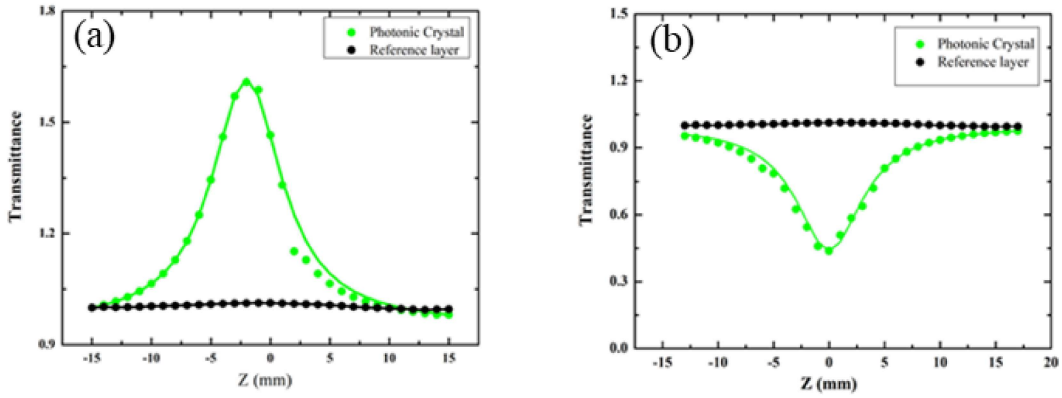

Figure 5.5: *Z scan curves showing corresponding to the BTO reference (black) and 1DPhC with BTO defect (green) of (a) MC1* and (b) MC2 at normal incidence. *MC1 is already discussed in Chapter 4.*

The angle tuned Z-scan measurements of MC1 and MC2 are shown in Figure 5.6 (a) and (b) respectively. Figure 5.6 (a) shows Z-scan curves of MC1 for the incident angles 0º, 20º and 32º and the Z-scan curves of MC2 for the incident angles 0°, 10°, 20° and 30° are shown in Figure 5.6(b). MC1 shows SA behaviour for all the angles of incidence and maximum absorption is obtained at an incident angle of 32°. MC2 shows switching behaviour from RSA to SA as it is tuned for higher angles for the same intensity of the laser beam.

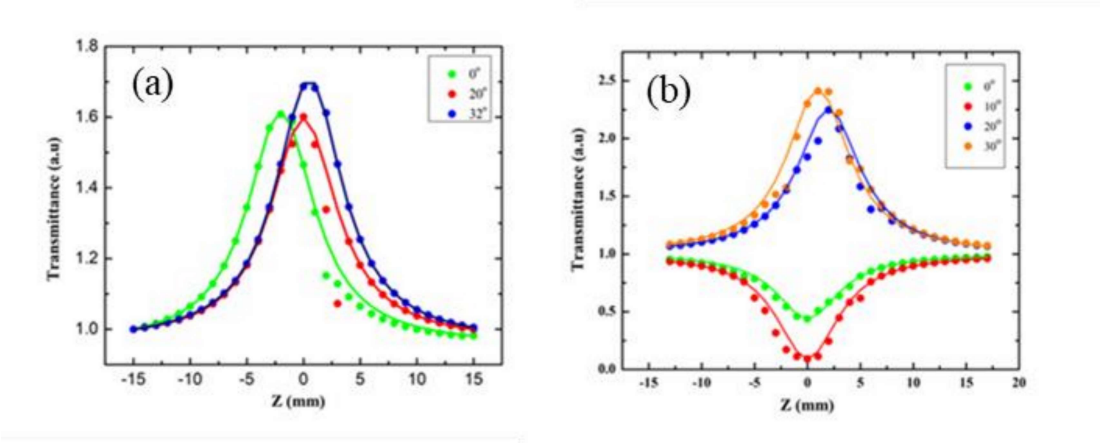

Figure 5.6: (a) *Open aperture Z- scan curves of the MC1* for the incident angles 0°, 20° and 32°. (b) Open aperture Z- scan curves of the MC2 for the incident angles 0°, 10°, 20° and 30°.* **MC1 is already discussed in Chapter 4.*

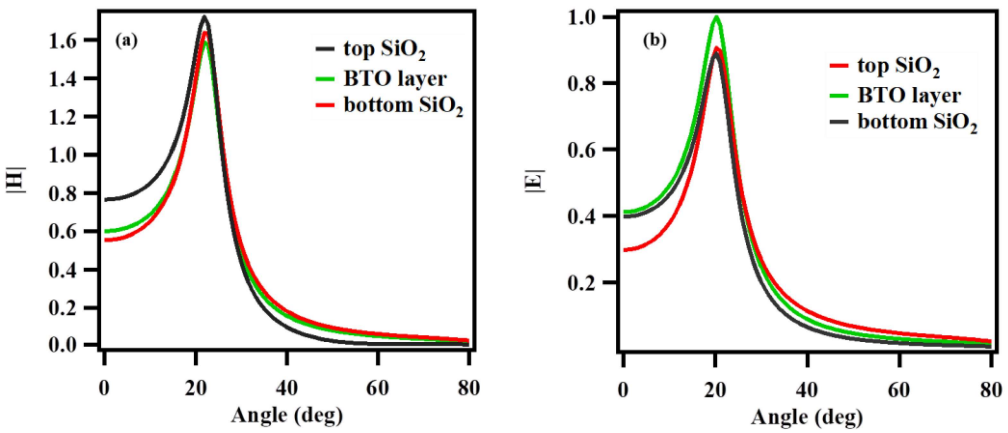

Figure 5.7: *Angle resolved spatial field distribution of (a) TM and (b) TE mode ((|H|) and (|E|)) within BTO layer in MC.*

To understand the above behaviour, we simulated the spatial field (|H|, |E|) profiles for the TM and TE modes at two different angles (10° and 30°) for MC2. Figure 5.7(a) and (b) show the field profile of MC2 at different angles (10° and 30°) in BTO layer and the two neighbouring silica layers. It is clear that the total TM and TE modes are stronger in BTO at higher angles compared to the field confinement nearby silica layers on both sides of BTO for lower angles of incidence. Therefore, it can be concluded that the dominant two photon absorption (TPA) from silica layers is leading to RSA behaviour. The study on the MC1 has yielded a simple saturation of absorption behaviour for all angles. Thus, as we vary the thickness of the defect layer it is clear that for best nonlinear absorption, one may have to choose an optimum thickness as at MC2. As we move from MC1 to MC2, we see a very good reversal of RSA to SA. The estimates of nonlinear saturable absorption coefficient $\alpha(I)$ and effective two photon absorption coefficient $\beta(I)$ of MC1 and MC2 are shown in Table 5.2.

Angle	$\alpha(I)$ (cm/W)	$\beta(I)$ (cm/W)
MC 1*		
0°	-1.30×10^{-4}	NA
20°	-1.22×10^{-4}	NA
32°	-1.45×10^{-4}	NA
MC 2		
0°	NA	1.05×10^{-4}
10°	NA	1.70×10^{-4}
20°	-2.35×10^{-4}	NA
30°	-2.67×10^{-4}	NA

Table 5.2: *Estimates of nonlinear absorption coefficients of MC1 and MC2: nonlinear saturable absorption coefficient α(I) and effective two photon absorption coefficient β(I).* **MC1 is already discussed in Chapter 4.*

5.4.2 Photoluminescence emission

The photoluminescence emission of the samples is recorded using photoluminescence spectrophotometer (Fluorolog, Horiba Jobin Yvon) and its experimental specifications are given in section 2.4.3. The linear absorption spectra of BTO reference film of MC1 and MC2 are shown in Figure 5.8 (a) and (b). The observed peaks of BTO reference film of MC1 is at 296 nm and 355 nm whereas the peaks of BTO reference film of MC2 are occurring at 290 nm and 357 nm, which correspond to the interband transitions.

Figure 5.9(a) displays the PL emission spectra of the BTO single layer (133 nm) and MC1 with excitation, λ_{exc} = 355 nm and the emission peak of both is observed at 424 nm while the emission spectra of the reference BTO layer of MC2 and PhC (MC2) with an excitation wavelength λ_{exc} = 357 nm is shown in Figure 5.9(b). In the case of MC2, the emission of reference BTO layer and MC2 is observed at 432 nm. The cavity effect reduces full width at half maximum (FWHM) of the spectra of MC1 and MC2 when compared to that of its

reference layers. Q-factor of the microcavities is assessed from the PL emission spectrum by computing $\lambda/\Delta\lambda$ at the resonance wavelength, which is found to be 6 for MC1 and 7 for MC2. This indicates that the quality factors of both cavities are almost same. The physical mechanism behind this PL emission is explained in section 4.4.2.

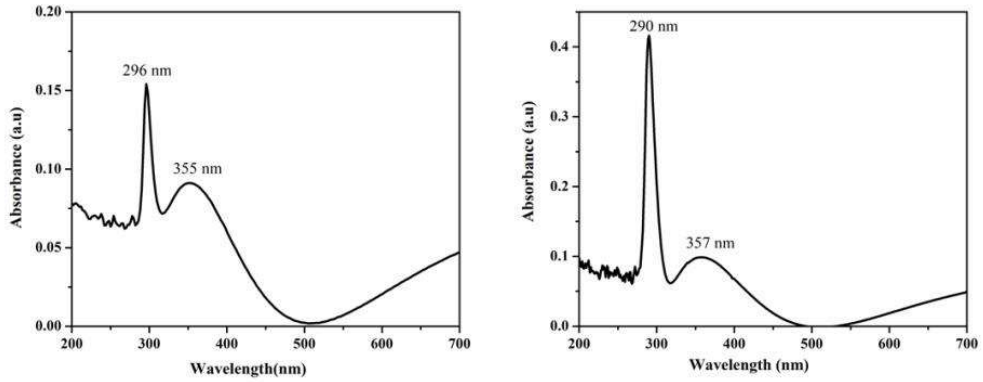

Figure 5.8: *(a) Absorption spectrum of BTO reference film of MC1* and (b) MC2. *MC1 is already discussed in Chapter 4.*

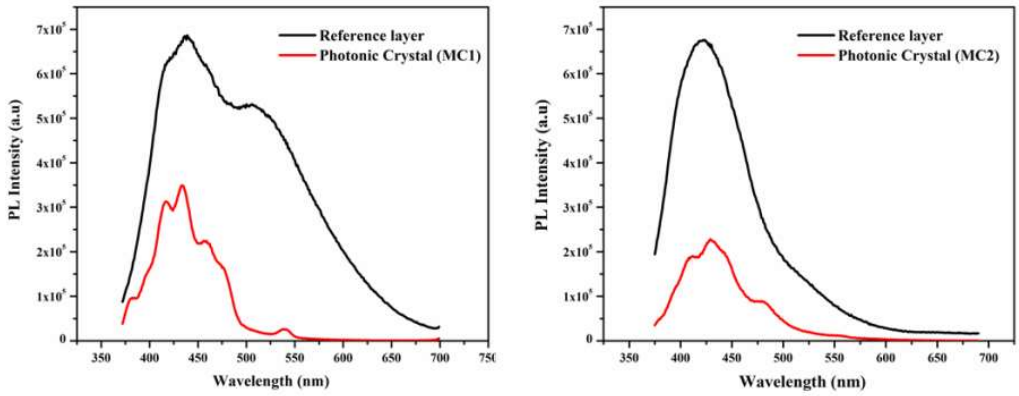

Figure 5.9: *(a) The photoluminescence spectra of single reference BTO layer (133 nm) and MC1* with λ_{exc}= 355 nm. (b) PL emission spectra of BTO reference layer (170 nm) and MC2 with λ_{exc}=357 nm. *MC1 is already discussed in Chapter 4.*

5.5 Conclusion

1D Photonic microcavities MC1 and MC2 with BTO defect layer are interpolated between DBR's of SiO_2 and TiO_2, which are fabricated through RF sputtering technique. The reflection spectra show the cavity resonance at 532 nm at an angle of incidence 32° for MC1 and at 20° for MC2. The open aperture Z-scan indicates an enhancement in nonlinear absorption in both the microcavities and an abnormal switching behaviour from RSA to SA for MC2 is observed for higher angle of incidence for the same intensity of the laser beam compared to MC1, where it shows SA behaviour for all the angles of incidence. Varying the thickness of defect layer, it is found that the best nonlinear absorption is obtained at an optimum thickness of BTO as in MC2. The transfer matrix simulation also shows field confinement both at lower and higher angles of incidence. The photoluminescence spectra of both reference layers and the respective microcavities are compared. The cavity effect reduces full width at half maximum (FWHM) of both the samples compared to its reference layers and it shows the quality factors of both cavities are almost same.

5.6 References

[1] R. Katouf, T. Komikado, M. Itoh, T. Yatagai and S. Umegaki, "Ultra-fast optical switches using 1D polymeric photonic crystals.", Photonics Nanostructures: Fundam. Appl. 3(2-3), pp116-119 (2005).

[2] A. Haché and M. Bourgeois, "Ultrafast all-optical switching in a silicon-based photonic crystal.", Appl. Phys. Lett. 77(25), pp4089-4091 (2000).

[3] K. Nozaki, T. Tanabe, A. Shinya, S. Matsuo, T. Sato, H. Taniyama and M. Notomi, "Sub-femtojoule all-optical switching using a photonic-crystal nanocavity."Nat. Photonics 4(7), p477 (2010).

[4] C. Husko, A. De Rossi, S. Combrié, Q. V. Tran, F. Raineri and C. W. Wong, “Ultrafast all-optical modulation in GaAs photonic crystal cavities.”, Appl. Phys. Lett.94(2), p021111 (2009).

[5] M. V. Vijisha, V. V. Sini, N. S. Narendran and K. Chandrasekharan, “Enhanced nonlinear optical response from dihydroxy (5, 10, 15, 20-tetraphenyl porphyrinato) tin (iv) or SnTPP in a fully plastic photonic crystal microcavity.”, Phys. Chem. Chem. Phys. 19(43), pp29641-29646 (2017).

[6] B. Y. Soon, J. W. Haus, M. Scalora and C. Sibilia, “One-dimensional photonic crystal optical limiter.” Opt. Express 11(17), pp2007-2018 (2003).

[7] J. S. Shirk, “Protecting the war fighter's vision in a laser-rich, battlefield environment.” Opt. Photonics News 11(4), pp19-23 (2000).

[8] T. W. Lu, L. H. Chiu, P. T. Lin and P. T. Lee, “One-dimensional photonic crystal nanobeam lasers on a flexible substrate.”, Appl. Phys. Lett. 99(7), p071101 (2011).

[9] T. W. Lu, W. C. Tsai, T. Y. Wu and P. T. Lee, “Laser emissions from one-dimensional photonic crystal rings on silicon-dioxide.”, Appl. Phys. Lett. 102(5), p051103 (2013).

[10] Y. Liu and A. A. Houck, “Quantum electrodynamics near a photonic bandgap.”, Nat. Phys. 13(1), 48 (2017).

[11] M. Lermer, N. Gregersen, F. Dunzer, S. Reitzenstein, S. Höfling, J. Mørk and A. Forchel, “Bloch-wave engineering of quantum dot micropillars for cavity quantum electrodynamics experiments.” Phys. Rev. Lett.108(5), p057402 (2012).

[12] Y. Akahane, T. Asano, B. S. Song and S. Noda, “High-Q photonic nanocavity in a two-dimensional photonic crystal.”, Nature 425(6961), p944 (2003).

[13] P. Lalanne, C. Sauvan and J. P. Hugonin, “Photon confinement in photonic crystal nanocavities.”, Laser Photonics Rev. 2(6), pp514-526 (2008).

[14] J. Bravo-Abad, A. Rodriguez, P. Bermel, S. G. Johnson, J. D. Joannopoulos and M. Soljačić, “Enhanced nonlinear optics in photonic-crystal microcavities.”, Opt. Express, 15(24), pp16161-16176 (2007).

[15]] P. Yeh, “Optical waves in layered media.” New York: Wiley 95 (1988).

[16] M. Sheik-Bahae, A. A. Said, T. H. Wei, D. J. Hagan and E. W. Van Stryland, “Sensitive measurement of optical nonlinearities Using a single beam.” IEEE J. Quantum electronics 26 (4), pp760-769 (1990).

Chapter 6

Optical Properties of $BaTiO_3$ in Asymmetric Microcavity

This chapter discusses an enhanced and switching non-linear absorption behaviour of $BaTiO_3$ in an asymmetric 1-D photonic microcavity, in which the thickness of micro layers violates Bragg's condition. The microcavity is fabricated using RF magnetron sputtering and the nonlinear absorption is examined in an open aperture Z-scan. The nonlinear switching behaviour from reverse saturable to saturable absorption is observed near an incident angle of 25°. The study reveals that the SA behaviour dominates over RSA for the higher thickness of BTO defect layer. We also have carried out numerical simulations of the system studied here using transfer matrix formalism to understand the unusual switching behaviour that is observed. The study also shows enhancement in photoluminescence emission with a Q-factor of 30.

6.1 Introduction

A one-dimensional photonic crystal (1D PhC) is a binary dielectric periodic structure, which can form a photonic band gap (PBG) [1-5]. A lot of research activities have been initiated in the field of photonic crystals and PBG effects have already been realized in such photonic systems [6-9]. Violating the perfect Bragg's condition for the preparation of multilayers leads to a cavity that can be defined as asymmetric microcavity.

In this chapter, we demonstrate the switching behaviour in nonlinear absorption from reverse saturable absorption (RSA) to saturable absorption (SA) as we angle tune the sample. Unlike in the case of the previous samples in which only the defect layers are prepared in such a way as to violate the Bragg's condition, here both the Bragg mirrors as well as the defect layer violate the Bragg's condition of thickness. This leads to a more dominant SA behaviour as opposed the RSA behaviour unlike the previous case. It also gives the enhancement in nonlinear absorption and photoluminescence of $BaTiO_3$ (BTO) in a 1-D asymmetric photonic microcavity. The asymmetric 1D PhC is fabricated using BTO as the defect layer with a thickness $3\lambda/4$ between the two Bragg mirrors composed of 9 layers of high and low refractive indices of titanium dioxide (TiO_2) and silicon dioxide (SiO_2) respectively with arbitrary thicknesses (chosen to be $\lambda/3$ and $\lambda/7$ in this case) as shown in Figure 6.1(a). The open aperture Z-scan shows the enhancement in nonlinear absorption while the photoluminescence is measured using spectrophotometer. For the design of the photonic 1-D structures, the transfer matrix simulations as well as the experimental results show the same PBG effect that also is present for the asymmetric structures. The structures studied here show an unusual behaviour in nonlinear absorption compared to the usual photonic crystal microcavity. Further, when the thickness of the defect layer (BTO) increases, the SA behaviour dominates which obscures RSA behaviour. The experimental results are in good agreement with the simulated optical properties of the 1-D asymmetric microcavity using optical transfer matrix formalism.

6.2 Details of the Experiment

The asymmetric dielectric microcavity comprises 19 layers of SiO_2-TiO_2 with BTO as defect layer, is prepared using RF magnetron sputtering technique, the experimental details of which are explained in section 2.3.2. Figure 6.1 (a) represents the schematic structure of asymmetric photonic microcavity consisting of two Bragg mirrors on both sides of a BTO defect layer. The refractive index of single layer of each material is measured using white light ellipsometer (J.A. Woollam, M2000V), which is a crucial information for fabricating the proposed structure. The ellipsometric measurements of the refractive index of each layer of SiO_2, TiO_2 and BTO at 532 nm wavelength are found to be 1.48, 2.42 and 2.05 respectively. The optimized deposition time for the optical thicknesses of SiO_2 ($\lambda/7$), TiO_2 ($\lambda/3$) and BTO ($3\lambda/4$) for a wavelength 532 nm are 18, 28 and 65 minutes respectively, to obtain the band gap in the visible region. The targets used are of 2-inch diameter with a thickness of 3 mm. The asymmetric MC is fabricated on silica substrate using a multi-target sputtering system (Advanced Process Technology, India). High vacuum inside the chamber is attained, with a residual pressure of 4.9×10^{-6} mbar which is then filled with Ar gas to a pressure of 5.5×10^{-3} mbar prior to the sputtering process. The first Bragg mirror, consisting of 9 alternate layers, is deposited on the silica substrate by sputtering SiO_2 and TiO_2 targets with RF power of 150 W and 130 W respectively. Next, the presure is increased to 7.5×10^{-3} mbar and then the BTO is deposited at an RF power of 75 W. The second Bragg mirror is deposited on top of the BTO layer as mentioned previously, reducing the pressure back to the initial value. The substrate is rotated at 20 rpm during the film deposition to obtain uniformity of the film thickness. The FESEM image of the fabricated structure is shown in Figure 6.1(b).

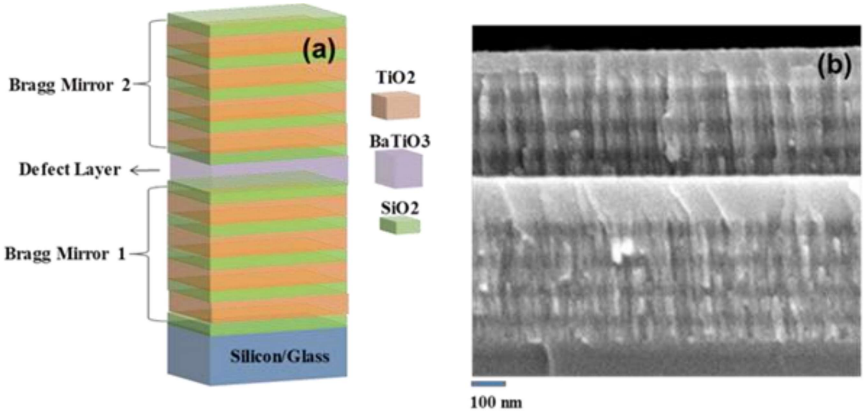

Figure 6.1: *(a) Schematic representation of asymmetric photonic microcavity consists of two Bragg mirrors on both sides of the BTO defect layer. (b) FESEM Image of the same.*

The reflection spectrum and cross-sectional morphology of the asymmetric microcavity is recorded using UV-Visible-Near IR spectrophotometer (Jasco V-670 Spectrophotometer), and the field emission scanning electron microscope (FESEM, Zeiss, Ultra^{TM}55). The nonlinear optical absorption is investigated using Z-scan technique with 532 nm nanosecond laser pulses (pulse width 6 ns, repetition rate of 10 Hz) coming out of an Nd:YAG laser (Spectra-Physics). The photoluminescence is recorded in the wavelength range 400-900 nm using photoluminescence spectrophotometer (Fluorolog, Horiba Jobin Yvon) for a reference of single layer of BTO (200 nm) and in the photonic microcavity fabricated as discussed above and the results are compared.

6.3 Results and Discussion

The 1-D asymmetric MC with 3λ/4 thickness of BTO as defect constitutes the microcavity with total nineteen layers, with each layer of SiO_2 having a thickness λ/7 and each layer of TiO_2 having thickness λ/3 on either side of the defect layer. Figure 6.1(b) represents the cross sectional FESEM image of the microcavity with BTO as defect. The dark and bright regions correspond to SiO_2 and TiO_2 respectively and the central thick bright layer is due to BTO. The thickness of the SiO_2, TiO_2 and BTO estimated from FESEM image are 55±5 *nm*, 73±5

nm and 199±5 *nm* respectively and the thickness of the entire multilayer is 1.3 *μm*. Figure 6.2(a) illustrates the reflection spectrum of the microcavity at an incident angle of 30°. The solid line shows the theoretical fit and the curve with red solid circles represents the experimental data. As can be seen, the experimental results are in good agreement with the theoretical simulations. The photonic microcavity's band-gap ranges from 446 *nm* to 638 *nm*. The pass band, which is also referred to as the cavity resonance mode, is occuring at 532 *nm* inside the photonic band-gap.

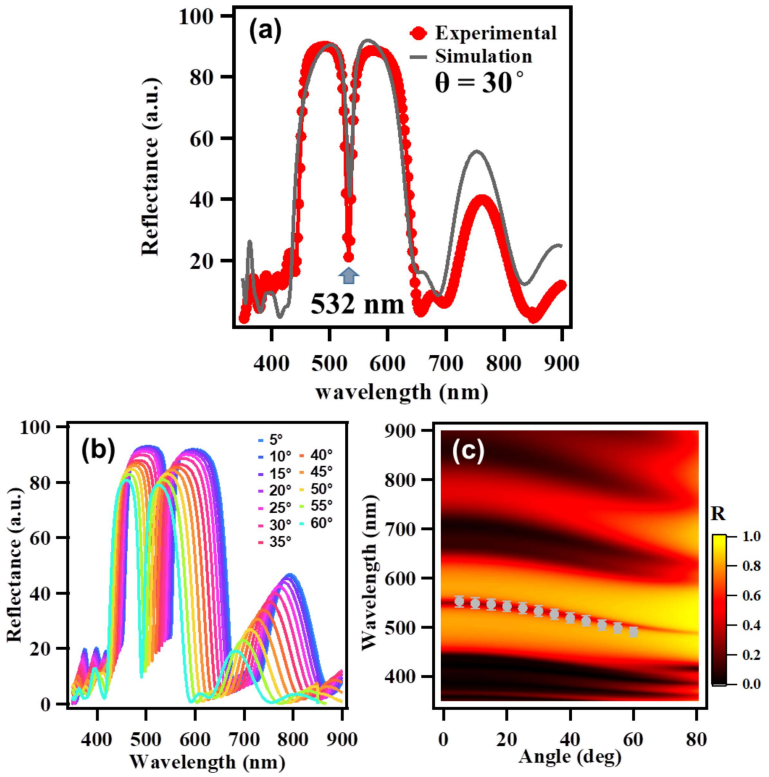

Figure 6.2: *(a) The reflection spectrum of asymmetric microcavity shows a band gap with the pass band at 532 nm. (b) Experimental reflection spectra at different angles and (c) transfer matrix simulation of angle vs wavelength intensity mapping. Solid grey symbols are the cavity peak values of experimental results (Figure 6.2 b)*

The angle-resolved reflection spectra are shown in Figure 6.2(b). The position of the pass band is blue shifted with higher angle of incidence. This can be attributed to the shortening of lattice constant experienced by the incident electromagnetic wave with an increase of the incident angle, given by the relation [10,11],

$$\lambda(\theta) = \lambda(0) \times (1 - Sin^2(\theta) / n_{eff}^2)^{1/2} = \lambda(0) \times (Cos^2(\theta) / n_{eff}^2)^{1/2} \quad (6.1)$$

Where $\lambda(0)$ and $\lambda(\theta)$ are respectively denote the cavity peak positions for 0^0 and θ^0 angles of incidence, and n_{eff} denotes the effective refractive index. The cavity resonance appears at 552 nm at an angle of 5° and 490 nm at an angle of 60° which indicates a wide tunability of the 1-D asymmetric MC. The simulated angle dependent reflection spectral mapping of the microcavity using transfer matrix method is shown in Figure 6.2 (c). The yellow region expands from 460 nm to 650 nm, which represents the stop band of the microcavity and the central dark red line shape denotes the resonance mode (pass band). The solid dark circles represent the experimental pass band peaks overlapped with the simulation. Since our laser source is at 532 nm for the characterization, we fix the pass band exactly at 532 nm at an angle of incidence 30°. This geometry is used to measure the nonlinear absorption by the Z-scan technique.

Parameters	Simulation (nm)	Experiment (nm)
	Thickness of the layers	
SiO_2	55	55±5nm
TiO_2	72	73±5 nm
$BaTiO_3$	177	199±5 nm
	Band gap at 30°	
Central Wavelength	532 nm	532 nm
FWHM (nm)	185	188
	Pass band at 30°	
Central Wavelength	532 nm	532 nm
FWHM (nm)	11	7.5
Q-factor	48	71

Table 6.1: *Summary of fabricated and simulated 1D asymmetric microcavity parameters*.

Since the experimental focus is on the nonlinear studies using Z-scan, it becomes vital to visualize the optical field profile within the microcavity at the laser excitation wavelength 532 nm. Figure 6.3 shows the simulations for transverse electric (TE) and transverse magnetic (TM) field distributions using the microcavity parameters given in Table 6.1. Results show that at an angle of incidence 30°, the laser light excitation at 532 nm is better confined within the cavity. The field ($|E|^2$) maxima at the central defect layer implies the strong localization of optical fields in the microcavity. The spectrally resolved TE optical field spatial distribution along the length of the microcavity at an angle 30° is shown in Figure 6.3(a). The low intensity (dark) region ranging from 446 nm to 638 nm denotes the band gap of the 1-D asymmetric MC, and bright discrete line-shaped intensities (in the white-coloured dashed encircled area) correspond to the resonance mode at 532 nm. Figure 6.3(b) shows the TE and TM field distribution over the depth of the microcavity with refractive index profile at 532nm and for light incident angle of 30°. Figure 6.3(c) and 6.3(d) show the

angle resolved field distribution at wavelength 532 nm for TE and TM modes. The maximum optical confinement in the BTO layer is obtained at an angle of 30° (white-coloured dashed encircled area). These results support that defect layer of BTO in an asymmetric microcavity will enhance optical effects at 532 nm for the incident angle of 30°, which will be further discussed in the following sections.

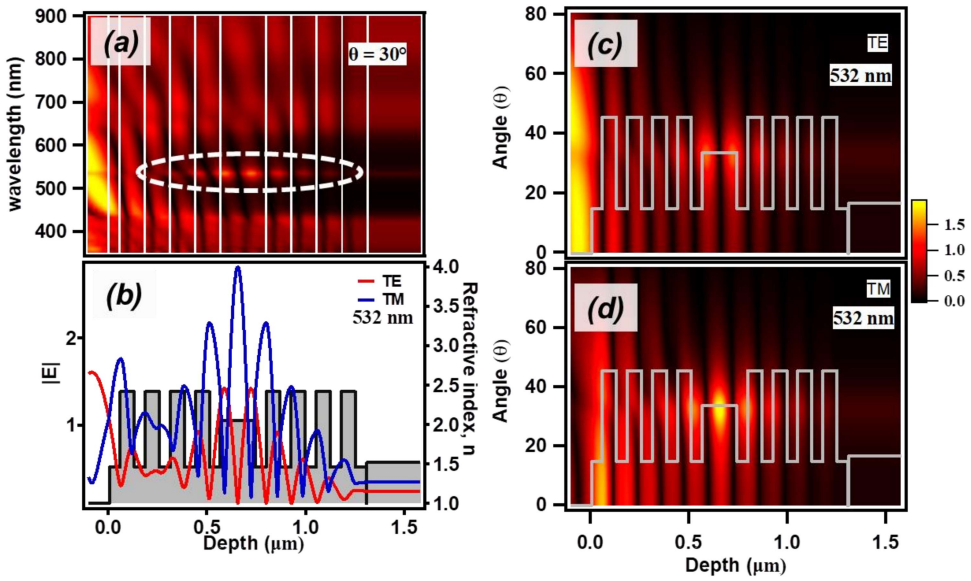

Figure 6.3: *Transfer matrix simulation of (a) spatial-wavelength (at 30°) mapping (b) spatial distribution of the transverse electric (TE) and transverse magnetic (TM) field profiles along the length of the 1D PhC at 30° angle and for 532 nm wavelength. Angle resolved (at 532nm) spatial field distribution mapping of (c) TE field and (d) TM field.*

6.3.1 Nonlinear absorption studies

For measuring the nonlinear optical absorption, the sample is aligned in such a way that the 532 nm laser beam makes an incident angle of 30° with the sample. From the theory of open aperture Z-scan [12], the coefficient of saturable absorption is given by,

$$\alpha(I) = \frac{\alpha_0}{1 + I_z / I_S} \qquad (6.2)$$

Where, α_0 is the linear absorption coefficient, I_z and I_s are respectively the laser intensity at any position z and the saturation intensity for BTO. Laser radiation intensity I_z is given by

$$I_z = \frac{I_0}{1+\left(\frac{z}{z_0}\right)^2} \tag{6.3}$$

Where I_0 is the peak intensity at the centre of the focus, z is the sample position, $z_0 = \frac{\pi\omega_0^2}{\lambda}$ is the Rayleigh range, ω_0 is the beam waist at the focal point *(z* = 0), λ is the laser wavelength. The normalized transmittance for the open aperture Z-scan is expressed as

$$T = 1 + \frac{\beta I_0 L_{eff}}{2^{3/2}\left(1+\left(z/z_0\right)^2\right)} \tag{6.4}$$

Where, $L_{eff} = (1-e^{-\alpha_0 L})/\alpha_0$, z is the longitudinal displacement of the sample from the focus (z=0), β is the effective two photon absorption (TPA) coefficient, I_0 is the on-axis peak intensity at the focus, L_{eff} is the effective interaction length, α_0 is the linear absorption coefficient and L is the sample length. The normalized open aperture Z scan curves of the asymmetric dielectric microcavity and the single reference layer of BTO are shown in Figure 6.4(a). The experimental data points are shown in red and black dots corresponding to the 1-D asymmetric dielectric microcavity and the reference BTO layer. The experimental data is fitted using equation (6.4) given above and the solid line in the figure represents the fitted curves. The asymmetric dielectric MC shows saturable absorption at an incident angle 30° for a laser intensity of 0.14 GW/cm^2 and a comparison shows that the nonlinear behaviour of reference BTO layer is about six order of magnitude lower ($\alpha(I)$ = -1.29×10^{-10} cm/W) than the microcavity. This clearly reflects the strong photon confinement and the cavity enhancement of the BTO layer.

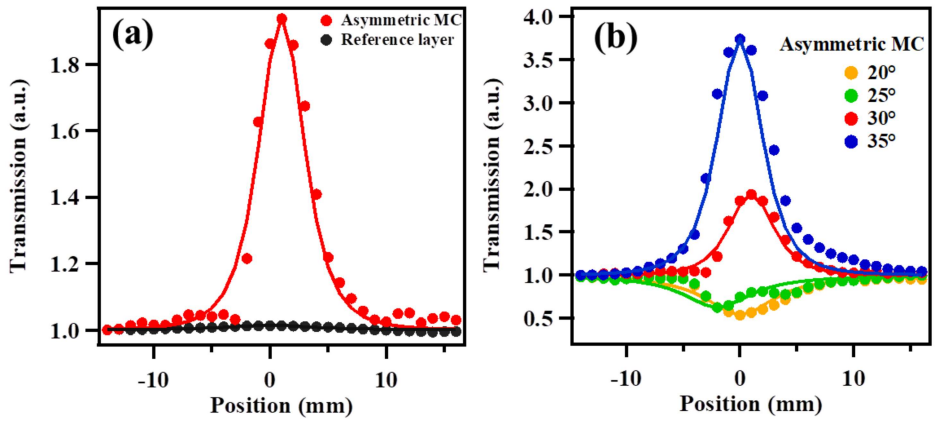

Figure 6.4: *(a) Open aperture Z- scan curves of the asymmetric microcavity (red) along with reference BTO layer (black). (b) Open aperture Z- scan curves of the 1D asymmetric dielectric microcavity for the incident angles 20°, 25°, 30° and 35°.*

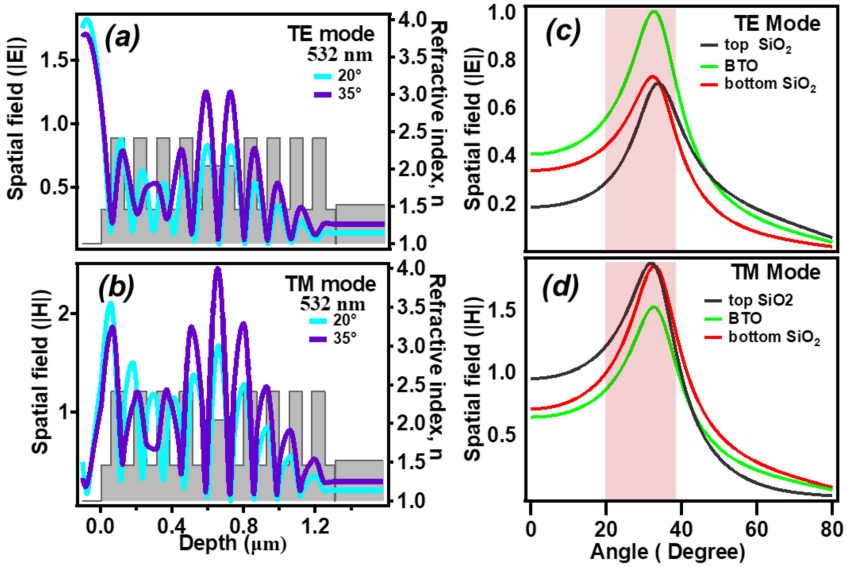

Figure 6.5: *Spatial field profiles at 20° and 35° along the depth of the microcavity for (a) TE (b) TM modes. Angle tuned spatial optical field within BTO defect layer and two neighbouring SiO_2 layers of the microcavity for (c) TE and (d) TM modes.*

The angle tuned Z-scan measurement of the MC is shown in Figure 6.4(b). The sample shows switching behaviour from reverse saturable absorption (RSA) to saturable absorption (SA),

by tuning to higher angles, at the same intensity of the laser beam. In order to understand this behaviour, we simulated the spatial field (|E|, |H|) profiles for the TE and TM modes at two different angles 20° and 35° (see Fig. 6.5a, 6.5b). Figure 6.5(c) and 6.5(d) exclusively show the field profile at different angles in BTO layer and the two neighbouring silica layers. It is obvious from these figures that the total TE and TM modes in both the silica layers put together is stronger compared to that in BTO layer at lower angles. However, for larger angles the field confinement in the $BaTiO_3$ layer increases. At larger angles the field confinement in BTO leads to saturation effects as the excitation falls within the band arising due to the defect states of BTO [13]. Whereas at lower angles the TM optical field intensity in both silica layers is much higher (Fig. 6.5(d)) than that in BTO layer. Therefore, it can be concluded that the dominant TPA is from silica layers, leading to an RSA behaviour. Earlier studies on the symmetric cavity has yielded a simple saturation of absorption behaviour for all angles [13]. The present result shows that, with proper choice of layers on either side of BTO, one may be able to achieve very good reversal of RSA to SA and vice versa by changing the angle of incidence. Moreover, when the thickness of the defect layer (BTO) becomes larger, the SA behaviour dominates and obscures RSA behaviour. The estimated nonlinear saturable absorption coefficient $\alpha(I)$ and effective two photon absorption coefficient $\beta(I)$ of 1-D asymmetric dielectric MC are shown in Table 6.2.

Angle	$\alpha(I)$ (cm/W)	$\beta(I)$ (cm/W)
20°	NA	1.52×10^{-4}
25°	NA	1.02×10^{-4}
30°	-1.85×10^{-4}	NA
35°	-3.02×10^{-4}	NA
Ref. layer $BaTiO_3$	-1.29×10^{-10}	NA

Table.6.2: *Estimates of nonlinear absorption coefficients: nonlinear saturable absorption coefficient α(I) and effective two photon absorption coefficient β(I).*

6.3.2 Photoluminescence

Figure 6.6(a) shows the linear absorption spectrum of BTO, the defect material used in the fabrication of the microcavity. The absorption peaks appear at 296 nm and 460 nm. The photoluminescence of the BTO of single layer and the same layer inside microcavity, at the excitation wave length 460 *nm* is shown in Figure 6.6(b). A strong enhancement in PL emission with a significant line narrowing of the spectrum is observed which may indicate the stimulated emission in the microcavity. The efficiency of the microcavity is determined by its Quality factor by calculating $\lambda/\Delta\lambda$, which is found to be 30. We interpret this as microcavity multiple reflections and the enhancement in the stimulated emission, which is obtained by sandwiching the material in between two Bragg mirrors. The angle tuned PL emission spectra of the microcavity, in the range of excitation angles 20° to 60°, with a step size 10° is given in Figure 6.6(c). There is considerable blue shift that is observed for higher angles of incidence. The PL emission occurs by several paths, involving numerous states within the forbidden band gap. PL is directly associated with the localized states existing inside of the band gap. The conduction band of $BaTiO_3$ is formed by Barium *s* and Titanium *s* and *d* states and the valence band is formed by Oxygen *2p* states. An electron transfer occurring between Barium and Titanium ions may introduce delocalized electronic levels in the forbidden gap. The presence of *s* and *p* states inside the band gap is attributed to the formation of clusters (TiO_2 or TiO_5) which decrease the band gap emission [13-15].

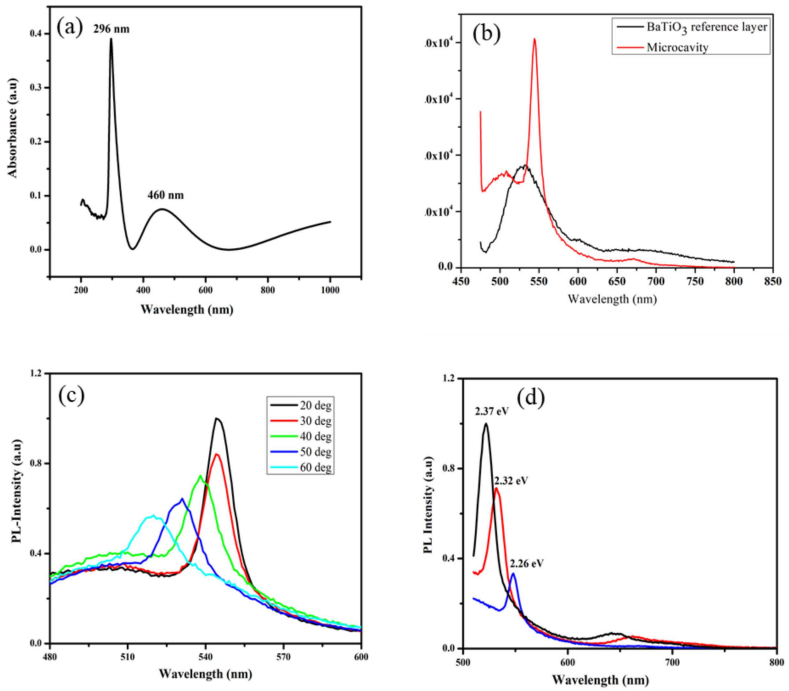

Figure.6.6*: (a) Absorption spectrum of the BTO reference layer (b) Photoluminescence spectra of single layer BTO and BTO in the 1-D asymmetric microcavity. (c) Angle dependent photoluminescence emission spectra of the microcavity. (d) Excitation energy dependent change in the photoluminescence emission spectrum.*

PL emission spectra is recorded at different excitation (pump) energies, namely, 3.09 eV (400 nm), 2.95 eV (420 nm) and 2.81 eV (440 nm). Figure 6.6(d) shows the excitation energy dependent change in the photoluminescence emission spectrum. The emission is recorded at 2.37 eV (522 nm), 2.32 eV (532 nm) and 2.26 eV (548 nm) respectively. An increase in the intensity of the photoluminescence emission and corresponding blue shift of the emission spectrum are observed with an increase in the excitation energy, as can be seen in Figure 6.6 (d).

6.4 Conclusions

1-D asymmetric photonic microcavity with $BaTiO_3$ (BTO) as defect layer sandwiched between asymmetric DBRs of SiO_2 and TiO_2 was fabricated using RF sputtering technique. The reflection spectrum shows cavity resonance at 532 nm at an angle of 30°. The spatial field intensity distribution with respect to angle and wavelength using transfer matrix simulation clearly shows large light-matter interaction and high density of electromagnetic modes at 30°. The open aperture Z-scan shows an enhancement in nonlinear absorption in the microcavity and a switching behaviour from RSA to SA for higher angles of incidence, for the same laser intensity of the beam. It is found that the SA behaviour dominates over RSA, for a higher thickness of BTO defect layer. Such high intensity laser induced optical nonlinearities can be further utilized for many nonlinear optical applications such as controlled nonlinear filters, holographic data usage etc. Further, the strong absorption and emission features of BTO can be tuned, utilizing the photonic cavity effects for both fundamental and advanced understanding. A large enhancement in photoluminescence is observed due to the stimulating action of the asymmetric microcavity and the corresponding Q-factor was found to be 30. It is observed that there is considerable blue shift of the emission spectrum with an increase in the pump excitation energy.

6.5 References

[1] C. M. Soukoulis, “Photonic crystals and light localization in the 21st century.”, Springer Science & Business Media 563 (2012).

[2] J. D. Joannopoulos, P. R. Villeneuve and S. Fan, “Photonic crystals.”, Solid State Commun. 102.2-3, pp165-173 (1997).

[3] H. Jiang, H. Chen, H. Li, Y. Zhang and S. Zhu, “Omnidirectional gap and defect mode of one-dimensional photonic crystals containing negative-index materials.”, Appl. Phys. Lett. 83, pp5386-5388 (2003).

[4] Y. Fink, J. N. Winn, S. Fan, C. Chen, J. Michel, J. D. Joannopoulos and E. L. Thomas, “A dielectric omnidirectional reflector.”, Science 282 (5394), pp1679-1682 (1998).

[5] W. H. Southwell, “Omnidirectional mirror design with quarter-wave dielectric stacks.”, Appl. Opt. 38 (25), pp5464-5467 (1999).

[6] E. Yablonovitch, “Inhibited spontaneous emission in solid-state physics and electronics.”, Phys. Rev. Lett. 58 (20), p2059 (1987).

[7] S. John, “Strong localization of photons in certain disordered dielectric superlattices.”, Phys. Rev. Lett. 58 (23), p2486 (1987).

[8] A. P. Vinogradov, A. V. Dorofeenko, S. G. Erokhin, M. Inoue, A. A. Lisyansky, A. M. Merzlikin and A. B. Granovsky, “Surface state peculiarities in one-dimensional photonic crystal interfaces.”, Phys. Rev. B 74 (4), p045128 (2006).

[9] L. Shiveshwari and P. Mahto, “Photonic band gap effect in one-dimensional plasma dielectric photonic crystals.”, Solid State Commun. 138(3), pp160-164 (2006).

[10] S. Guddala, V. K. Dwivedi, G. Vijaya Prakash and D. N. Rao, “Raman scattering enhancement in photon-plasmon resonance mediated metal-dielectric microcavity.”, J. Appl. Phys. 114, p224309 (2013).

[11] Q. Gong and X. Hu, “Photonic crystals: principles and applications.”, Pan Stanford, (2014).

[12] M. Sheik-Bahae, A. A. Said, T. H. Wei, D. J. Hagan and E. W. VanStryland, “Sensitive measurement of optical nonlinearities using a single beam.”, IEEE J. Quantum Electron. 26, pp760-769 (1990).

[13] N. K. Shihab, J. N. Acharyya, U. M. Rasi, R. B. Gangineni, G. Vijaya Prakash and D. N. Rao, “Cavity Enhancement in Nonlinear Absorption and Photoluminescence of $BaTiO_3$.”, Optik p163896 (2019).

[14] L. S. Cavalcante, M. F. C. Gurgel, A. Z. Simoes, E. Longo, J. A. Varela, M. R. Joya and P. S. Pizani, “Intense visible photoluminescence in Ba $(Zr_{0.25}Ti_{0.75})O_3$ thin films.”, Appl. Phys. Lett. 90, p011901 (2007).

[15] G. F. G. Freitas, R. S. Nasar, M. Cerqueira, D. M. A. Melo, E. Longo and J. A. Varela, “Luminescence in semi-crystalline zirconium titanate doped with lanthanum.”, Mater. Sci. Eng. A. 434, pp19-22 (2006)

Chapter 7

Conclusions and Future Perspectives

7.1 Conclusions

Photonic crystal microcavity with adjacent layers of SiO_2-TiO_2 and SiO_2-SnO_2 are fabricated using Sol-Gel and characterised their linear transmission through reflection spectrum and studied the morphology using FESEM. Role of number of layers and the refractive index contrast between the adjacent materials on the band gap in the reflection spectrum for both TM and TE polarization modes are studied. Interestingly, the FWHM of the stop band is shorter for TM mode, but the reflectivity is found to be higher compared to that of TE mode. However, consistent fabrication of the crystal was not achievable, due to unavoidable issues like cracking, which necessitated changing the fabrication method to RF magnetron sputtering.

A conventional photonic crystal microcavity (symmetric microcavity) with Bragg mirrors (alternate layers of SiO_2 and TiO_2) of quarter wave optical thickness and the defect (a layer of $BaTiO_3$) with half wave optical thickness is fabricated by the RF sputtering with a Q-factor of 48. The reflection spectrum of the sample reveals a cavity resonance at 532 nm in a 205 nm broad photonic band gap at an incident angle 32°. The wavelength and the incident angle dependent spatial field intensity distribution is numerically simulated using transfer matrix technique. Such study clearly shows the large light-matter interaction and high density of electromagnetic modes at 32°, thus substantiating the experimental findings. The nonlinear absorption of the cavity is studied using Z-scan technique, and it is observed to show saturable absorption at every incident angle. The enhancement of nonlinear absorption in the microcavity is expressed in terms of enhancement factor G, which is found to be nearly 16, calculated by means of spatial distribution of optical field. The large enhancement is attributed as being due to the strong confinement of the optical field. The photoluminescence spectrum of the reference layer and 1DPhC were also studied and compared to understand the role of defect layer in its optical properties.

The crucial role of the thickness of defect layer, i.e. the microcavity, for a given wavelength is explored by fabricating two identical microcavities with different thicknesses of the defect layer. The first microcavity is chosen to be a conventional photonic microcavity with a defect layer thickness of $\lambda/2$, and the second one is an unconventional photonic microcavity with an arbitrary thickness, in this case $2\lambda/3$, with the same Bragg mirrors. The enhancement in the nonlinear absorption coefficient of both cavities are measured using open aperture Z- scan technique with a nanosecond (ns) laser and results are compared. It is found that, with an increase in the thickness of the defect layer, there is a switching from reverse saturable absorption (RSA) to saturable absorption (SA), in response to the angle tuning of the sample. The spatial field distribution along the depth of the microcavities, using transfer matrix simulation validated our experimental results.

Next, we fabricated an asymmetric photonic microcavity in which both the Bragg mirror of SiO_2 and TiO_2 and the defect of $BaTiO_3$ (BTO) layers are not as per the Bragg's condition. The reflection spectrum shows a cavity resonance at 532 nm at an angle of 30° and at this particular angle the spatial field intensity using transfer matrix simulation clearly shows enhanced light-matter interaction and high density of electromagnetic modes. The open aperture Z-scan shows an enhancement in nonlinear absorption in the microcavity and a switching behaviour from reverse saturable absorption to saturable absorption, for higher angle of incidence, for the same intensity of the laser beam. It is seen that the SA behaviour dominates over RSA for the higher thickness of BTO defect layer. A large enhancement in photoluminescence is observed, due to the lasing action of the asymmetric microcavity and the corresponding Q-factor was found to be 30. It is observed that there is considerable blue shift of the emission spectrum with the increase of excitation pump energies.

7.2 Future Scope

As a next step, it is planned to demonstrate slow light in a photonic crystal using Michelson Interferometer technique, as this phenomenon has wide applications in microlasers, optical

storage, optical microamplifiers etc. It will also throw more insight into the changes in the light matter interaction within the defect layer.

Co-sputtering of defect layer BTO with metals like copper, silver in photonic crystal microcavity is another technique that helps to understand the photon-plasmon interactions. In such systems, plasmons interacting with photon at optical frequencies produces another quasiparticle, the plasmon polariton. The resultant absorption and emission peaks can be used in molecular sensors. Moreover, plasmons are known to play an efficient role in information transfer on computer chips, as plasmons can support higher frequencies. Such plasmonic enhancement may result in plasmon based electronic devices. Large variety of incorporation of materials as defect is possible in the case of Sol-Gel method, once we succeed in quality fabrication of a microcavity using the Sol-Gel method.

List of Publications

[1] N. K. Shihab, J. N. Acharyya, U. M. Rasi, R. B. Gangineni, P. A. Lakshmi, G. V. Prakash and D. N. Rao, "Nonlinear optical absorption switching behaviour of $BaTiO_3$ in asymmetric microcavity", Opt. Mater. 101, p109777 (2020).

[2] N. K. Shihab, J. N. Acharyya, U. M. Rasi, R. B. Gangineni, G. V. Prakash and D. N. Rao, "Cavity enhancement in nonlinear absorption and photoluminescence of $BaTiO_3$.", Optik, p163896 (2019).

[3] U. M. Rasi, N. K. Shihab, S. Angappane, R. B. Gangineni, "Coexistence of ferromagnetic and spin glass-like magnetic order in $Bi_{10}Co_{16}O_{38}$–$Bi_{25}FeO_{40}$ powder composite.", Ceram. Int. 45(12), pp15171-15177 (2019).

[4] J. George, M. George, J. Alex, D. Sajan, N. K. Shihab, G. Vinitha and R. Chitra, "Growth of Morpholin-4-ium hydrogen tartrate single crystal for optical limiting application.", Opt Laser Technol. 119, p105647 (2019).

[5] L. M. Clavian, P. R. Kumar, K. A. Kumar, D. N. Rao, N. K. Shihab and S. Ganesh, "Enhanhanced third order optical nonlinearity in ultrathin amorphous film of tetraphenyl-porphyrin in picosecond regime.", Opt. Laser Technol. 119, pp105642 (2019).

[6] M. V. Rao, V. R. K. Kumar, N. K. Shihab and D. N. Rao, "Third order nonlinear and optical limiting properties of alkaline bismuth borate glasses.", Opt Laser Technol. 107, pp110-115 (2018).

[7] M. V. Rao, V. R. K. Kumar, N. K. Shihab and D. N. Rao, "Z-scan studies of Barium Bismuth Borate glasses.", Opt. Mater. 84, pp178-183 (2018).

Conference Proceedings

[1] N. K. Shihab, U. P. Mohammed Rasi, R. B. Gangineni and D. Narayana Rao, *"*Cavity enhancement in Photoluminescence of $BaTiO_3$in 1-D Dielectric microcavity.", DAE-BRNS NLS proceedings 2016. (Dec 20-23 , KIIT University, Bhubaneswar, Odisha).

[2] N K Shihab and D Narayana Rao, “Sol-Gel processed one dimensional photonic system.”, Student conference on Optics and Photonics (SCOP) 2016. (Sep 2-3, Physical Research Laboratory, Ahmedabad).

[3] N. K. Shihab, U. P. Mohammed Rasi, R. B. Gangineni and D. Narayana Rao, “1-D Photonic Crystal: A comparison of Sol-Gel and RF Sputtering fabrications.”, (Sep 21-23,2017 Photonic crystal symposium, IIT Kanpur).

[4] L. M. Clavian, P. C. Rajesh Kumar, K. V. Anil Kumar, D. Narayana Rao, N. K. Shihab, and G. Sanjeev, “Third order optical nonlinearity in TPP incorporated PMMA composite thin film.”, AIP Conference Proceedings 2115, p030287 (2019).

[5] P. C. Rajesh Kumar, L. M. Clavian, K. V. Anil Kumar, D. Narayana Rao, N. K. Shihab, and G. Sanjeev, “Intensity dependent third order optical nonlinearity of zinc-tetraphenyl porphyrin ultrathin film in nano-second regime.”, AIP Conference Proceedings 2115, p030329 (2019).

Workshops and Symposia

[1] DST-SERC School on ‘Nonlinear optics and Materials’, Department of Science and Technology, New Delhi (3-21 February 2014, SSN College of Engineering, Chennai).

[2] Short course on ‘Photonic materials, Characterization and techniques’ conducted by Indian Laser Association (1-2 December 2014, SV University, Tirupati).

[3] N. K. Shihab, U. P. Mohammed Rasi, R. B. Gangineni and D. Narayana Rao, “1-D Photonic Crystal: A comparison of Sol-Gel and RF Sputtering fabrications.”, (Sep 21-23,2017 Photonic crystal symposium, IIT Kanpur).

Nonlinear Optical Properties of BaTiO3 in Symmetric and Asymmetric Microcavities

by Shihab N.k

Nonlinear Optical Properties of BaTiO3 in Symmetric and Asymmetric Microcavities

ORIGINALITY REPORT

33%	4%	32%	10%
SIMILARITY INDEX	INTERNET SOURCES	PUBLICATIONS	STUDENT PAPERS

PRIMARY SOURCES

1	N.K. Shihab, Jitendra Nath Acharyya, U.P. Mohammed Rasi, R.B. Gangineni, G. Vijaya Prakash, D. Narayana Rao. "Cavity enhancement in nonlinear absorption and photoluminescence of BaTiO3", Optik, 2019 Publication	14%
2	N.K. Shihab, Jitendra Nath Acharyya, U.P. Mohammed Rasi, R.B. Gangineni, P. Anantha Lakshmi, G. Vijaya Prakash, D. Narayana Rao. "Nonlinear optical absorption switching behavior of BaTiO3 in asymmetric microcavity", Optical Materials, 2020 Publication	13%
3	Submitted to University of Hyderabad, Hyderabad Student Paper	1%
4	B. Nithyaja, H. Misha, P. Radhakrishnan, V. P. N. Nampoori. "Effect of deoxyribonucleic acid on nonlinear optical properties of Rhodamine 6G-polyvinyl alcohol solution", Journal of Applied	<1%

Out of 33% of similarity index, approximately 27% is from student's own publications (Ref. 1, 2). We also found that the software, which used to check the similarity index, is including the generic terms which are repeatedly used in this thesis and also counted multiple times at the time of calculation of similarity index. Some of them are photonic crystal, refractive index, SiO_2, TiO_2, $BaTiO_3$ and so on, which are quite in the research domain.

Prof. D. Narayana Rao

Prof. P. Anantha Lakshmi